A STUDY OF THERMAL NOISE

by

JOSEPH MICHAEL KOVALIK

B. S. California Institute of Technology
(1986)

SUBMITTED IN PARTIAL FULFILLMENT
OF THE REQUIREMENTS FOR THE
DEGREE OF

DOCTOR OF PHILOSOPHY

at the

MASSACHUSETTS INSTITUTE OF TECHNOLOGY

September, 1994

Signature of Author______________________________
Department of Physics
August, 1994

Certified by______________________________
Rainer Weiss
Thesis Supervisor

Accepted by______________________________
George Koster
Chairman, Department Committee

A STUDY OF THERMAL NOISE

by

JOSEPH MICHAEL KOVALIK

Submitted to the Department of Physics in August, 1994
in partial fulfillment of the requirements for
the degree of Doctor of Philosophy in Physics

Abstract

Thermal noise will be a fundamental limit to the sensitivity of the Laser Interferometer Gravitational Wave Observatory (LIGO) in the frequency band where astrophysical sources should be detected. A study of thermal noise in mechanical systems helps to predict the noise floor of high sensitivity experiments such as LIGO and also gives insight to the loss mechanisms in macroscopic systems. This thesis investigates the thermal noise in wires that support the test masses of a gravity wave detector and in the internal normal modes of the test masses themselves.

The thermal noise of a pendulum is calculated by considering the losses in the flexure of the thin fibres that support the pendulum mass. An experimental investigation of thermoelastic damping was done by measuring the Q's of thin fibres made of tungsten, sapphire, silicon and fused quartz. Tungsten had the highest losses with Q's on the order of 10^3. Fused quartz had the lowest losses with Q's between $10^5 - 10^6$. The results indicate that thermoelastic damping is at best only an upper limit for the Q of a wire.

The internal thermal noise of the gravity wave detector test masses depends upon the frequency dependence of the loss mechanism in the test mass material (in this case, fused quartz-SiO_2). The design and noise sources of a high sensitivity special purpose interferometer to measure the thermally excited motions in a thin disk of fused quartz are presented. The RMS thermally driven motion of the mechanical resonances from normal modes between 8 kHz and 20 kHz was $4 \times 10^{-13} cm$ and the typical Q between 5×10^3 and 10^5. The measured mechanical noise of the system was $2 \times 10^{-15} cm/\sqrt{Hz}$ between 1 kHz and 20 kHz which was too large to be attributed to the off-resonance thermal noise from one of the measured mechanical modes of the plate. Various candidates for this noise are presented. Future experiments that would lead to a better understanding of the measured noise are discussed.

A possible microscopic model for the loss mechanisms in fused quartz is presented.

Finally, a method to monitor the internal thermal noise directly in future advanced gravity wave detectors is discussed. The optical experiment performed in this thesis is a prototype for such a technique.

Thesis Supervisor: Dr. Rainer Weiss

Title: Professor of Physics

Acknowledgments

I have been a graduate student for eight years now and will end this stage of my education with the submission of this thesis. I have by no means ended my career as a student. There is far too much to learn for anyone to believe that their studies can be completed by the award of a degree.

I would like to thank my supervisor Rai Weiss whose relentless pursuit of scientific excellence has allowed me to investigate many different aspects of experimental physics. I would like to thank Marcus Bennet who generously donated his time to perform some of the tasks that led to the experiments performed in this thesis. I would like to thank Joe Giaime for trading lists of the outrages perpetrated against people with the status of graduate student. I would like to thank everyone in the lab past and present for their camaraderie especially AJ, Brian, Dick, David, Nelson, Dick, Nergis, Susan, Tom, Viktor and Yaron. I would like to thank Peter Saulson for introducing me to research in thermal noise.

Over the course of my time at MIT, I have made many friends outside of the lab. I particularly thank Mike, Tom and Baraga for their friendship. I would like to thank Marshall Hughes for introducing me to the Sharing a New Song chorus and the world of Russian music and travel.

My parents have been an uninterrupted source of support for me in every way. I do not think that I could have finished this degree without their backing and that of my brothers and sisters.

Finally, I would like to thank my fiancee Carol McComas. She met me at the point of my graduate school career when the light at the end of the tunnel seemed impossibly far away and managed to make it bearable. With the completion of this thesis, I look forward to embarking on the rest of my life with her.

Contents

Chapter 1 Introduction

1.1 Gravitational Wave Detection

The research described in this thesis was undertaken as part of the Laser Interferometer Gravitational Wave Observatory (LIGO) project. The fundamental goal of the LIGO project is to detect gravitational radiation from astrophysical sources. Since a great deal has already been written about this subject (see for example [1]), a brief description of the expected magnitude of a gravity wave signal and of the typical detector noise gives an adequate impetus for the study of thermal noise that was undertaken in this thesis.

Einstein's Theory of General Relativity is a very successful theory of classical gravitation that has been verified experimentally in many ways. One of the most interesting physical phenomena that it predicts is the existence of space-time disturbances that travel as plane waves at the speed of light. The metric is

$$g_{\mu\nu} \approx \eta_{\mu\nu} + h_{\mu\nu} \tag{1.1.1}$$

where $\eta_{\mu\nu}$ is the Minkowski metric and $h_{\mu\nu}$ is the gravity wave disturbance that satisfies the wave equation

$$\left(\nabla^2 - \frac{1}{c^2}\frac{\partial^2}{\partial t^2}\right)h_{\mu\nu} = 0 \tag{1.1.2}$$

The gravity wave has two polarizations that produce tidal disturbances in the space-time metric.

While there are some similarities between classical electromagnetic wave theory and that of gravity, the most important difference between the two theories to be considered in this thesis is the inherent weakness of gravity with respect to electromagnetism. Because linear momentum and angular momentum must be conserved, both the electric dipole and magnetic dipole radiation of electromagnetic theory cannot occur in gravity theory. Instead, the lowest order term is a quadrupole. The common way to describe the strength of a gravitational wave is in terms of the strain $h = \Delta l/l$. The amount of power in gravity waves emitted by a time varying quadrupole is:

$$P \approx \frac{G}{45c^5}\left(\frac{d^3Q^{kl}}{dt^3}\right)\left(\frac{d^3Q^{kl}}{dt^3}\right) \tag{1.1.3}$$

where Q^{kl} is the mass quadrupole moment

$$Q^{kl} = \int \left(3x^k x^l - r^2\delta_k^l\right)\rho(\overline{x})d^3x \tag{1.1.4}$$

The strain is

$$h \approx \frac{2G}{3Rc^4}\left(\frac{d^2Q^{kl}}{dt^2}\right) \tag{1.1.5}$$

where G is the gravitational constant and R is the distance to the source. This is enough information to obtain an order of magnitude estimate of the gravity wave amplitude. (For a more complete discussion of gravitational wave sources see for example Smarr [2]).

The gravity wave amplitude will be on the order

$$h \sim \frac{G(kinetic\ energy)}{c^4 R} \tag{1.1.6}$$

The kinetic energy in this case is the non-spherical component of the kinetic energy in the source. In order to make a rough estimate, the kinetic energy will be explicitly defined as Mv^2 where M is the mass of the source. This gives a simpler expression for the gravity wave amplitude

$$\begin{aligned} h \sim \frac{GM\left(\frac{v}{c}\right)^2}{c^2 R} &\sim 10^{-18}\left(\frac{M}{M_\odot}\right)\left(\frac{10kpc}{R}\right)\left(\frac{v}{c}\right)^2 \\ &\sim 10^{-21}\left(\frac{M}{M_\odot}\right)\left(\frac{10Mpc}{R}\right)\left(\frac{v}{c}\right)^2 \end{aligned} \tag{1.1.7}$$

where $M_\odot$ is the solar mass. The first result shows the scale of h for an event at the centre of our own galaxy. The probability of astrophysical events such as supernovae occurring, however, is much greater if one goes to distances where there are rich clusters of galaxies such as the Virgo cluster. It is clear that a gravitational wave detector must be able to achieve a sensitivity of $h \sim 10^{-21}$ if it is to find something.

There are at least two detection schemes to study gravity waves. The earlier technique involves looking for the excitation of the fundamental mode of a cylindrical bar of aluminum by a gravity wave. The typical resonant frequency of the bar is about 1 kHz with a bandwidth of order 10 Hz. One significant improvement in these detectors is the reduction of thermal noise by cooling them to milliKelvin temperatures. Other improvements in seismic isolation and transducer sensitivity have also enhanced the performance of these detectors [3]. A drawback is that the sensitivity is limited to a narrow band around the resonant frequency.

The other approach to the detection of gravity waves is to use a sensitive interferometer [4] to measure the distortion of space-time due to the passage of a gravity wave. The gravity wave effect on the detector can be described as a tidal force that moves test masses which are the end mirrors of the interferometer. Alternatively, in the rest frame of the test masses, the gravity wave distorts the space-time in the interferometer arms and thus produces an effective phase change in the light. The length of each interferometer arm in LIGO will be 4 km. This sets the length change that must be measured as $4 \times 10^{-16} cm$ for a gravity wave signal with a strain of 10^{-21}.

Figure 1.1.1 shows a schematic diagram of an interferometric gravity wave detector. The test masses are mirrors that are suspended as pendula. This allows the masses to be free falling in the direction of the optic axis. A gravity wave acts to change the effective length of the interferometer arms as shown. For half of the gravity wave period, one arm of the interferometer lengthens while the other contracts. For the other half of the gravity wave period, this is reversed.

Figure 1.1.1 Schematic of an interferometric gravity wave detector with Fabry-Perot cavity arms.

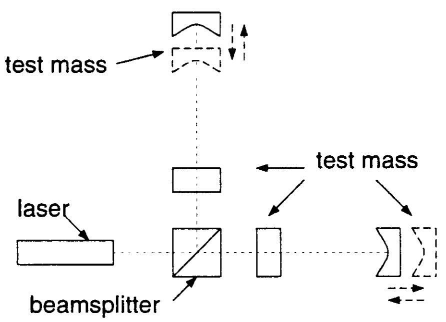

1.2 Noise Sources in Interferometric Gravitational Wave Detectors

There are many different noise sources besides thermal noise that must be considered to determine the sensitivity of interferometric gravitational wave detectors. These include the seismic noise of the gravity wave site, the photon shot noise, residual gas fluctuations, scattered light, laser frequency noise and many others (see [5]). The seismic noise is filtered by vibration isolation and the test mass suspension. The photon shot noise can be improved by increasing the power of the laser until the radiation pressure and its fluctuations become important. The other noise sources can be reduced by improvements in technology.

In the case of LIGO, the sensitivity of the detector is so high that thermal noise is a significant noise source. The interferometer is designed so that the mechanical resonant frequencies of the system are outside the gravitational wave detection band. In this way, only the off-resonance thermal noise must be considered (see section 1.4). The magnitude and shape of the off-resonance spectrum depends on the loss mechanisms of the mechanical system. There are two sets of thermal noise sources and frequency regimes that must be considered.

The suspension of the test masses is a pendulum with a resonant frequency on the order of 1 Hz. Since the best sensitivity of LIGO will be at 100 Hz where the photon shot noise and the radiation pressure noise are approximately equal, the regime of $\omega >> \omega_0$ is important. In this case, one would want the loss mechanism to have a structure damping rather than viscous damping frequency dependence (see the section 1.4 for an explanation of these terms) since it has a steeper slope and will have lower thermal noise above the resonant frequency.

The other major thermal noise source comes from the internal modes of the test masses that have resonant frequencies larger than 10 kHz. The frequency regime of interest here is for $\omega << \omega_0$. A loss mechanism with a structure damping frequency dependence would not be desirable in this case since the noise increases at low frequencies. For example, if the resonant frequency of an internal mode is 10 kHz, the thermal noise will be a factor of 10 worse at 100 Hz if the loss mechanism has a structure damping rather than a viscous damping frequency dependence.

The initial parameters for LIGO used a viscous damping model for the loss mechanism in both the suspensions and the test mass substrate. Figures 1.2.1 and 1.2.2 show the spectra of noise sources for both an early LIGO detector and an advanced one. Assuming a viscous damping mechanism, the early LIGO detector is limited by the capabilities of existing technology. The detector noise is dominated by seismic noise below 100 Hz, by suspension thermal noise in the frequency range of a few 100 Hz and by photon shot noise above a few 100 Hz. By improving the seismic isolation and the suspension design and by increasing the laser power, their contribution to the noise decreases and thermal noise from internal modes of the test masses becomes a significant noise source for an advanced detector.

Figure 1.2.1 Noise sources for an early LIGO detector [5]. The parameters used to make these predictions are: Laser Power=5 Watts, mirror losses=50 ppm, recycling factor=30, test masses=10kg, suspension Q=10^7, internal mirror Q=10^4, vacuum H_2=10^{-6} torr, H_2O=10^{-7} torr. The stippled area shows the range where the thermal noise may appear depending on the loss mechanisms in both the suspension and the test mass substrate.

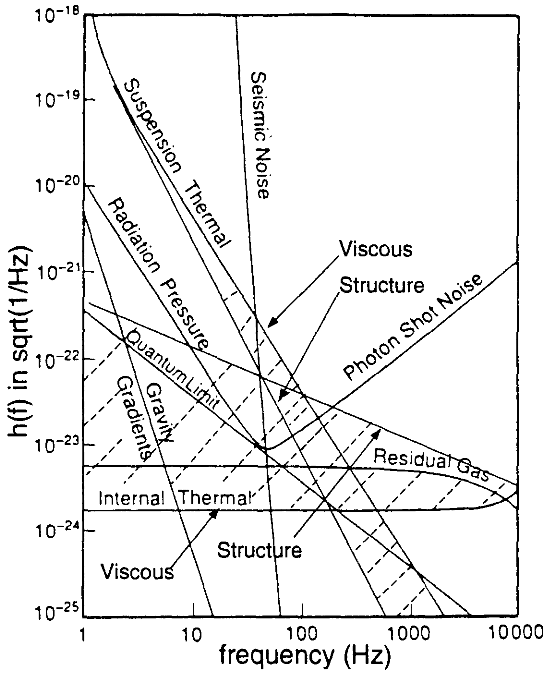

Figure 1.2.2 Noise sources for an advanced LIGO detector [5]. The parameters used to make these predictions are: Laser Power=60 Watts, mirror losses=20 ppm, recycling factor=100, test masses=1 ton, suspension Q=10^9, internal mirror Q=10^4, vacuum $H_2=10^{-9}$ torr, $H_2O=10^{-10}$ torr. The stippled area shows the range where the thermal noise may appear depending on the loss mechanisms in both the suspension and the test mass substrate

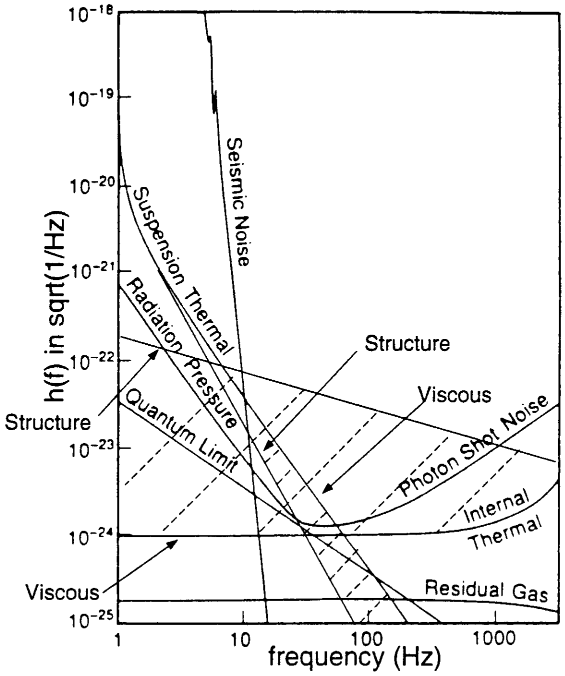

The noise plots in figures 1.2.1 and 1.2.2 show the difference in the off-resonance thermal noise spectrum between the two loss mechanisms. If the dominant loss mechanism in the test mass substrate has a structure damping frequency dependence, the thermal noise becomes a very significant problem. It is now clear that a better understanding of the loss mechanism frequency dependence is needed. This thesis will attempt to measure the off resonance noise spectrum of fused quartz and hence, determine the frequency dependence of the loss mechanisms.

1.3 Brownian Motion and the Fluctuation-Dissipation Theorem

The important physical concept in thermal noise is the relation between the frictional force that dissipates energy in a system and the fluctuating forces that excite the same system about equilibrium. A useful model for this phenomenon is the Brownian motion of a particle in one dimension. (For some useful discussions, see the papers collected in [6]. The approach here follows that of Reif [7]). It is interesting to note that once again this is a problem that was studied by Einstein.

Since it is difficult to describe the interaction of a particle with all of the degrees of freedom for every other particle in the system, they will be regarded as a heat reservoir with a temperature T and an interaction that can be lumped into some net force $F(t)$. This force varies with a rate that is characterized by a correlation time τ^* that measures the relaxation time for the system to return to equilibrium after a sudden disturbance away from equilibrium. The response of a free particle to such an interaction would have a characteristic time on the order of the mean intermolecular separation divided by the mean molecular velocity. For a particle bound with a linear restoring force such as a harmonic oscillator, the characteristic time is on the order of the period of the oscillator multiplied by its Q. If there is another external force $\widetilde{F}(t)$, the particle's motion can be written as

$$m\frac{dv}{dt} = \widetilde{F}(t) + F(t) \tag{1.3.1}$$

where m is the mass of the particle.

By integrating this equation of motion over a time interval $\tau >> \tau^*$ that is still small on a macroscopic time scale, one receives

$$m[v(t+\tau) - v(t)] = \widetilde{F}(t)\tau + \int_t^{t+\tau} F(t')dt' \tag{1.3.2}$$

By expanding the fluctuating force into its slowly varying part $\overline{F}(t)$ and rapidly fluctuating part $F'(t)$ and doing the same to the velocity, one can expand the force in a linear fashion as

$$\overline{F}(t) = -\alpha\overline{v} \tag{1.3.3}$$

where α is a friction constant. This leads to the Langevin equation

$$m\frac{dv}{dt} = \widetilde{F}(t) - \alpha v + F'(t) \tag{1.3.4}$$

In the absence of an external force, a particle will follow the equation of motion

$$\begin{gathered} m\frac{dv}{dt} = -\alpha v + F'(t) \\ mx\frac{d\dot{x}}{dt} = m\left[\frac{d}{dt}(x\dot{x}) - \dot{x}^2\right] = -\alpha x\dot{x} + xF'(t) \end{gathered} \tag{1.3.5}$$

By taking ensemble averages and noting that $\langle xF'(t)\rangle = \langle x\rangle\langle F'(t)\rangle = 0$ and $\frac{1}{2}m\langle\dot{x}^2\rangle = \frac{1}{2}k_BT$ where k_B is Boltzmann's constant gives

$$m\frac{d}{dt}\langle x\dot{x}\rangle = k_BT - \alpha\langle x\dot{x}\rangle \tag{1.3.6}$$

Solving this equation with initial conditions $x(0) = 0$ gives

$$\langle x^2\rangle = \frac{2k_BT}{m\gamma}\left[t - \frac{1}{\gamma}(1 - e^{-\gamma t})\right] \tag{1.3.7}$$

where $\gamma = \frac{\alpha}{m}$ and γ^{-1} denotes the characteristic time of the system.

For a time interval $t << \gamma^{-1}$,

$$\langle x^2\rangle = \frac{k_BT}{m}t^2 \tag{1.3.8}$$

and the particle behaves as if it were moving with a constant thermal velocity $v = \sqrt{\frac{k_B T}{m}}$. For a time interval $t >> \gamma^{-1}$,

$$\langle x^2 \rangle = \frac{2k_B T}{m\gamma} t \tag{1.3.9}$$

and the particle behaves as if it were executing a random walk.

For a harmonically bound particle, the equation of motion is

$$m\frac{dv}{dt} = -\alpha v + F'(t) - m\omega_0^2 \tag{1.3.10}$$

where $\omega_0 = \sqrt{k/m}$ is the resonant frequency of the oscillator. The solution to this equation is a more complicated problem than that of the free particle (see for example Uhlenbeck in [6]). The important result is that with initial conditions $x(0) = 0$ and $v(0) = 0$

$$\langle x^2 \rangle = \frac{kT}{m\omega_0^2}\left(1 - e^{-(2m\omega_0^2/\alpha)t}\right) \tag{1.3.11}$$

In this case, the characteristic time constant of the system is $m\omega_0^2/\alpha$ or Q/ω_0 where $Q = m\omega_0/\alpha$.

A more general approach to this problem takes into account the thermodynamic properties of the heat reservoir and how the equilibrium is disturbed and reestablished. Assume there is a small subsystem A described by x and the other degrees of freedom with which this coordinate interacts through the force F. All the other degrees of freedom are described by a large heat bath B. The ensemble average of equation 1.3.2 is

$$m\langle[v(t+\tau) - v(t)]\rangle = \widetilde{F}(t)\tau + \int_t^{t+\tau} \langle F(t')\rangle dt' \tag{1.3.12}$$

If at some time t the particle has a velocity $v(t)$, then the system A is at equilibrium to first degree with $\langle F \rangle = 0$ and the probability of A being in state r as $W_r^{(0)}$. In the next approximation, at time $t' = t + \tau'$, the particle has velocity $v(t + \tau')$. If τ' is sufficiently small, the particle's velocity changes and the internal equilibrium is disturbed. After a time of order τ^*, the equilibrium is reestablished and is consistent with $v(t + \tau')$. The heat bath B will be found with equal likelihood in any one of its Ω accessible states. If the change in velocity is $\Delta v(\tau')$, then the energy of B changes by $\Delta E'(\tau')$. This energy change must equal the work done by the force on the particle

$$\Delta E' = \int_t^{t'} v(t'')F(t'')dt'' \approx -v(t)\int_t^{t'} F(t'')dt'' \tag{1.3.13}$$

In equilibrium, the probability of the occurrence of a state r of A is proportional to the corresponding number of states accessible to the heat bath B. Comparing the probability of the occurrence of the same configuration r at times t and $t + \tau'$ gives

$$\frac{W_r(t+\tau')}{W_r^{(0)}} = \frac{\Omega(E' + \Delta E')}{\Omega(E')} = e^{\beta \Delta E'} \tag{1.3.14}$$

where $\beta = \frac{\partial \ln \Omega}{\partial E'}$. The mean value of F at a later time $t' = t + \tau'$ is

$$\begin{aligned}\langle F\rangle &= \sum_r W_r(t+\tau')F_r = \sum_r W_r^{(0)} e^{\beta \Delta E'}(t+\tau')F_r \\ &\approx \big\langle (1+\beta\Delta E')F\big\rangle_0\end{aligned} \tag{1.3.15}$$

Since $\langle F\rangle_0 = 0$,

$$\begin{aligned}\big\langle F(t')\big\rangle &= -\beta\left\langle F(t')v(t)\int_t^{t'} F(t'')dt''\right\rangle_0 \\ &= -\beta\bar{v}(t)\int_t^{t'} dt''\big\langle F(t')F(t'')\big\rangle_0\end{aligned} \tag{1.3.16}$$

and the equation of motion becomes for $s = t'' - t'$

$$m\langle[v(t+\tau)-v(t)]\rangle = \widetilde{F}(t)\tau - \beta\bar{v}(t)\int_t^{t+\tau} dt' \int_{t-t'}^{0} ds\big\langle F(t')F(t'+s)\big\rangle_0 \tag{1.3.17}$$

The ensemble average in equation 1.3.17 is the correlation function of $F(t)$ defined as

$$\begin{aligned}K(s) &= \big\langle F(t')F(t'+s)\big\rangle_0 \\ &= \langle F(t)F(t+s)\rangle\end{aligned} \tag{1.3.18}$$

If s becomes sufficiently large, then $F(t)$ and $F(t+s)$ become uncorrelated and one has a general form for $K(s)$ (see figure 1.3.1)

$$\begin{aligned}K(0) &= \big\langle F^2(t)\big\rangle > 0 \\ K(s) &\to \langle F(t)\rangle\langle F(t+s)\rangle,\ s\to\infty \\ K(s) &\to 0,\ if\ \langle F\rangle = 0,\ s\to\infty\end{aligned} \tag{1.3.19}$$

The characteristic time τ^* is the interaction time of the force and is very small on a macroscopic time scale.

Figure 1.3.1 Plot of the correlation function $K(s)$ for a random force $F(t)$

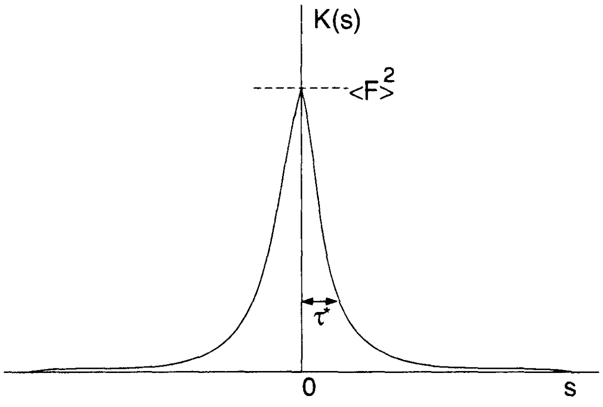

From the properties of this correlation function one can obtain a new form of equation 1.3.17

$$m\langle[v(t+\tau)-v(t)]\rangle = \widetilde{F}(t)\tau - \alpha\overline{v}(t)\tau \tag{1.3.20}$$

where

$$\alpha = \frac{1}{2k_BT}\int_{-\infty}^{\infty}\langle F(0)F(s)\rangle_0 ds \tag{1.3.21}$$

This is a form of the fluctuation dissipation theorem that has an explicit term for the friction force α in terms of the correlation function of the fluctuating force $F(t)$. It shows that the same forces that cause the system to fluctuate are those that cause it to dissipate energy.

The Brownian motion of a particle in the absence of external forces can be characterized as a Markoff process so that the probability $P(v,t)dv$ that the velocity of the particle is between v and $v+dv$ is not determined by its entire past history, but only from its velocity at a specific time. The probability can be written as conditional probability which depends on the values v_0, t_0

$$Pdv = P(v,t \mid v_o, t_0)dv \tag{1.3.22}$$

Since the actual time origin is not important, the probability can be written in term of the time difference $s = t - t_0$

$$P(v,t \mid v_o, t_0)dv = P(v,s \mid v_o)dv \tag{1.3.23}$$

For very short times, the probability that the velocity is known becomes a delta function

$$P(v,t \mid v_o, t_0) \rightarrow \delta(v-v_0),\ s \rightarrow 0 \tag{1.3.24}$$

For very long periods of time, the particle must come to equilibrium with the surrounding medium at temperature T and the probability reduces to the canonical distribution

$$P(v,t \mid v_o, t_0) \rightarrow \sqrt{\frac{m\beta}{2\pi}}e^{-\frac{1}{2}\beta m v^2},\ s \rightarrow \infty \tag{1.3.25}$$

The general condition that the probability must satisfy is that in any small time interval τ the [increase in probability that the particle has a velocity between v and $v+dv$] must be equal to the [decrease in this probability given that the particle has a probability $P(v_1,\tau \mid v)dv_1$ of changing its velocity to any other value between v_1 and v_1+dv_1] plus the [increase in this probability given that the particle, now with velocity between v_1 and v_1+dv_1 has a probability $P(v,\tau_1 \mid v_1)dv_1$ of changing its velocity back to between v and $v+dv$] or

$$\begin{aligned}\frac{\partial P}{\partial s}dv\tau = &-\int_{v_1} P(v,s \mid v_0)dvP(v_1,\tau \mid v)dv_1\\ &+\int_{v_1} P(v_1,s \mid v_0)dv_1P(v,\tau \mid v_1)dv\end{aligned} \tag{1.3.26}$$

Since $P(vs \mid v_0)$ does depend upon v_1 and $P(v\tau_1 \mid v)$ is properly normalized, the above equation becomes

$$\frac{\partial P}{\partial s}\tau = -P(v,s \mid v_0) + \int\limits_{-\infty}^{+\infty} P(v-\xi, s \mid v_0) P(v,\tau \mid v-\xi) d\xi \tag{1.3.27}$$

where $\xi = v - v_1$

This can be expanded in terms of a Taylor series about ξ such that

$$\begin{aligned} \frac{\partial P(v,s \mid v_0)}{\partial s} &= \sum_{n=1}^{\infty} \frac{(-1)^n}{n!} \frac{\partial^n}{\partial v^n} [M_n P(v,s \mid v_0)] \\ M_n &= \frac{1}{\tau} \int\limits_{-\infty}^{+\infty} d\xi \xi^n P(v+\xi, \tau \mid v) = \frac{\langle [\Delta v(\tau)]^n \rangle}{\tau} \end{aligned} \tag{1.3.28}$$

If τ is small, this reduces to the Fokker-Planck equation

$$\begin{aligned} \frac{\partial P}{\partial s} &= -\frac{\partial}{\partial v}(M_1 P) + \frac{1}{2}\frac{\partial^2}{\partial v^2}(M_2 P) \\ &= \gamma P + \gamma v \frac{\partial P}{\partial v} + \gamma \frac{kT}{m}\frac{\partial^2 P}{\partial v^2} \end{aligned} \tag{1.3.29}$$

The solution of this equation is

$$P(v,s \mid v_0) = \left[\frac{m}{2\pi kT(1-e^{-2\gamma s})}\right]^{\frac{1}{2}} \exp\left[-\frac{m\left(v - v_0 e^{-\gamma s}\right)^2}{2kT(1-e^{-2\gamma s})}\right] \tag{1.3.30}$$

and it approaches the limits of equations 1.3.24 and 1.3.25.

In experimental physics, it is often more useful to consider the frequency components of the noise sources using Fourier analysis. The correlation function can be expressed as a Fourier integral

$$\begin{aligned} K(s) &= \int\limits_{-\infty}^{+\infty} J(\omega) e^{i\omega s} d\omega \\ J(\omega) &= \int\limits_{-\infty}^{+\infty} K(s) e^{-i\omega s} ds \end{aligned} \tag{1.3.31}$$

where $J(\omega)$ is defined as the spectral density of $F(t)$. Since the $K(s)$ is real and symmetric, then $J(\omega)$ is also real and symmetric so that both functions satisfy

$$\begin{aligned} K^*(s) = K(s) \quad K(s) = K(-s) \\ J^*(\omega) = J(\omega) \quad J(\omega) = J(-\omega) \end{aligned} \tag{1.3.32}$$

A very important result is that the mean square of $F(t)$ is equal to the integral of the spectral density for positive frequencies

$$\langle F^2 \rangle = K(0) = \int_{-\infty}^{+\infty} J(\omega) dw = \int_{0}^{+\infty} J_+(\omega) dw \qquad (1.3.33)$$
$$J_+(\omega) = 2J(\omega)$$

One interesting example of the spectral density is that of the voltage fluctuations across a resistor that was studied by Nyquist. The mean square voltage noise in a resistor is

$$\langle V^2 \rangle = \int_{0}^{\infty} J_+(\omega) d\omega \qquad (1.3.34)$$

and the resistance, from the fluctuation dissipation theorem, is

$$\begin{aligned} R &= \frac{1}{2k_BT} \int_{-\infty}^{\infty} \langle V(0)V(s) \rangle_0 ds \\ &= \frac{\pi}{k_BT} J(0) \end{aligned} \qquad (1.3.35)$$

If the correlation time τ^* of the force is small and thus the correlation function is peaked near $s = 0$, then for $\omega << \frac{1}{\tau^*}$

$$J(\omega) = J(0) = \frac{1}{\pi} k_BTR \qquad (1.3.36)$$

This produces a spectral density that is independent of frequency and is called white noise.

Figure 1.3.2 The spectral density for a random force with a small correlation time.

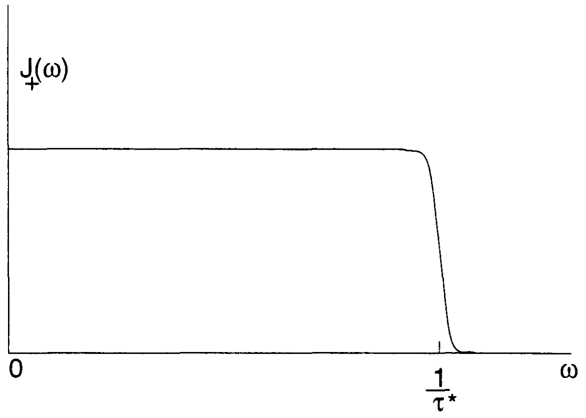

In a simple electrical circuit (see figure 1.3.3), the fluctuations in the current are due to the fluctuations in the emf. The equation for the current is

$$L\frac{dI}{dt} + RI + \frac{1}{C}\int I dt = V(t) \qquad (1.3.37)$$

If the voltage and current are decomposed into their frequency components $V_0(\omega)e^{i\omega t}$ and $I_0(\omega)e^{i\omega t}$, the complex impedance of the circuit is obtained

$$\begin{aligned} I_0(\omega) &= \frac{V_0(\omega)}{Z(\omega)} \\ Z(\omega) &= R + i\left(\omega L - \frac{1}{\omega C}\right) \end{aligned} \tag{1.3.38}$$

The fluctuations in the current then come from the fluctuations in the voltage divided by the impedance

$$\int_{-\infty}^{\infty} \left|I_0^2(\omega)\right| d\omega = \int_{-\infty}^{\infty} \frac{|V_0(\omega)|^2}{|Z(\omega)|^2} d\omega \tag{1.3.39}$$

The spectral density of the current is

$$\begin{aligned} I_0^2(\omega) &= \frac{V_0^2(\omega)}{R^2 + \left(\omega L - \frac{1}{\omega C}\right)^2} \\ &= \frac{\frac{2}{\pi} k_B T R}{R^2 + \left(\omega L - \frac{1}{\omega C}\right)^2} \; in\ amps^2/(radians/sec.) \end{aligned} \tag{1.3.40}$$

Figure 1.3.3 An electric circuit with resistance R, capacitance C and Inductance L.

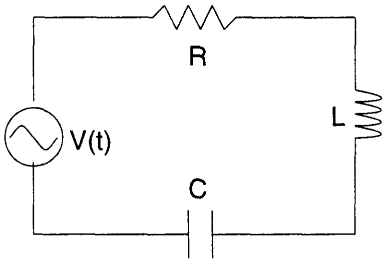

The spectral density calculated in equation 1.3.40 can be done for any system. This treatment of thermal noise in the frequency domain was generalized by Callen [8, 9] and is the approach that will be used in this thesis. The following section introduces the language that is used in the experimental field of gravitational wave detection.

1.4 Thermal Noise in a Harmonic Oscillator

A mathematically useful form to describe the loss associated with time-dependent strain in materials is to substitute a purely real Young's modulus with one that has both real and imaginary value (see for example Nowick [10]). If a stress

$$\sigma = \sigma_0 e^{i\omega t} \tag{1.4.1}$$

is imposed on a dissipative system, then the linearity of the stress-strain relationship causes the strain, ε, to be periodic with the same frequency

$$\varepsilon = \varepsilon_0 e^{i(\omega t - \phi(\omega))} \tag{1.4.2}$$

where ϕ is the loss angle by which the strain lags behind the stress. Similarly, if the strain is given, then the stress can be regarded as leading the strain by an angle ϕ. One can then define a complex modulus of the material as

$$M^*(\omega) = \sigma/\varepsilon = |M(\omega)| e^{i\phi(\omega)} \tag{1.4.3}$$

Since $\phi(\omega) << 1$, the modulus can be written

$$M(\omega) = \sigma/\varepsilon = M(\omega)(1 + i\phi(\omega)) \tag{1.4.4}$$

The maximum energy stored per unit volume is

$$W = \int_{\omega t=0}^{\pi/2} \sigma d\varepsilon = \frac{1}{2} M \varepsilon_0^2 \tag{1.4.5}$$

while the amount of energy dissipated in a cycle is

$$\Delta W = \pi M \phi \varepsilon_0^2 \tag{1.4.6}$$

The ratio of the energy dissipated by a cycle of motion to the stored energy is

$$\Delta W / W = 2\pi\phi \tag{1.4.7}$$

so that ϕ is called the internal friction of the material. The thermal noise spectrum for such a loss can be calculated using the Callen formulation of the Fluctuation-Dissipation Theorem.

A useful form of the Fluctuation-Dissipation theorem gives an expression for the thermal noise in a simple linear system (see Saulson [11] for a thorough review):

$$F_{thermal}^2(\omega) = 4k_B T R(\omega) \tag{1.4.8}$$

or

$$x_{thermal}^2(\omega) = \frac{4k_B T \sigma(\omega)}{\omega^2} \tag{1.4.9}$$

where

$$\begin{aligned} Z &= \frac{Force}{velocity} \\ R(\omega) &= Re(Z) \\ \sigma(\omega) &= Re(Z^{-1}) \end{aligned} \tag{1.4.10}$$

In this formulation, the power spectral density is expressed for the customary bandwidth of 1 Hz.

The damping term for internal friction is defined in terms of a loss angle $\phi(\omega)$ where:

$$\begin{aligned} F_{damping} &= -k(i\phi(\omega))x \\ F &= m\ddot{x} + k(1 + i\phi(\omega))x \\ Z &= \frac{k\phi(\omega)}{\omega} + i\left(m\omega - \frac{k}{\omega}\right) \\ \sigma &= \frac{k\phi(\omega)\,\omega}{\left(k - m\omega^2\right)^2 + k^2\phi^2(\omega)} \end{aligned} \tag{1.4.11}$$

and the thermal noise spectrum is:

$$\begin{aligned} F^2(\omega) &= 4k_BTm\omega_o^2\frac{\phi(\omega)}{\omega} \\ x^2(\omega) &= \left(\frac{4k_BT}{m}\right)\left(\frac{\phi(\omega)}{\omega}\right)\frac{\omega_o^2}{\left(\omega_o^2 - \omega^2\right)^2 + \phi^2(\omega)\,\omega_o^4} \end{aligned} \tag{1.4.12}$$

In many instances, the loss in certain materials is dominated by a single relaxation process of characteristic time τ and a dimensionless relaxation strength Δ (see for example [10]). Δ is defined as the ratio of two quantities that can be measured in the creep of a bulk material after the application of a step function stress σ_0 and is given by

$$\Delta = \frac{\delta J}{J_U} \tag{1.4.13}$$

where

$$J_U = J(t = 0) = \frac{\varepsilon(t = 0)}{\sigma_0} \tag{1.4.14}$$

is the instantaneous compliance upon application of a unit stress and measures the deformation when no time is allowed for relaxation. $\delta J = J_R - J_U$ is the relaxation of the compliance and is a measure of the total additional compliance that occurs after the application of the stress. $J_R = J(t = \infty)$ is the relaxed compliance and measures the final equilibrium value for the compliance.

The Young's modulus becomes

$$\begin{aligned} E^* &= E_0\left[\left(1 + \Delta\frac{(\omega\tau)^2}{1 + (\omega\tau)^2}\right) + i\left(\Delta\frac{(\omega\tau)^2}{1 + (\omega\tau)^2}\right)\right] \\ &= E_0\left[1 + i\left(\Delta\frac{\omega\tau}{1 + (\omega\tau)^2}\right)\right], \ \Delta << 1 \end{aligned} \tag{1.4.15}$$

The internal friction in this case has an explicit frequency dependence

$$\phi(\omega) = \Delta\frac{\omega\tau}{1 + (\omega\tau)^2} \tag{1.4.16}$$

and is called the Debye model for a single relaxation process.

The losses in solids can be due to many different relaxation mechanisms. The relaxation time τ often obeys the Arrhenius equation

$$\tau^{-1} = \nu_0 e^{-\Delta E/k_B T} \tag{1.4.17}$$

where ΔE is an activation energy in the relaxation process and ν_0 is a constant relating rate at which the activation barrier crossing is attempted. If one loss mechanism is dominant, but has a spread of activation energies, the loss angle ϕ is constant over a wide frequency band and is called structure damping [12]. If the fraction of activation energy Q between Q and $Q + dQ$ is given by $f(Q)dQ$, then the internal friction will be

$$\begin{aligned} \phi(\omega) &= \Delta \int_0^\infty dQ f(Q) \frac{\omega\tau}{1 + (\omega\tau)^2} \\ &= \Delta \int_0^\infty dQ f(Q) \frac{\omega\tau_0 e^{Q/k_B t}}{1 + \left(\omega\tau_0 e^{Q/k_B t}\right)^2} \end{aligned} \tag{1.4.18}$$

The integrand is sharply peaked about

$$Q_m = -k_B T \ln(\tau_0 \omega) \tag{1.4.19}$$

with a corresponding

$$\tau_m = \tau_0 e^{Q_m/k_B T} \tag{1.4.20}$$

determined by $\tau_m \omega = 1$. If $f(Q)$ varies little over a range of $k_B T$, equation 1.4.18 becomes

$$\phi(\omega) \approx \Delta f(Q_m) \int_0^\infty dQ \frac{\omega\tau}{1 + (\omega\tau)^2} \tag{1.4.21}$$

By making the replacement $z = \tau/\tau_m$, the above integral becomes

$$\phi(\omega) = \Delta f(Q_m) k_B T \int_\delta^\infty dz \frac{1}{1 + z^2} \tag{1.4.22}$$

where

$$\delta = e^{-Q_m/k_B T} \tag{1.4.23}$$

Since $Q_m >> k_B T$, the integral in equation 1.4.22 becomes

$$\phi(\omega) = \Delta \frac{\pi}{2} k_B T f[-k_B T \ln(\tau_0 \omega)] \tag{1.4.24}$$

For a frequency independent internal friction between 1 Hz and 10^7 Hz, the spread in energy of Q must be

$$k_B T \ln\left(10^7\right) = 16.1 k_B T = 0.4\ eV \tag{1.4.25}$$

Another well known model for the damping term in a simple harmonic oscillator is velocity or viscous damping. Viscous damping has a force that is proportional to velocity:

$$\begin{aligned} F_{damping} &= -\beta \dot{x} \\ F &= m\ddot{x} + \beta\dot{x} + kx \\ Z &= \beta + i\left(m\omega - \frac{k}{\omega}\right) \\ \sigma &= \frac{\beta\omega^2}{\beta^2\omega^2 + \left(m\omega^2 - k\right)^2} \end{aligned} \tag{1.4.26}$$

and a thermal noise spectrum:

$$\begin{aligned} F^2(\omega) &= 4k_BT\beta \\ x^2(\omega) &= \left(\frac{4k_BT}{m}\right)\frac{\frac{\beta}{m}}{(\omega^2 - \omega_0^2)^2 + \left(\frac{\beta\omega}{m}\right)^2} \end{aligned} \tag{1.4.27}$$

It is clear that viscous damping is a form of internal friction where ϕ has a frequency dependence of the form:

$$\phi_{viscous}(\omega) = \frac{\beta\,\omega}{m\,\omega_0^2} \tag{1.4.28}$$

The frequency dependence of the thermal noise for different sides of the resonant frequency has interesting characteristics depending on the model (see table 1.4.1). The Q (quality factor) which is defined as the number of radians through which the system oscillates before its energy decays by a factor of 1/e also has a different frequency dependence for each model. All the systems being considered have low losses and consequently Q>>1.

Table 1.4.1 Frequency dependence and Q for viscous and structure damping

Property	viscous	structure
Q	$\frac{m\omega_0}{\beta}$	$\frac{1}{\phi}$
ϕ	$\frac{\omega\beta}{m\omega_0^2}$	ϕ
$\omega << \omega_0$	$x^2(\omega) \propto const.$	$x^2(\omega) \propto \frac{1}{\omega}$
$\omega >> \omega_0$	$x^2(\omega) \propto \frac{1}{\omega^4}$	$x^2(\omega) \propto \frac{1}{\omega^5}$

There are several interesting results to discuss when attempting to find the best way to minimize the thermally driven displacement noise in a mechanical system. While there is always k_BT of energy in each mode, the distribution of this energy in frequency depends upon the resonant frequency and the Q of the material. The most obvious prescription is to choose the mass of the system to be as large as possible while at the same time insuring that the resonant frequency is not in the frequency band of experimental interest. In most cases, since the frequency decreases with increased mass, this is mutually incompatible for one structure and some compromise must be made.

The next step is to use as high a Q material as possible. This puts as much of the $k_B T$ energy as possible in a very narrow band around the resonant frequency. This feature can be removed in the data processing with the appropriate use of a notch filter. Cooling the system is problematic since the amplitude of the noise is proportional to the square root of temperature and the only way to achieve any significant difference is to go to very low temperatures on the order of microKelvin. This requires an elaborate experimental set up. In interferometers, this is especially problematic since the light power lost in the mirrors must also be removed.

1.5 Previous Measurements of Thermal Noise

Thermal noise has been seen in many different types of systems. A well known example is the Johnson noise of a resistor where the voltage noise spectral density across a resistor is:

$$V_{thermal}^2(f) = 4k_B T R \tag{1.5.1}$$

Another example is the Brownian motion of small particles. In macroscopic mechanical systems, the effect of thermal noise has never been seen except at some resonant frequency of the system.

Some of the earliest precision mechanical measurements were made using quartz torsion fibre balances. They include the Roll, Krotkov and Dicke [13] repeat of the Eőtvős experiment and various LaCoste gravimeter experiments to measure normal modes of the Earth [4], [14]. In all of these experiments, noise sources other than thermal dominated and limited the sensitivity of these instruments.

Another obvious high precision measurement where thermal noise could be seen is the detection of gravity waves. Acoustic gravity wave detectors are limited by the on-resonance thermal noise with their current sensitivities. In interferometric detectors, the Garching group [15], the 1.5 m MIT prototype [16] and the LIGO 40m prototype [17] have seen the thermal noise at the resonant peaks.

1.6 Thesis Outline

This thesis will study the thermal noise in gravity wave detectors due to the suspension of the test masses and the internal normal modes of the test masses.

Chapter 2 discusses the thermal noise from the mechanical losses in the fibers that suspend the test masses. It includes a discussion of the thermoelastic damping model, experimental results from measuring the Q's of wires made from different materials and predictions for the thermal noise in LIGO test mass suspensions.

The rest of the thesis describes an experiment to measure the off resonance thermal noise spectrum in fused quartz. Chapter 3 studies the thermal noise in a thin plate of fused quartz. Chapter 4 gives a detailed description of the optical interferometer design. Chapter 5 presents the results of the experiment. Chapters 6 and 7 discuss the possible experimental and mechanical sources for the measured noise. Chapter 8 describes future experiments to gain a better understanding of the measured noise.

Chapter 9 gives a microscopic model of how the loss mechanisms in a bulk piece of fused quartz produce thermal noise. There is a description of an experiment that tests this model.

Finally, chapter 10 presents methods to measure the thermal noise in test masses directly.

Chapter 2 Mechanical Loss in Fibres

2.1 Thermal Noise in a Pendulum Supported by a Thin Fibre

The mass that holds a mirror of the gravity wave interferometer is suspended from a thin fibre to produce a pendulum. The transfer function of the pendulum provides a filter for seismic noise above the pendulum frequency:

$$\frac{x_{out}(f)}{x_{in}(f)} = \frac{f_0^2}{f^2},\ f >> f_0 \tag{2.1.1}$$

This combined with a typical seismic spectrum of:

$$x_{seismic}(f) \approx \frac{10^{-5} cm/\sqrt{Hz}}{f^2},\ f > 10Hz \tag{2.1.2}$$

offers some isolation from seismic noise. Unfortunately, the fibres are flexural members and any mechanical loss from bending will not only degrade the Q of the pendulum, but also introduce thermal noise.

The equation (see for example [18]) for a member that is clamped at one end to a fixed object and on the other end to a free mass is (see figure 2.1.1):

$$\begin{gathered}
y(x) = \alpha(x - x_0) + \alpha x_0 e^{-\frac{x}{x_0}} \\
x_0 = \left(\frac{n\, EA\kappa^2}{mg}\right)^{\frac{1}{2}} \\
E = Young's\ modulus \\
A = \pi a^2 = cross\ section\ of\ member \\
\kappa = radius\ of\ gyration\ of\ member \\
\kappa^2 = \frac{1}{A}\int z^2 dA = \frac{a^2}{4} \\
n = \#\ of\ fibers\ supporting\ mass \\
m = pendulum\ mass
\end{gathered} \tag{2.1.3}$$

Figure 2.1.1 Pendulum supported by a thin flexural member

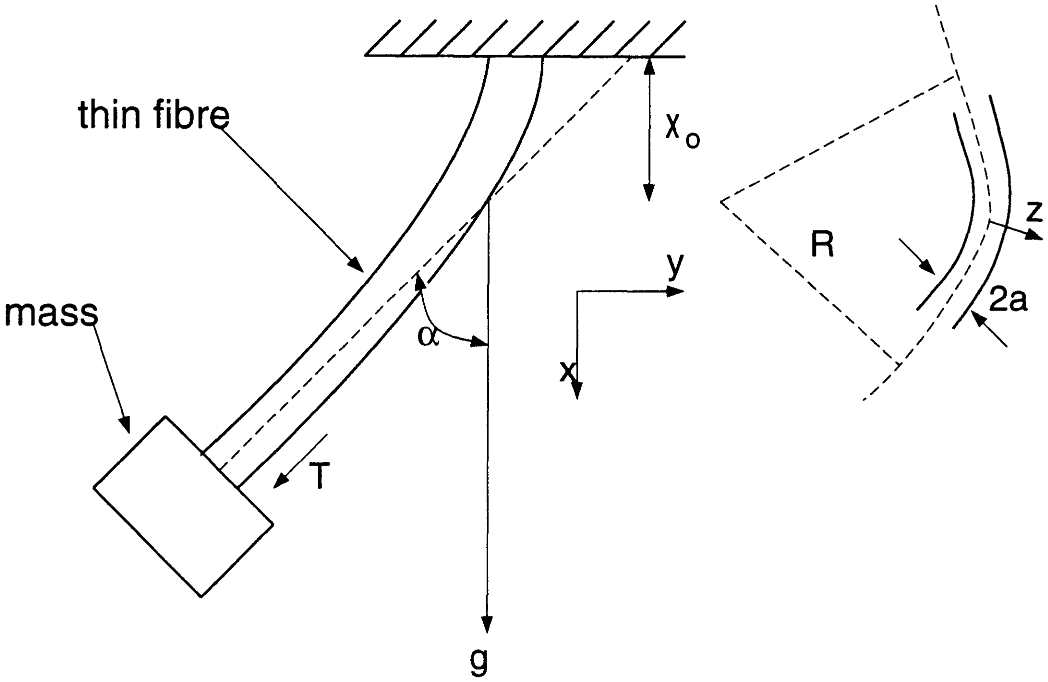

In order to use the fluctuation-dissipation theorem as expressed by Callen, one must obtain the real part of the impedance of the fibre. First, the Young's modulus must be expressed with a complex component

$$E^* = E(1 + i\phi_{mat}(\omega)) \tag{2.1.4}$$

so that

$$x_0 = \frac{a^2}{2}\left(\frac{\pi n E}{mg}\right)^{\frac{1}{2}}\left(1 + +i\frac{\phi_{mat}(\omega)}{2}\right) \tag{2.1.5}$$

The shearing force is

$$\begin{aligned} F &= -E\frac{\pi a^4}{4}\frac{\partial^3 y}{\partial x^3} \\ &= E\frac{\pi a^4}{4x_0^2}\alpha e^{-\frac{x}{x_0}} \\ &= \alpha\frac{mg}{n} \end{aligned} \tag{2.1.6}$$

The velocity of a fibre with length l is

$$\frac{dy}{dt} \approx i\omega(l - 2x_0)\alpha \tag{2.1.7}$$

The impedance of the string is then

$$\begin{aligned} Z &= \frac{F}{v} = -i\frac{mg}{n\omega(l - 2x_0)} \\ &\approx i\frac{mg}{n\omega l}\left(1 + 2\frac{x_0}{l}\right) \\ &= i\frac{mg}{n\omega l}\left(1 + \frac{a^2}{l}\left(\frac{\pi n E}{mg}\right)^{\frac{1}{2}}\left(1 + i\frac{\phi_{mat}(\omega)}{2}\right)\right) \end{aligned} \tag{2.1.8}$$

The equation of motion for a pendulum is

$$v(\omega) = \frac{F(\omega)}{Z_{mass} + Z_{string}}$$

$$\begin{aligned} v(\omega) &= \frac{F(\omega)}{(Z_{mass} + Z_{string})} \\ &= \frac{F(\omega)}{\left(i\omega m - i\frac{mg}{n\omega l}\left(1 + 2\frac{|x_0|}{l}\left(1 + i\frac{\phi_{mat}(\omega)}{2}\right)\right)\right)} \\ &= \frac{F(\omega)\omega}{m\left(i\left(\omega^2 - \omega_0^2\left(1 + 2\frac{|x_0|}{l}\right)\right) + \omega_0^2\frac{|x_0|}{nl}\frac{\phi_{mat}(\omega)}{2}\right)} \end{aligned} \tag{2.1.9}$$

The resonant frequency of the pendulum is

$$\begin{aligned} \omega_0^2 &= \frac{g}{l} \\ {\omega'_0}^2 &= \frac{g}{l}\left(1 + 2\frac{|x_0|}{l}\right) \approx \omega_0^2 \end{aligned} \tag{2.1.10}$$

The real part of Z^{-1} is

$$\begin{aligned} \sigma(\omega) &= \frac{\omega_0^2\omega|x_0|}{2nlm}\frac{\phi_{mat}(\omega)}{\left(\left(\omega^2 - \omega_0^2\right)^2 + \frac{\omega_0^4|x_0|^2\phi_{mat}^2(\omega)}{4n^2l^2}\right)} \\ &= \frac{\omega_0^2\omega a^2}{4nlm}\left(\frac{\pi nE}{mg}\right)^{\frac{1}{2}}\frac{\phi_{mat}(\omega)}{\left(\left(\omega^2 - \omega_0^2\right)^2 + \frac{\omega_0^4a^4\phi_{mat}^2(\omega)}{16n^2l^2}\left(\frac{\pi nE}{mg}\right)\right)} \end{aligned} \tag{2.1.11}$$

The thermal noise will be

$$\begin{aligned} x^2(\omega) &= \frac{4k_BT}{\omega^2}\sigma(\omega) \\ &= \frac{k_BT}{\omega}\frac{\omega_0^2a^2}{nlm}\left(\frac{\pi nE}{mg}\right)^{\frac{1}{2}}\frac{\phi_{mat}(\omega)}{\left(\left(\omega^2 - \omega_0^2\right)^2 + \frac{\omega_0^4a^4\phi_{mat}^2(\omega)}{16n^2l^2}\left(\frac{\pi nE}{mg}\right)\right)} \\ &= \frac{k_BT\omega_0^4a^2\pi^{\frac{1}{2}}E^{\frac{1}{2}}}{(mg)^{\frac{3}{2}}n^{\frac{1}{2}}}\frac{\phi_{mat}(\omega)}{\omega}\frac{1}{\left(\left(\omega^2 - \omega_0^2\right)^2 + \frac{\omega_0^8a^4E\pi\phi_{mat}^2(\omega)}{16g^3nm}\right)} \end{aligned} \tag{2.1.12}$$

Another way to obtain the loss in the pendulum and hence, its thermal noise is to compare the power dissipated in the flexure to the power dissipated in the pendulum and to compare the energy stored in the flexure and the energy stored in the pendulum.

The energy stored in the flexure is:

$$\begin{aligned} E_{elastic} &= \frac{1}{2}AE\kappa^2\int_0^l\left[\frac{\partial^2y}{\partial x^2}\right]^2dx \\ &= \frac{1}{4}\left(\frac{mg}{n}EA\kappa^2\right)^{\frac{1}{2}}\alpha^2 \\ &= \frac{a^2}{8}\left(\pi\frac{mg}{n}E\right)^{\frac{1}{2}}\alpha^2 \end{aligned} \tag{2.1.13}$$

The gravitational energy stored in the pendulum is:

$$E_{gravitational} = \frac{1}{2} mgl\alpha^2 \tag{2.1.14}$$

The pendulum is a harmonic oscillator that follows the equation

$$\alpha(t) = \alpha e^{i\omega_0 t} \tag{2.1.15}$$

The power lost in each member due to flexure is

$$\begin{aligned} P &= \langle F \times v \rangle \\ &= \left\langle -(i\phi_{mat}(\omega)) \frac{E\pi a^4}{4} \int_0^l \frac{\partial^4 y}{\partial x^4} \times i\omega_0 y dx \right\rangle \\ &= \frac{a^2}{8} \left(\frac{\pi m g E}{n} \right)^{\frac{1}{2}} \omega_0 \alpha^2 \phi_{mat}(\omega) \end{aligned} \tag{2.1.16}$$

The power lost by the pendulum is

$$\begin{aligned} P &= \langle F \times v \rangle \\ &= \langle -k(i\phi_{pend}(\omega)) y \times v \rangle \\ &= \langle -m\omega_0^2 (i\phi_{pend}(\omega)) \alpha l e^{i\omega_0 t} \times i\omega_0 \alpha l e^{i\omega_0 t} \rangle \\ &= \frac{1}{2} m\omega_0^3 \alpha^2 l^2 \phi_{pend}(w) \end{aligned} \tag{2.1.17}$$

Since the loss in the pendulum is entirely due to the loss of the flexure (the gravitational field that stores most of the pendulum's energy is lossless), the internal friction of the pendulum is

$$\begin{aligned} \frac{1}{2} m\omega_0^3 \alpha^2 l^2 \phi_{pend}(\omega) &= \frac{a^2}{8} \left(\frac{\pi m g E}{n} \right)^{\frac{1}{2}} \omega_0 \alpha^2 \phi_{mat}(\omega) \\ \phi_{pend}(\omega) &= \frac{a^2}{4l} \left(\frac{\pi E}{n\, mg} \right)^{\frac{1}{2}} \phi_{mat}(\omega) \end{aligned} \tag{2.1.18}$$

Alternatively, one can equate the losses of the pendulum to the ratio of the energy stored in the flexure (which losses an amount proportional to $1/Q_{mat}$ in each cycle) to that stored in the gravitational field and obtain the same result

$$\begin{aligned} \frac{E_{pend}}{Q_{pend}} &= \frac{E_{mat}}{Q_{mat}} \\ Q_{pend} &= Q_{mat} \frac{4l}{a^2} \left(\frac{nmg}{\pi E} \right)^{\frac{1}{2}} \end{aligned} \tag{2.1.19}$$

The thermal noise due to the loss in the flexure for one member can be obtained by putting the pendulum loss in equation 1.4.12. It gives the same answer as that obtained in equation 2.1.12.

$$\begin{aligned}
x^2_{thermal}(\omega) &= \left(\frac{4k_BT}{m}\right)\left(\frac{\phi_{pend}(\omega)}{\omega}\right)\frac{\omega_0^2}{\left(\omega_0^2-\omega^2\right)^2+\phi^2_{pend}(\omega)\omega_0^4} \\
&= \frac{k_BT\,a^2\,\omega_0^4\,E^{\frac{1}{2}}\pi^{\frac{1}{2}}}{(mg)^{\frac{3}{2}}n^{\frac{1}{2}}}\;\frac{\phi(\omega)_{material}}{\omega}\frac{1}{\left(\omega_0^2-\omega^2\right)^2+\left(\frac{\phi^2(\omega)\omega_0^8a^4E\pi}{16\,g^3n\,m}\right)}
\end{aligned} \tag{2.1.20}$$

For $\omega >> \omega_0$, the expression is:

$$\begin{aligned}
x^2_{thermal}(\omega) &= \frac{k_BT\,a^2\,\omega_0^4\,E^{\frac{1}{2}}\pi^{\frac{1}{2}}}{(mg)^{\frac{3}{2}}n^{\frac{1}{2}}}\,\phi(\omega)_{material}\,\frac{1}{\omega^5} \\
&= \frac{k_BT\;\omega_0^4\,E^{\frac{1}{2}}}{\pi^{\frac{1}{2}}(mg)^{\frac{1}{2}}n^{\frac{3}{2}}S_{max}}\,\phi(\omega)_{material}\,\frac{1}{\omega^5}
\end{aligned} \tag{2.1.21}$$

where S_{max} is the yield strength of the wire. The total thermal noise from all n members is just $\sqrt{n}$ times the thermal noise from each member or the thermal noise of each member added in quadrature.

2.2 Loss Mechanisms in Fibres: Thermoelastic Damping

There are many ways to model the mechanisms that contribute to mechanical loss in a solid. The Debye model for single relaxation processes has an explicit frequency dependence and has the form (see for example Nowick [10]):

$$\phi(\omega) = \Delta\frac{\omega\tau}{1+(\omega\tau)^2} \tag{2.2.1}$$

where Δ is the relaxation strength and τ is the relaxation time.

One such process is thermoelastic damping as described by Zener [19, 20] where the parameters are

$$\begin{aligned}
\Delta &= \frac{E\alpha^2T}{C_V} \\
\tau &= \frac{d^2}{2\pi\,2.16D}\;(circular\ beam) \\
\tau &= \frac{a^2}{\pi^2\,D}\;(rectangular\ beam\ thickness = a) \\
D &= \frac{\kappa}{C_V} \\
E &= Young's\ modulus \\
\alpha &= linear\ coefficient\ of\ thermal\ expansion \\
C_V &= specific\ heat\ per\ unit\ volume \\
\kappa &= thermal\ conductivity \\
T &= temperature
\end{aligned} \tag{2.2.2}$$

The physical interpretation of this model involves heat transfer across a thin fiber. The heat transfer depends upon the thermal conductivity of the material while the compression and expansion of the fibre (which generates the work) depends upon the frequency of oscillation. If the period of oscillation matches the heat transfer period, the dissipation is maximized.

Figure 2.2.1 $x^2(\omega)$ for different frequency limits.

	$\omega << \omega_0$	$\omega >> \omega_0$
$\omega << \tau^{-1}$	$\left(\frac{4k_BT}{m}\right)\left(\frac{\Delta\tau}{\omega_0^2}\right)$	$\left(\frac{4k_BT}{m}\right)\left(\Delta\omega_0^2\tau\right)\frac{1}{\omega^4}$
$\omega \approx \tau^{-1}$	$\left(\frac{4k_BT}{m}\right)\frac{\Delta\tau}{\omega_0^2}\left(\frac{1}{1+(\omega\tau)^2}\right)$	$\left(\frac{4k_BT}{m}\right)\frac{\Delta\omega_0^2\tau}{\omega^4}\left(\frac{1}{1+(\omega\tau)^2}\right)$
$\omega >> \tau^{-1}$	$\left(\frac{4k_BT}{m}\right)\left(\frac{\Delta}{\omega_0^2\tau}\right)\frac{1}{\omega^2}$	$\left(\frac{4k_BT}{m}\right)\left(\frac{\Delta\omega_0^2}{\tau}\right)\frac{1}{\omega^6}$

It is of pedagogical interest to relate this loss to the motions induced in the fibre by statistical temperature fluctuations inducing small changes in the length of the fibre about the neutral line and hence, stresses in the fibre.

Figure 2.2.2 Sketch of how a temperature fluctuation causes a motion of the fibre.

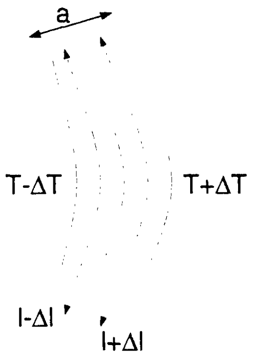

The differential of the Gibbs free energy per unit volume is (see for example Nowick [10])

$$dg = -sdT - \varepsilon d\sigma \tag{2.2.3}$$

From this equation one can obtain the cross relationship

$$\left(\frac{\partial s}{\partial \sigma}\right)_T = \left(\frac{\partial \varepsilon}{\partial T}\right)_\sigma = \alpha \tag{2.2.4}$$

where α is the coefficient of linear expansion. The relationship between temperature and entropy is

$$\left(\frac{\partial s}{\partial T}\right)_\sigma = \frac{C_V}{T} \tag{2.2.5}$$

and the relationship between temperature and strain is

$$\left(\frac{\partial T}{\partial \sigma}\right)_s = -\frac{\left(\frac{\partial s}{\partial \sigma}\right)_T}{\left(\frac{\partial s}{\partial T}\right)_\sigma} = \frac{-\alpha T_0}{C_V} \tag{2.2.6}$$

where C_V is the specific heat per unit volume. The strain can be expanded about $\sigma = \varepsilon = 0$; $T = T_0$

$$\begin{aligned}\varepsilon(\sigma, T) &= \left(\frac{\partial \varepsilon}{\partial \sigma}\right)_T \sigma + \left(\frac{\partial \varepsilon}{\partial T}\right)_\sigma (T - T_0) \\ &= J_R \sigma + \alpha \Delta T\end{aligned} \tag{2.2.7}$$

where J_R is the relaxed compliance (see equation 1.4.14 for a definition of both the relaxed and unrelaxed compliance J_U). The differential form of the enthalpy is

$$dh = -\varepsilon d\sigma + T ds \tag{2.2.8}$$

which gives

$$\left(\frac{\partial \varepsilon}{\partial s}\right)_\sigma = -\left(\frac{\partial T}{\partial \sigma}\right)_s = \frac{\alpha T_0}{C_V} \tag{2.2.9}$$

The strain can then be written

$$\varepsilon = J_U \sigma + \left(\frac{\alpha T_0}{C_V}\right) \Delta s \tag{2.2.10}$$

The temperature can be expanded in terms of s and σ

$$\begin{aligned}\Delta T &= \left(\frac{T_0}{C_V}\right)(\Delta s - \alpha \sigma) \\ &= \left(\frac{T_0}{C_V}\right)(\Delta s - \overline{\Delta s})\end{aligned} \tag{2.2.11}$$

where $\overline{\Delta s}$ is the equilibrium value of the entropy for $\Delta T = 0$.

The heat flow across the neutral line will follow a diffusion equation

$$\frac{dq}{dt} = \kappa \nabla^2 T \tag{2.2.12}$$

Using equation 2.2.12 and

$$\frac{dq}{dt} = T \frac{d(\Delta s)}{dt} \tag{2.2.13}$$

gives a new diffusion equation in terms of the entropy

$$\frac{d(\Delta s)}{dt} = D \nabla^2 (\Delta s - \overline{\Delta s}) \tag{2.2.14}$$

where $D = \kappa / C_V$ and is called the thermal diffusivity.

The entropy can be written in terms of time dependent and spatially dependent orthonormal functions

$$\Delta s = \sum_n \Delta s_n(t) U_n(x,y,z) \tag{2.2.15}$$

The spatial eigenfunctions are solutions to the equation

$$\nabla^2 U + \xi U = 0 \tag{2.2.16}$$

For a rectangular ribbon with thickness a, the boundary condition is that there is no heat flow out of the ribbon or

$$\frac{dU}{dx} = 0,\ x = \pm a/2 \tag{2.2.17}$$

The solution of this equation is

$$\begin{aligned} U_n &= \left(\frac{2}{a}\right)^{\frac{1}{2}} \sin\left[(2n+1)\frac{\pi x}{a}\right] \\ \xi_n &= \left[\frac{(2n+1)\pi}{a}\right]^2 \end{aligned} \tag{2.2.18}$$

The time dependent equation for the entropy can be written

$$\begin{aligned} \frac{d(\Delta s_n)}{dt} &= \frac{-(\Delta s_n - \overline{\Delta s_n})}{\tau_n} \\ \tau_n^{-1} &= D\xi \end{aligned} \tag{2.2.19}$$

This is the same time constant from the Zener thermoelastic damping model. The solution of the above equation is

$$\begin{aligned} \Delta s_n &= A e^{-\frac{t}{\tau_n}} + \overline{\Delta s_n}\left(\frac{t}{\tau_n}\right) \\ &= \alpha\sigma\left(\frac{t}{\tau_n}\right) \end{aligned} \tag{2.2.20}$$

The entropy thus increases linearly with time. The stress is due to the length change caused by the temperature fluctuation

$$\sigma = E\frac{\Delta l}{l} = E\alpha\Delta T \tag{2.2.21}$$

The change in energy that takes place is then the heat flow that causes the temperature difference

$$\begin{aligned} \Delta Energy &= (T + \Delta T)\Delta s - (T - \Delta T)\Delta s \\ &= 2\Delta T \Delta s \\ &= 2\alpha\sigma\left(\frac{t}{\tau_n}\right) \\ &= \frac{2\alpha^2 E (\Delta T)^2}{\tau_n} t \end{aligned} \tag{2.2.22}$$

The temperature fluctuations are (see Landau[21])

$$\left\langle (\Delta T)^2 \right\rangle = \frac{k_B T^2}{C_V} \tag{2.2.23}$$

The energy fluctuations are

$$\Delta Energy = \frac{2k_B T \alpha^2 E T}{\tau_n C_V} t \tag{2.2.24}$$

The fluctuation dissipation theorem gives the energy fluctuations as

$$\begin{aligned} \Delta Energy &= k_B \frac{t}{\tau_{correlation}} \\ \frac{1}{\tau_{correlation}} &\approx \frac{\omega}{Q} \approx \omega\phi \end{aligned} \tag{2.2.25}$$

Relating equations 2.2.24 and 2.2.25 gives the internal friction as

$$\phi = \frac{E\alpha^2 T}{C_v \omega \tau_n} \tag{2.2.26}$$

which is the same as that predicted by Zener's thermoelastic damping for $\omega\tau >> 1$. This result is a very clear example of the fluctuation dissipation theorem. In one case, bending of the fibre produces temperature changes in the fibre that dissipate due to thermal diffusion and hence, cause a loss. In the other case, temperature fluctuations cause fluctuations in length which in turn produce flexure in the fibre.

2.3 Experiment

An experiment to investigate the loss in fibres that might be suitable for the suspension of the test masses of LIGO was performed [22]. The materials studied included: tungsten, silicon, sapphire and fused quartz.

Table 2.3.2 Δ and D values for the materials considered

Material	Δ	D in cm/s^2
Tungsten	7.8×10^{-4}	0.61
Sapphire	9.1×10^{-4}	0.13
Silicon	1.1×10^{-4}	0.79
Fused Quartz	3.1×10^{-6}	0.16

The top of the fibre was clamped in various ways to an aluminum block. The bottom was left free. An electrostatic plate excited the bottom of the fibre by applying a sinusoidal potential of up to a kilovolt over a DC signal of up to a kilovolt at a resonant frequency

Figure 2.3.1 Sketch of apparatus used to measure losses in fibres.

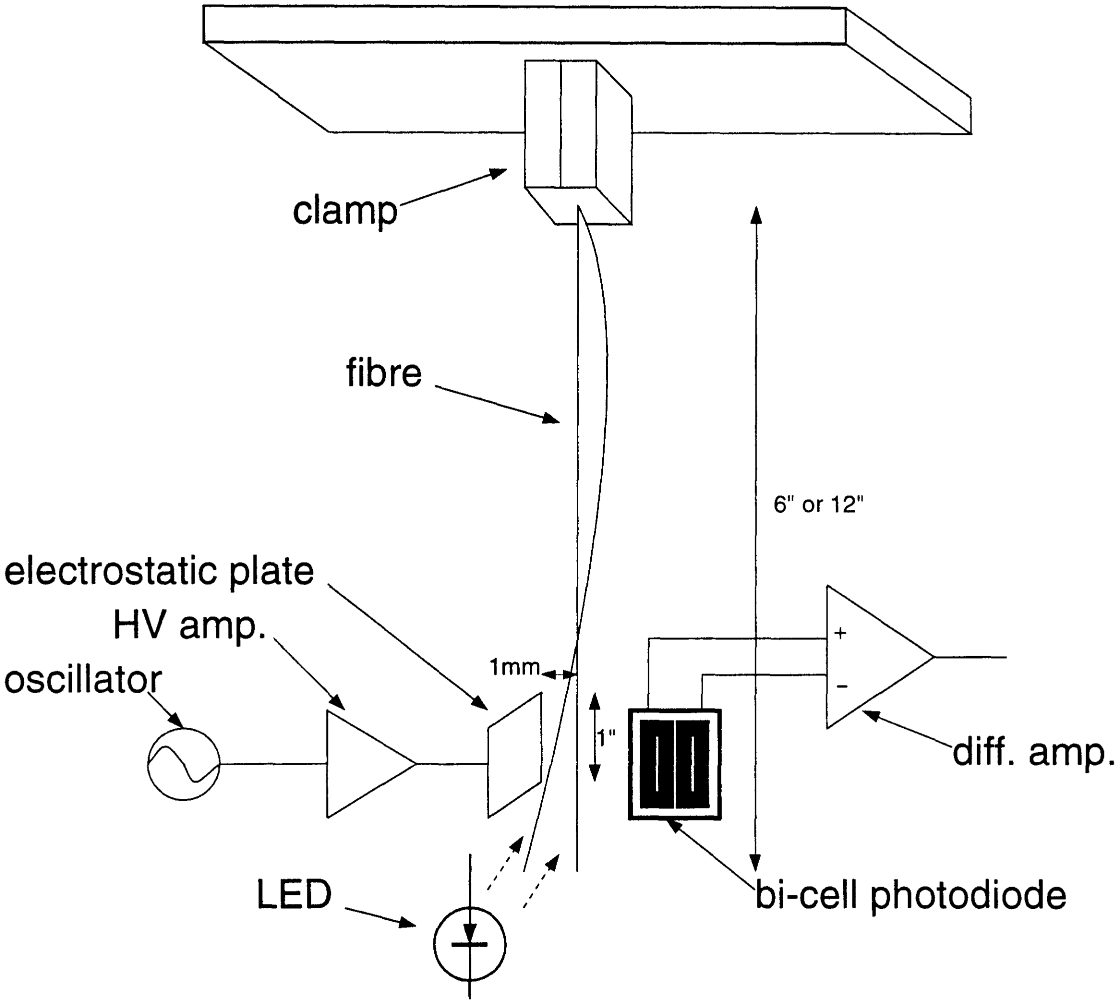

of a transverse mode of the fibre. An optical shadow detection system consisting of the fibre blocking the light from an LED shining onto a split photodiode measured the motion of the fibre (see figure 2.3.1).

The Q was measured in two ways: either by driving the fibre at its resonance frequency and looking at the FWHM of the resonance in the frequency domain with an FFT spectrum analyzer or by determining the envelope to the damped sinusoidal amplitude of the fibre's vibration during a free decay after the drive was turned off. The electrostatic drive could easily excite the fibre to an order of magnitude above the level at which it was driven by background vibrations. The envelope of the free decay was regularly checked for its exponential character to guard against non-linearities in the measurement process or the mechanical system.

The resonant frequencies of the fibres follow that of a stiff string (see for example Morse [23])

$$f_n = \frac{n}{2l}\sqrt{\frac{T}{\rho\pi a^2}}\left[1+\frac{2}{l}\sqrt{\frac{E\pi a^2\kappa^2}{T}}+\left(4+\frac{n^2\pi^2}{2}\right)\frac{E\pi a^2\kappa^2}{Tl^2}\right] \qquad (2.3.1)$$

The resonant frequency of the first mode of the fibre reduces to that of a wire hanging vertically by its own weight or a "chain" that neglects the stiffness of the wire

$$f_0 = \frac{1.2}{2\pi}\sqrt{\frac{g}{l}} \tag{2.3.2}$$

where l is the length of the wire. The frequencies of the higher modes reduce to that for a clamped beam that neglects gravity:

$$\begin{aligned} f_i &= \frac{\lambda_i^2}{2\pi l^2}\sqrt{\frac{EI}{m}} \\ \lambda_i^2 &= 1.875, 4.694, 7.855, 10.996. 14.923 \\ I &= \frac{\pi a^4}{4} \end{aligned} \tag{2.3.3}$$

Most of these modes were split from ellipticity in the fibre. Since most of the restoring force for the higher order modes comes from the flexure in the fibre, the Q measured is the actual Q of the material.

Gas damping was made negligible by placing the experiment inside a bell jar vacuum system that reached pressures below 10^{-5} torr. The supporting structure was much greater in mass than the fibre which made external damping from recoil negligible.

There was concern that friction due to rubbing in the clamp would be the dominant loss mechanisms. A number of steps were taken to reduce this possibility. The best strategy was to use a fibre drawn from a thick piece; the thick piece is easier to clamp than the thin fibre.

Figure 2.3.2 Q values for tungsten. The square boxes indicate the measurements for a wire 0.009″ in diameter and 10″ long that was clamped between two aluminum plates with the edges rounded in an attempt to reduce friction due to rubbing between the wire and the aluminum surface. The hexagonal and pentagonal boxes show the values for a 0.005″ diameter wire with a length of 10″ and 4″ respectively. The wire was spot welded to a thicker tungsten rod (0.126″ in diameter) that was clamped inside a tightly fitting hole in an aluminum block. The triangles are the results from a 0.059″ tungsten rod that was electrochemically etched to a wire with a thickness between 0.005″ and 0.010″ and length of 4″. The curves represent the theoretical values from thermoelastic damping (the pentagons represent 0.005″ diameter, square boxes 0.009″ and the triangles 0.015″).

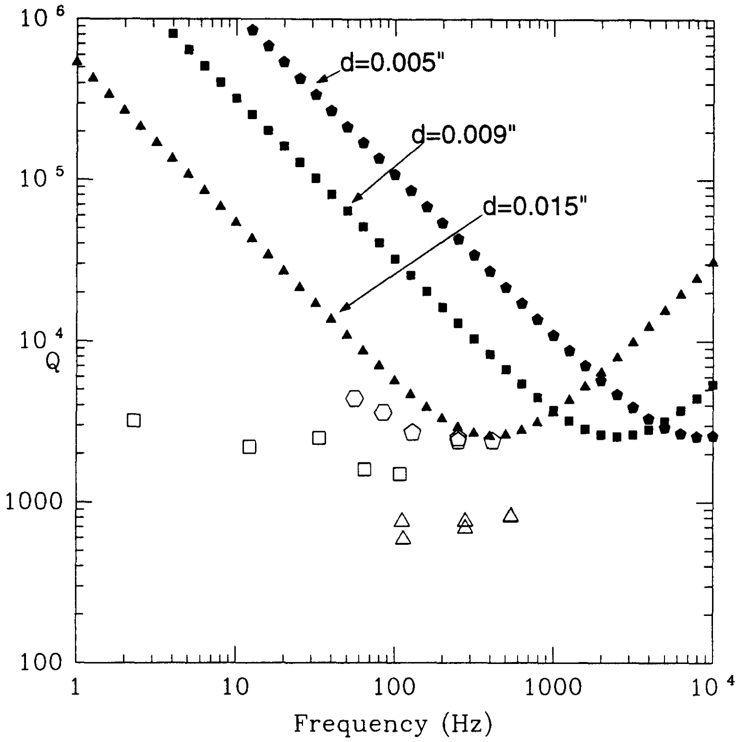

Figure 2.3.2 shows the results of measuring various tungsten wires. The square boxes indicate the measurements for a wire 0.009″ in diameter and 10″ long that was clamped between two aluminum plates with the edges rounded in an attempt to reduce friction due to rubbing between the wire and the aluminum surface. The hexagonal and pentagonal boxes show the values for a 0.005″ diameter wire with a length of 10″ and 4″ respectively. The wire was spot welded to a thicker tungsten rod (0.126″ in diameter) that was clamped inside a tightly fitting hole in an aluminum block. The triangles are the results from a 0.059″ tungsten rod that was electrochemically etched to a wire with a thickness between 0.005″ and 0.010″ and length of 4″. The curves represent the theoretical values from thermoelastic damping (the pentagons represent 0.005″ diameter, square boxes 0.009″ and the triangles 0.015″).

Figure 2.3.3 shows the Q of various sapphire samples. The squares are from a fibre 0.020″ in diameter and 10″ long that was clamped between two aluminum plates. The triangles are from a piece 0.009″ in diameter and 4″ long also held in an aluminum plate clamp. Finally, the pentagons comes from a fibre 0.0055″ thick and 3″ long that was welded to a thicker sapphire rod 0.030″ in diameter. The thick piece was press fitted into a tightly fitting hole in an aluminum block. The curves represent the values expected from thermoelastic damping.

Figure 2.3.3 Q values for sapphire. The squares are from a fibre 0.020″ in diameter and 10″ long that was clamped between two aluminum plates. The triangles are from a piece 0.009″ in diameter and 4″ long also held in an aluminum plate clamp. Finally, the pentagons comes from a fibre 0.0055″ thick and 3″ long that was welded to a thicker sapphire rod 0.030″ in diameter. The thick piece was press fitted into a tightly fitting hole in an aluminum block. The curves represent the values expected from thermoelastic damping (the pentagons represent 0.0055″ diameter, the triangles 0.009″ and the square boxes 0.020″).

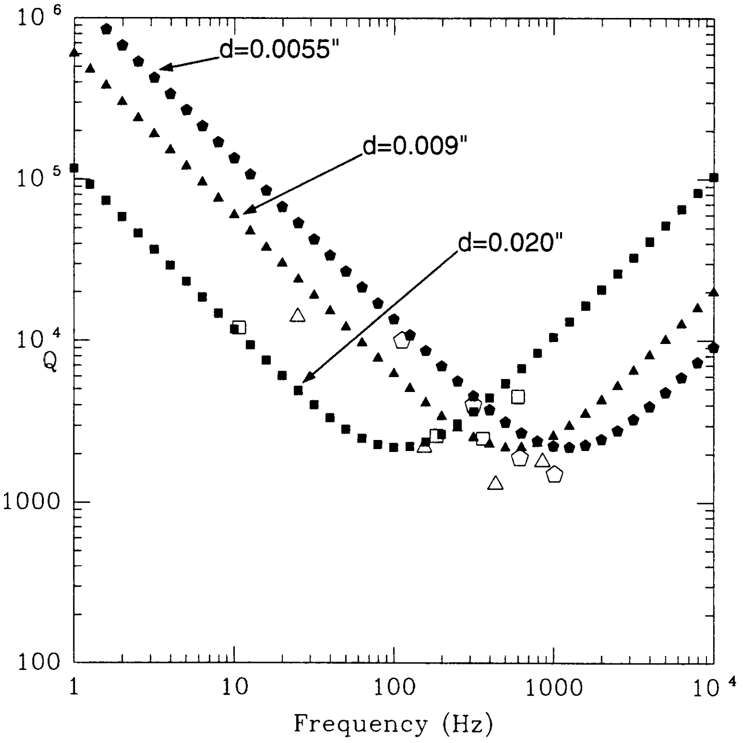

Figure 2.3.4 shows the results from a sample of silicon. A rod with a diameter 0.125″ was chemically etched to a fibre with thickness between 0.027″ and 0.035″ and a length of 4″. The rod end was clamped into an aluminum block. The curve represents the thermoelastic values for a piece 0.030″ in diameter.

Figure 2.3.4 Q values for silicon. A rod with a diameter 0.125″ was chemically etched to a fibre with thickness between 0.027″ and 0.035″ and a length of 4″. The rod end was clamped into an aluminum block. The curve represents the thermoelastic values for a piece 0.030″ in diameter.

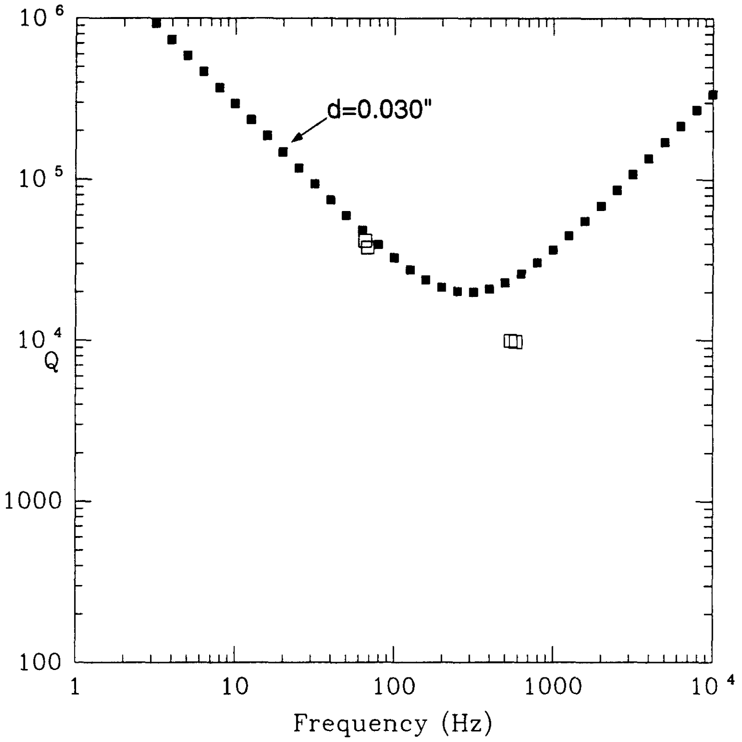

The last material measured, fused quartz, can be seen in figure 2.3.5. A series of 0.125″ fused quartz rods were pulled to make a fibre 3″ long and thicknesses of 0.009″ (pentagons), 0.015″(triangles) and 0.020″(squares). In each case, the rod end was clamped into an aluminum block. Again, the curves represent the predicted thermoelastic damping for each respective thickness.

Figure 2.3.5 Q values for fused quartz. A series of 0.125″ fused quartz rods were pulled to make a fibre 3″ long and thicknesses of 0.009″ (pentagons), 0.015″(triangles) and 0.020″(squares). In each case, the rod end was clamped into an aluminum block. Again, the curves represent the predicted thermoelastic damping for each respective thickness.

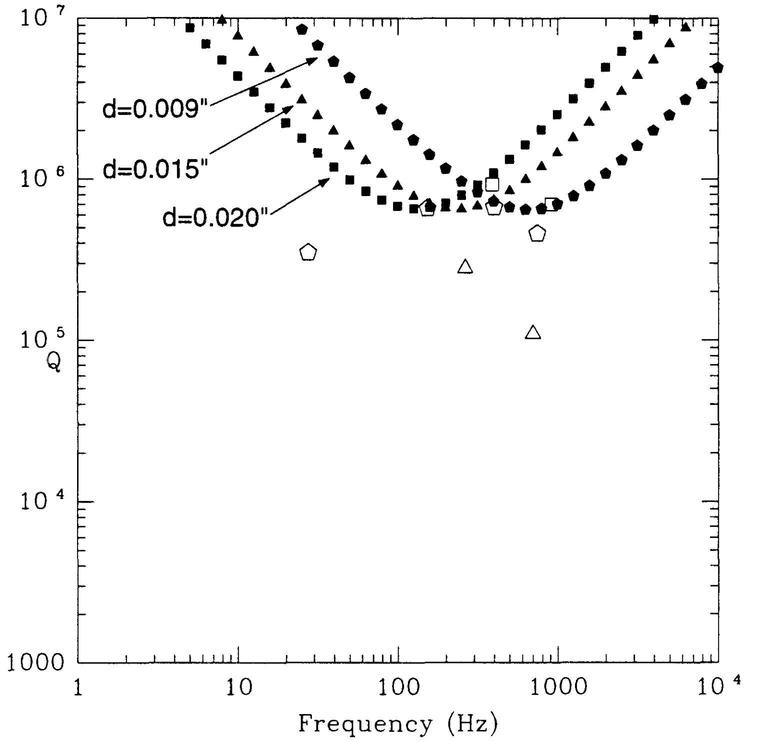

2.4 Discussion

With such a limited number of samples, it is only really possible to say that thermoelastic damping does give a good upper limit for the possible Q of the materials. By using thermoelastic damping as an estimate of the loss in fibres, one can determine a noise spectrum for a typical LIGO suspension. Figure 2.4.1 shows the predicted noise for a bifilar pendulum with m=10 kg and f_0=1 Hz. The square boxes are for tungsten with the wire at its yield strength (4×10^{10} dynes/cm^2) and the crosses are for fused quartz at its yield strength (4.8×10^{8} dynes/cm^2). While the fused quartz does have a higher Q, it is weaker than the tungsten and must have a larger thickness. This reduces the effectiveness of the lower loss by making the Q improvement from equation 2.1.19 worse.

Figure 2.4.1 Thermal noise from thermoelastic damping in a LIGO suspension for a 2 wire pendulum. The mass is 10kg and the resonant frequency 1 Hz (l=25 cm). The yield strength for tungsten (square boxes) was 4×10^{10} dynes/cm^2(d= 0.005″). The yield strength for fused quartz (crosses) was 4.8×10^8 dynes/cm^2 (d=0.045″).

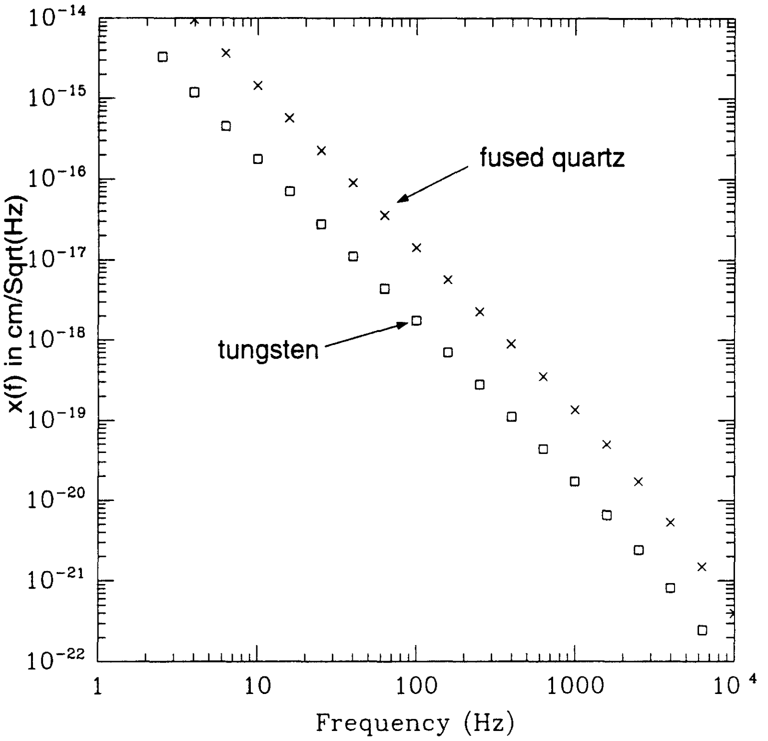

Chapter 3 Thermal Noise in a Thin Plate

3.1 Internal Thermal Noise

An interferometric gravity wave detector measures extremely small distances by reflecting laser beams from mirrors and comparing the phase accumulated by two beams that travel orthogonal to one another (see figure 1.1.1). If these mirrors have their own independent random motion, this will create a path change for the light that can look like a gravity wave signal. One such motion is introduced by thermal noise from the suspension system that holds the mirrors (see chapter 2). Another source of motion is thermal noise driving the internal mechanical modes of the mirror substrate.

As discussed in section 1.4, the thermal noise contribution to the frequency band of interest can be reduced by putting the resonant frequency out of the measurement band and by using a system with a high Q. In a LIGO test mass, the Q should be limited by the material properties of the mirror substrate. (In practice, this is a difficult goal since the Q of the material can be degraded by clamps or other devices such as positioning magnets that are attached to the mirror). Ideally, this substrate should be a material with a very high Q. In LIGO, however, the mirror substrates must have optical properties that include transparency to green light ($5145\ \dot{A}$) and low absorption losses. The substrate must also be made from a material that can be polished to within very high tolerances. At this point, fused quartz (SiO_2) is the best material that satisfies these conditions. In the future, other materials with better Q's and optical properties might be used.

The first design consideration for the mirror is that the mirror should be substantially bigger than the beam spot. (The radius of the mirror must be more than four times bigger than the beam spot for a diffraction loss of 10^{-6}.) Another important consideration is the effect of the beam heating the mirror. Finally, given these constraints, the resonant frequencies of the mirror normal modes should be as high as possible. This sets a constraint on the aspect ratio of the mirror. If the mirror is too thin, it becomes a plate and the resonant frequencies are too low. If it is too thick, the mirror becomes a cylinder whose bending modes are too low in frequency. The good compromise is a mirror with a diameter of 25 cm and a thickness of 10 cm.

The lowest resonant frequencies of this mirror are on the order of 10 kHz. Since the gravitational wave band is near 100 Hz, the thermal noise from the internal modes of the mirror is given by

$$x^2(\omega) = \frac{4k_BT}{m\omega}\sum_n \frac{\phi_n(\omega)}{\omega_n^2} \tag{3.1.1}$$

For a certain aspect ratio, the quantity $\omega_n a/c$ where a is the radius of the mirror and c is the speed of sound is constant for a particular normal mode of the mirror. Since $M \propto a^3$, then $w_n^2 \propto M^{-2/3}$. The thermal noise then scales as $M^{-1/6}$. Changing the mass of the mirror does not significantly change the off-resonance thermal noise in the gravity wave detection band.

The other important part of equation 3.1.1 is the frequency dependence of the loss mechanism $\phi(\omega)$. Figures 1.2.1 and 1.2.2 clearly show that a structure damping loss mechanism will make the off-resonance thermal noise a serious problem near 100 Hz. The next few chapters describe an experiment that was undertaken to measure the frequency dependence of the loss mechanism in fused quartz.

3.2 Motivation for a Thin Plate Geometry

An important consideration for an experiment to measure the off-resonance thermal noise spectrum is the design of the mechanical system studied. The material is fused quartz since it is the most likely one used in the gravity wave detector test mass. The mass is made as small as possible in order to make the thermal noise as large as possible. The resonant frequency is on the order of 10 kHz so that seismic and acoustic noise are no longer significant noise terms. The normal mode that is measured is anti-symmetric in its shape so that common mode noise terms in the sensing system are cancelled by an interferometric measurement technique.

A geometry that takes all these considerations into account is a thin plate. While a thin plate does not have the same aspect ratio as a gravity wave detector test mass, the loss mechanisms in the plate should be due to the inherent material properties of the fused quartz and should give a good indication of the loss mechanisms in any other fused quartz mechanical system.

3.3 Normal Mode Analysis of a Thin Plate

For a thin circular plate, the general form of the normal modes is (see for example Blevins [24]):

$$z_{nk}(r,\theta) = A_{nk}\left[J_k\left(\frac{\lambda_{nk}r}{r_0}\right) + b_{nk}\, I_k\left(\frac{\lambda_{nk}r}{r_0}\right)\right] \cos(k\theta) \qquad (3.3.1)$$

where A_{nk} is the amplitude of the displacement for a particular mode, r_0 is the radius of the plate, λ_{nk} is an eigenvalue that depends upon the boundary conditions, k is the number of radial nodes and n is the number of circular nodes. J_k are Bessel functions of the first kind and I_k are modified Bessel functions of the first kind. The thin plate approximation is valid when the thickness, h, is much smaller than the radius $(h/r_0 << 1)$ and the displacements are much smaller than the thickness $(A_{nk}/h << 1)$. The coordinate system has its origin on the neutral surface of the plate and the z axis is normal to the neutral surface. z_{nk} is the vertical displacement of a point on the neutral surface (see figure 3.3.1). The components of displacement in the xy plane are second order relative to z_{nk} and are set equal to 0.

Figure 3.3.1 Sketch of the coordinate system for a thin, circular plate

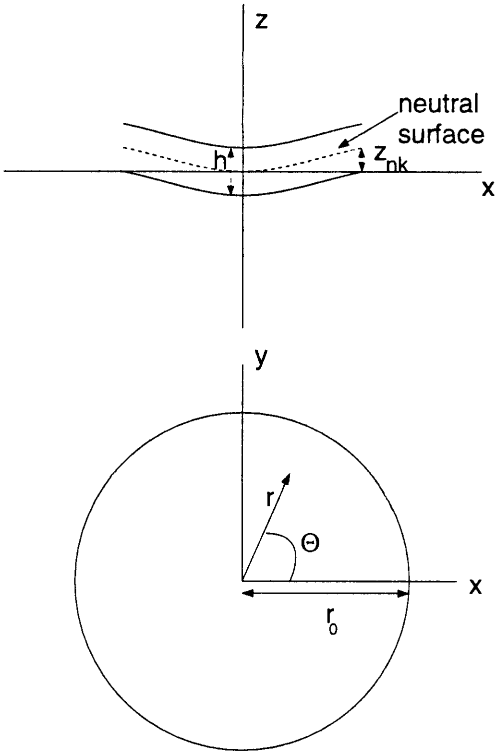

The boundary conditions for a rigidly clamped edge are:

$$\begin{aligned} Z_{nk}(r = r_o) &= 0 \\ \frac{\partial Z_{nk}}{\partial r}\Big|_{r=r_o} &= 0 \end{aligned} \tag{3.3.2}$$

Solving these equations give the following:

$$\begin{aligned} J_k(\lambda_{nk})\, I_{k+1}(\lambda_{nk}) + I_k(\lambda_{nk})\, J_{k+1}(\lambda_{nk}) &= 0 \\ b_{nk} &= \frac{-J_k(\lambda_{nk})}{I_k(\lambda_{nk})} \end{aligned} \tag{3.3.3}$$

The roots of these equations for some values of *k* and *n* are given in table 3.3.3.

Table 3.3.3 λ_{nk} and b_{nk} for clamped edge

n	k=0	k=1	k=2	k=3
0	3.19622 0.0557128	4.6109 0.0152162	5.90568 0.00523458	7.14353 0.00201321
1	6.30644 -0.0023015	7.79927 -0.000608146	9.19688 -0.0017531	10.5367 -0.0000565
2	9.4395 0.00110987	10.9581 0.0000254845	12.4022 0.0000675364	λ_{23} b_{23}

The shape of the second lowest mode is displayed in figure 3.3.2. This is the mode that is measured.

Figure 3.3.2 Second lowest order mode (*n=0, k=1*)

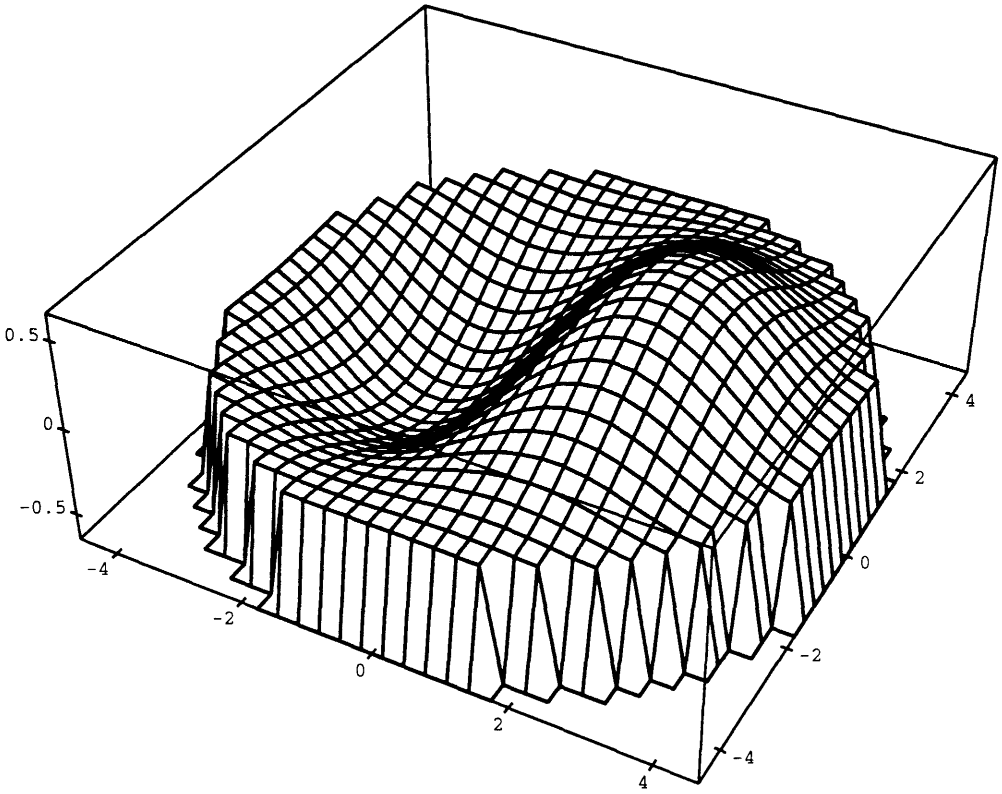

The frequencies of these modes are given by the solutions to the equation (see for example Landau [18])

$$\rho \frac{\partial^2 z_{nk}}{\partial t^2} + \frac{Eh^2}{12(1-\sigma^2)} \Delta^2 z_{nk} = 0 \tag{3.3.4}$$

where Δ is the two dimensional Laplacian ($\Delta = \frac{\partial^2}{\partial x^2} + \frac{\partial^2}{\partial y^2}$ in rectangular coordinates and $\Delta = \frac{1}{r}\frac{\partial}{\partial r}(r\frac{\partial}{\partial r}) + \frac{1}{r^2}\frac{\partial^2}{\partial \theta^2}$ in spherical coordinates). The frequencies are

$$\begin{gathered}
\omega_{nk}^2 = \frac{Eh^2}{12(1-\sigma^2)\rho} \frac{(\lambda_{nk})^4}{r_o^4} \\
E = 7.2 \times 10^{11} \; dynes/cm^2 \\
\sigma = 0.16 \\
\rho = 2.2 \, g/cm^3 \\
f_{nk} = 2.66 \times 10^4 \frac{(\lambda_{nk})^2 \, h}{r_o^2} \; Hz \quad r, h \; in \; cm \\
f \propto \frac{h}{r_0^2}
\end{gathered} \tag{3.3.5}$$

For the second lowest order mode, the frequency is:

$$f_{01} = 5.66 \times 10^5 \frac{h}{r_o^2} Hz \quad r, h \; in \; cm \tag{3.3.6}$$

3.4 Displacement Thermal Noise in a Plate Normal Mode

The next step is to calculate the actual displacement thermal noise of the plate as a function of position on the plate. In order to use the formalism of Callen, the impedance of the plate must be calculated.

The normal modes of the plate must be normalized according to the relation (Saulson [11] does a similar derivation for a one dimensional system)

$$\begin{gathered} \int_0^{r_0} \int_0^{2\pi} \rho(r,\theta) h \frac{1}{a_{nk}} z_{nk} \frac{1}{a_{n'k'}} z_{n'k'} r dr d\theta = \delta_{nkn'k'} \\ a_{nk}^2 = h\pi\rho r_0^2 M_{nk} \\ M_{nk} = \frac{1}{\lambda_{nk}^2} \int_0^{\lambda_{nk}} [J_k(u) + b_{nk} I_k(u)]^2 u du \end{gathered} \tag{3.4.1}$$

The plate is assumed to be uniform in density for these calculations. Table 3.4.4 gives some values for M_{nk}

Table 3.4.4 $M_{nk} = \frac{1}{\lambda_{nk}^2} \int_0^{\lambda_{nk}} (J_k(u) + b_{nk} I_k(u))^2 u \, du$

n	k=0	k=1	k=2	k=3
0	0.10887	0.067164	0.0498746	0.0394756
1	0.0506907	0.0404892	0.0336565	0.0287584
2	0.211237	0.0289387	0.124823	

The normal mode expansion of a displacement at a certain point on the plate is

$$z(r,\theta,t) = \sum_{n,k} \frac{1}{a_{nk}} z_{nk}(r,\theta) q_{nk}(t) \tag{3.4.2}$$

where $q_{nk}(t)$ is the generalized coordinate of mode nk. The equation of motion has the form

$$\begin{gathered} \ddot{q}_{nk}(t) + \omega_{nk}^2 (1 + \phi_{nk}(\omega)) q_{nk}(t) = Q_{nk}(t) \\ \left[-\omega^2 + \omega_{nk}^2 (1 + \phi_{nk}(\omega))\right] q_{nk}(t) = Q_{nk}(t) \end{gathered} \tag{3.4.3}$$

Since the Young's modulus has a loss term of the form

$$E(1 + i\phi(\omega)) \tag{3.4.4}$$

and the resonant frequency

$$\omega_{nk}^2 \propto E(1 + i\phi(\omega)) \tag{3.4.5}$$

an explicit damping term in the form of an internal friction, $\phi(\omega)$, is included in equation 3.4.3.

$$Q_{nk}(t) \tag{3.4.6}$$

is the generalized force that is given by

$$Q_{nk}(t) = \int_0^{r_0}\int_0^{2\pi} f(r,\theta,t)\frac{1}{a_{nk}} z_{nk}(r,\theta) r dr d\theta \tag{3.4.7}$$

where $f(r,\theta,t)$ is the force density that is applied to the system. If a force $Fe^{i\omega t}$ is applied at r, θ, the generalized force is

$$Q_{nk}(t) = Fe^{i\omega t}\frac{1}{a_{nk}} z_{nk}(r,\theta) \tag{3.4.8}$$

Putting this force in equation 3.4.3 gives

$$q_{nk}(t) = \frac{Fe^{i\omega t}\frac{1}{a_{nk}} z_{nk}}{\omega_{nk}^2 - \omega^2 + i\phi_{nk}(\omega)\omega_{nk}^2} \tag{3.4.9}$$

Substituting this result into equation 3.4.2 gives

$$z(r,\theta,t) = \sum_{n,k} \frac{Fe^{i\omega t}\frac{1}{a_{nk}^2} z_{nk}^2}{\omega_{nk}^2 - \omega^2 + i\phi_{nk}(\omega)\omega_{nk}^2} \tag{3.4.10}$$

The admittance $Y = velocity/F$ is

$$\begin{aligned} Y &= \sum_{n,k} \frac{i\omega\frac{1}{a_{nk}^2} z_{nk}^2}{\omega_{nk}^2 - \omega^2 + i\phi_{nk}(\omega)\omega_{nk}^2} \\ \sigma(\omega) = Re(Y) &= \sum_{n,k} \frac{\phi_{nk}(\omega)\omega\omega_{nk}^2\frac{1}{a_{nk}^2} z_{nk}^2}{\left(\omega_{nk}^2 - \omega^2\right)^2 + \phi_{nk}^2(\omega)\omega_{nk}^4} \end{aligned} \tag{3.4.11}$$

The thermal noise can be found by using equation 1.4.9

$$\begin{aligned} z_{thermal}^2(r,\theta,\omega) &= 4k_BT\sum_{n,k} \frac{\phi_{nk}(\omega)\omega_{nk}^2\frac{1}{a_{nk}^2} z_{nk}^2}{\omega\left(\left(\omega_{nk}^2 - \omega^2\right)^2 + \phi_{nk}^2(\omega)\omega_{nk}^4\right)} \\ &= \frac{4k_BT}{\pi\rho h r_0^2\omega}\sum_{n,k} \frac{\left[J_k\left(\frac{\lambda_{nk}}{r_0}r\right) + b_{nk}I_k\left(\frac{\lambda_{nk}}{r_0}r\right)\right]^2 \cos^2(k\theta)}{M_{nk}} \\ &\times \frac{\phi_{nk}(\omega)\omega_{nk}^2}{\left(\omega_{nk}^2 - \omega^2\right)^2 + \phi_{nk}^2(\omega)\omega_{nk}^4} \end{aligned} \tag{3.4.12}$$

The thermal noise contribution of a specific mode is

$$\begin{aligned} z_{nk}^2(r,\theta,f) &= \frac{4k_BT}{\pi\rho h r_0^2\omega}\frac{\left[J_k\left(\frac{\lambda_{nk}}{r_0}r\right)+b_{nk}I_k\left(\frac{\lambda_{nk}}{r_0}r\right)\right]^2\cos^2(k\theta)}{M_{nk}} \\ &\times\frac{\phi_{nk}(\omega)\omega_{nk}^2}{\left(\omega_{nk}^2-\omega^2\right)^2+\phi_{nk}^2(\omega)\omega_{nk}^4} \\ &= \frac{3.8\times10^{-15}}{hf}\frac{\left[J_k\left(\frac{\lambda_{nk}}{r_0}r\right)+b_{nk}I_k\left(\frac{\lambda_{nk}}{r_0}r\right)\right]^2\cos^2(k\theta)}{M_{nk}} \\ &\times\frac{\phi_{nk}(\omega)}{\left(1.7\times10^5\frac{h\lambda_{nk}^2}{r_0^2}-2.4\times10^{-4}\frac{r_0^2f^2}{h\lambda_{nk}^2}\right)^2+2.8\times10^{10}\phi_{nk}^2(\omega)\frac{h^2\lambda_{nk}^4}{r_0^4}} \\ &in\ cm/\sqrt{Hz}\ for\ r_0,\ r,\ h\ in\ cm,\ f\ in\ Hz \end{aligned} \tag{3.4.13}$$

3.5 Mirror Parameters

As discussed in section 3.2, the parameters that determine the size of the mirror for this experiment are chosen to give a resonant frequency near 10 kHz for the $n = 0$, $k = 1$ mode. There are two ways to achieve a resonant frequency in this range and each has a problem associated with it. The mirror can be made thin which causes problems in the manufacturing process since a certain aspect ratio is necessary in order to obtain a good surface figure. The surface figure is constrained by two different factors. The mirror will be optically contacted which requires a minimum surface figure error. Also, the high finesse of the optical cavities demands a very small loss in the mirror which constrains the surface figure. The other dimension that can be changed is the diameter. Practical considerations limit this size.

Standard industry practice uses a 9:1 aspect ratio for a mirror to have a surface figure of $\lambda/10$. For a frequency of 10 kHz, the diameter of the mirror will be 10″. This is too large for table top sized experiment. A reasonable size for the diameter is about 4″. Since the surface figure is only important over the area that is optically contacted and over the beam spot (which are both small compared to the area of the entire plate), the aspect ratio and surface figure can be relaxed somewhat. The parameters used in this experiment are a diameter of 4″ (actually 4.75″ including the surface that is optically contacted) and a thickness of 1/4″. This has a resonance frequency of 14 kHz for the second lowest mode. If the predicted sensitivity of this experiment does reach the conservative calculated value of $10^{-17}\ cm/\sqrt{Hz}$, then the off resonance thermal noise should be seen.

One of the goals of this experiment is to determine the shape of the off resonance thermal noise curve. Figure 3.5.1 shows four different curves that describe:

$$\phi(\omega) = 10^{-5}, 10^{-6}, \frac{f\,10^{-5}}{(14\times10^3\ Hz)}, \frac{f\,10^{-6}}{(14\times10^3\ Hz)} \tag{3.5.1}$$

The first two expressions represent structure damping with $Q = 10^5$, 10^6 and the last two expressions represent a viscous damping with $Q = 10^5$, 10^6 at 14 kHz. The spot on the mirror is chosen to be at the maximum displacement point or at $r = 0.38r_o$ for the $n = 0$, $k = 1$ mode. It is clear that there are substantial differences between the two damping models at frequencies above and below the resonance. An instrument sensitivity of $10^{-17} cm/\sqrt{Hz}$ is sufficient to distinguish between the two damping models for a Q of 10^5.

Figure 3.5.1 Plot of the thermal noise from the second lowest mode. The top curve is $\phi(\omega) = 10^{-5}$; the next is $\phi(\omega) = \frac{f\,10^{-5}}{(14\times10^3\,Hz)}$, then $\phi(\omega) = 10^{-6}$; the bottom curve is $\phi(\omega) = \frac{f\,10^{-6}}{(14\times10^3\,Hz)}$. The horizontal line represents a predicted sensitivity of $10^{-17} cm/\sqrt{Hz}$.

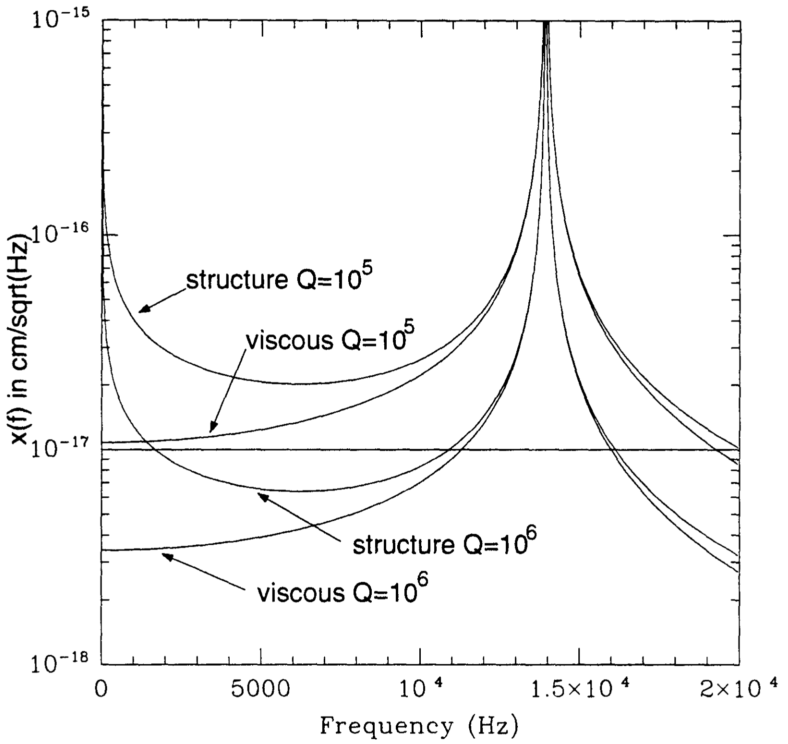

3.6 Mechanical Assembly to Hold the Thin Plate

The thin plate must be mounted in a way that neither degrades its Q nor adds any other significant losses. A first guess at the best clamp is an optically contacted joint. A good optical contact joint should be the same as if the material is continuous across the joint and hence, have the same losses as the material. The other part of the clamp that must be considered is how it can form an optical interferometer. The final design that was used can be seen in figure 3.6.1.

By making the two spherical mirrors and the fused quartz plate on which they are mounted thick, the resonant frequencies and mass will be high so that their contribution to the thermal noise of the system will be negligible. The normal modes of the cylindrical shell should primarily be common mode in nature. By making the walls sufficiently thick, the frequencies of these modes are also high so that their contribution to the thermal noise is negligible. Since this optical assembly is the most important single part of the experiment and cannot be changed easily, it is referred to as the "jewel". It also happens to be the most expensive part of the experiment.

Figure 3.6.1 Sketch of experimental optical assembly or jewel. The flat, thin mirror on the left is the one that will be measured. The two small spherical mirrors are optically contacted to a flat piece of fused quartz. Both the thin, flat mirror and the thick plate of fused quartz are optically contacted to a fused quartz cylinder that holds the assembly together.

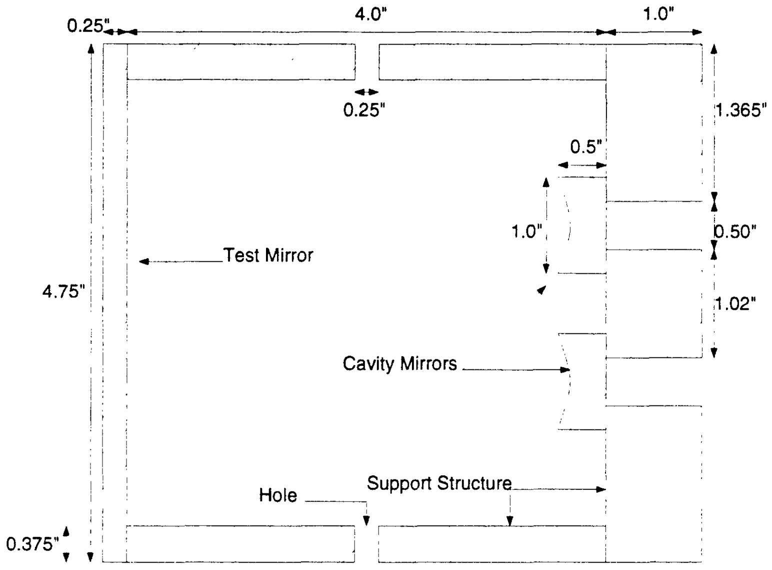

The two spherical mirrors and the plate upon which they are attached do contribute to the thermal noise being measured, but not significantly. A spherical mirror 1″ in diameter and 1/2″ thick has its lowest order mode at 214 kHz. Each spherical mirror contributes uncorrelated noise from this mode. Since the plate is much thicker than the thin mirror, it has a much higher resonant frequency (56 kHz for a thickness of 1″ and diameter of 4″) for the mode that will contribute to the thermal noise. Figure 3.6.2 shows a plot of the thermal noise contribution from different parts of the jewel.

Figure 3.6.2 Plot of thermal noise from different parts of the optical system. The bottom curve is the contribution from a spherical mirror. The next one up is the contribution from the thick plate. The horizontal line represents the predicted sensitivity of $10^{-17}\ cm/\sqrt{Hz}$. Finally, the top curve is the signal that will be measured. In all cases, $\phi(\omega) = 10^{-5}$.

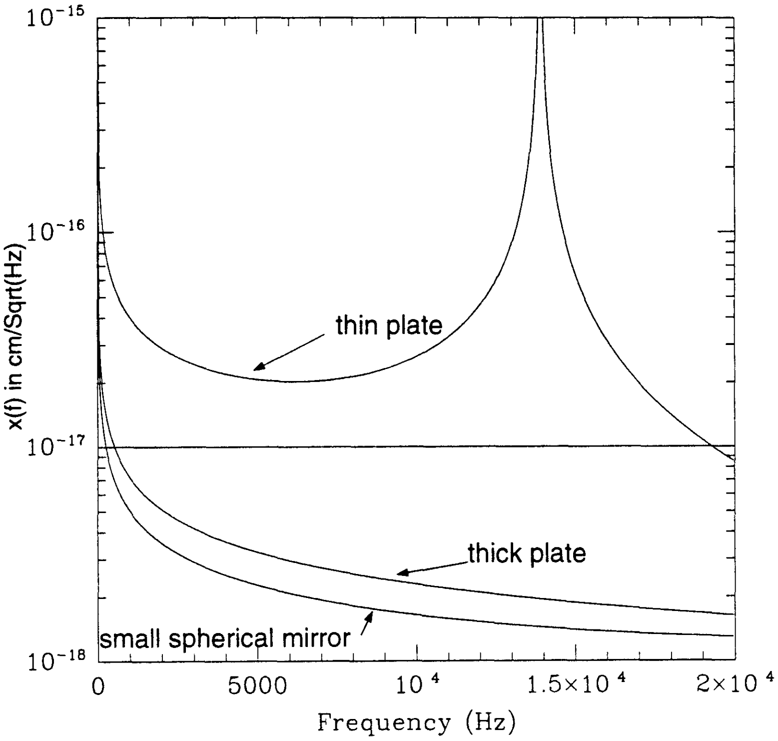

The resonant frequencies of a thin, cylindrical shell are (see for example Leissa [25])

$$\begin{gathered}\omega^2 = \frac{E}{\rho R(1-\sigma^2)}\Omega^2 \\ f = 18kHz \times \Omega\end{gathered} \tag{3.6.1}$$

where R is the inner radius of the shell. Ω is a solution to the equation

$$\begin{gathered}\Omega^6 - (K_2 + k\Delta K_2)\Omega^4 + (K_1 + k\Delta K_1)\Omega^2 - (K_0 + k\Delta K_0) = 0 \\ K_2 = 1 + \frac{1}{2}(3-\sigma)(n^2+\lambda^2) + k(n^2+\lambda^2)^2 \\ K_1 = \frac{1}{2}(1-\sigma)\left[n^2 + (3+2\sigma)\lambda^2 + (n^2+\lambda^2)^2 + \frac{3-\sigma}{1-\sigma}k(n^2+\lambda^2)^3\right] \\ K_0 = \frac{1}{2}(1-\sigma)\left[(1-\sigma^2)\lambda^4 + k(n^2+\lambda^2)^4\right] \\ k = \frac{h^2}{12R^2} \\ \lambda = \frac{m\pi k}{L}\end{gathered} \tag{3.6.2}$$

where h is the thickness of the shell and L its length. The integers m and n refer to the number of axial and circumferential nodes respectively (see figure 3.6.3).

Figure 3.6.3 Sketch of a normal mode for n=2, m=3.

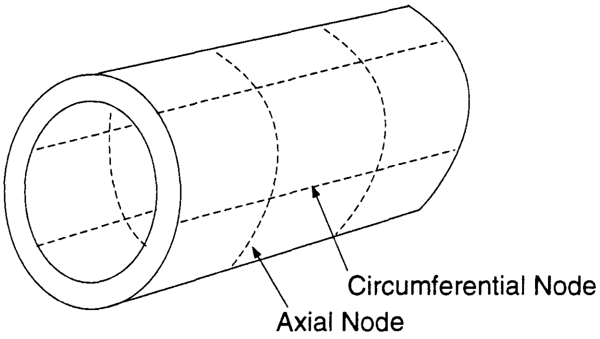

The first approximation in this model assumes the ΔK terms are very small since k is small for a cylinder with a thin shell. There are three solutions to equation 3.6.2 for a given n, m which are associated with radial, longitudinal and circumferential modes. The lowest frequency for a given n, m is usually associated with a radial mode.

Table 3.6.5 The solutions to equation 3.6.2 for a cylinder with h=0.375″, L=4″ and R=2″.

m	1	2	3	4
n				
0	0.988	1.12	1.55	2.35
	1.02	2.04	3.05	4.07
	1.58	3.15	4.72	6.29
1	0.648	1.05	1.56	2.39
	1.37	2.18	3.14	4.13
	1.92	3.31	4.82	6.37
2	0.463	0.988	1.62	2.50
	1.76	2.50	3.36	4.30
	2.65	3.75	5.13	6.60
3	0.619	1.10	1.79	2.71
	2.26	2.90	3.68	4.56
	3.49	4.38	5.60	6.97
4	0.973	1.41	2.10	3.04
	2.82	3.37	4.07	4.89
	4.39	5.14	6.21	7.46

The lowest order mode that contributes an effective length change that mimics a differential mode motion of the plate is a $n = 1$, $m = 1$ mode that looks like that shown in figure 3.6.4.

Figure 3.6.4 Sketch of a cylinder normal mode that produces a differential path length between the two cavities.

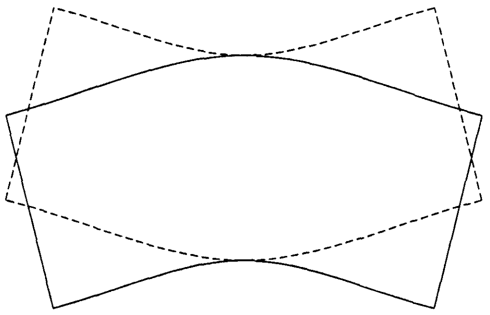

Unfortunately, the resonant frequency of this mode is about 12 kHz. However, since the mass of the entire jewel is about ten times that of the thin plate alone, the amplitude of the thermal noise from one of these modes is a factor $\sqrt{10}$ smaller than the thermal noise of the thin plate alone. Also, the motion of the cylinder ends is common mode to some extent (one of the cavity length moves more than the other, but they both move) (see figure 3.6.5). This also reduces the effective motion of this mode by a factor

$$\begin{aligned} \Delta x &= \Delta x_2 - \Delta x_1 \\ &= \frac{\Delta x_0}{2r_0}(r_0 + 0.38r_0 - (r_0 - 0.38r_0)) \\ &= 0.38\Delta x_0 \end{aligned} \tag{3.6.3}$$

Figure 3.6.5

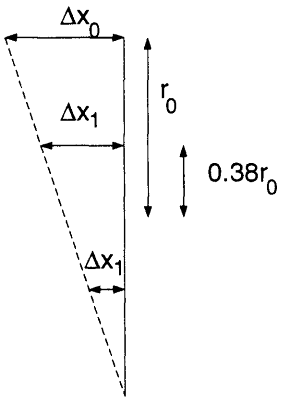

The off resonance thermal noise from this mode is on the order

$$\begin{aligned} x(\omega) &\approx 0.38\sqrt{\frac{4k_BT\phi}{m\omega\omega_0^2}} \\ &\approx 0.38\sqrt{\frac{4k_BT10^{-5}}{1500g \times (12kHz)^2 \times (2\pi)^3 f}} \\ &\approx 6.7 \times 10^{-17} f^{-\frac{1}{2}} cm/\sqrt{HZ} \end{aligned} \tag{3.6.4}$$

At 5 kHz, the off-resonance thermal noise from this mode of the cylinder will be $1 \times 10^{-18} cm/\sqrt{Hz}$. This is well below the off-resonance thermal noise from the plate which is approximately $2 \times 10^{-17} cm/\sqrt{Hz}$ at 5 kHz. Although the thermal noise at the resonant frequency of the cylinder can be seen, the mode has a high Q and simply sticks out above the off-resonance thermal noise from the thin plate. The motion of the plate should be the dominant motion detected.

Chapter 4 Experimental Optical Design

4.1 Introduction to the Experiment

The experimental goal is to measure the off-resonance thermal noise spectrum from a normal mode of a bulk piece of fused quartz. The numbers calculated in chapter 3 show that an experimental sensitivity of at least $10^{-17} cm/\sqrt{Hz}$ is necessary. Since this is the same sensitivity that should be achieved by the initial LIGO interferometer, this experiment uses many of the same techniques that a gravity detector does in order to obtain such a high sensitivity.

There are many different noise sources that must be considered when designing an interferometer. Two important noise sources are amplitude noise and frequency noise. The amplitude noise of lasers is quite large between 1 kHz and 20 kHz due to $1/f$ noise. This problem is avoided by performing the fringe interrogation at a sufficiently high frequency where the laser amplitude noise is dominated by shot noise (see section 4.6). The frequency noise from the laser is a common mode noise source that is cancelled by the interferometry. By using a laser that has an inherent frequency stability and carefully controlling the common mode rejection in the interferometer beam recombination, the frequency noise can be eliminated as a significant noise source (see section 4.8).

A simple calculation for the shot noise limited sensitivity of a Michelson interferometer with a perfect contrast gives

$$\begin{aligned}\Delta x(f) &= \frac{1}{\pi b}\sqrt{\frac{\eta h \lambda c}{2I}} \\ &= \frac{1}{b} \times 10^{-13} cm/\sqrt{Hz} \\ &\times \sqrt{\frac{\eta}{0.5} \times \frac{\lambda}{1.06\mu m} \times \frac{I}{40mW}}\end{aligned} \tag{4.1.1}$$

where b is the number of bounces the light beam makes against a mirror. The number of bounces must be greater than 10000 in order to achieve a sensitivity of $10^{-17} cm/\sqrt{Hz}$. This can be accomplished by making the interferometer arms resonant Fabry-Perot cavities where the equivalent number of bounces for mirrors with transmission T and loss L is

$$b = \frac{1}{L+T} \tag{4.1.2}$$

Current mirror technologies can achieve losses as low as a few parts per million. If the transmission of the mirrors is set equal to the loss to maximize the light throughput, the equivalent number of bounces can easily reach 100000 (see section 4.7 for an exact calculation of the instrument sensitivity).

4.2 Optical Layout

The optical system is a Mach-Zender interferometer with Fabry-Perot cavities in the phase sensitive optical paths (see figures 4.2.2 and 4.2.3). The finesse of the cavities is high to increase the phase changes due the motion of the cavity ends. The thermal noise that will be measured comes from the mechanical mode of a thin, common test mirror that produces an anti-symmetric length change between the two cavities (see figure 4.2.1).

Figure 4.2.1 Motion of mirror and Fabry-Perot cavities inside the jewel.

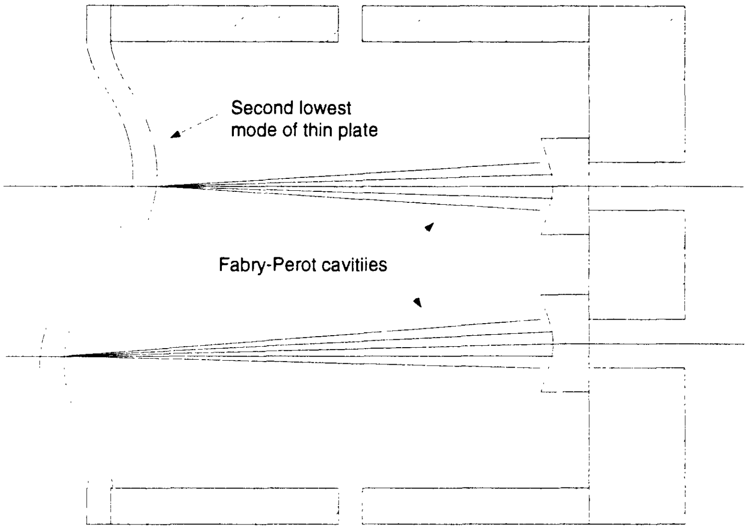

The optics contain all the necessary components to keep two Fabry-Perot cavities on resonance, modulate their output and recombine the beams (see figures 4.2.2 and 4.2.3). The laser is a Lightwave Model 120–03A MISER. A diode laser pumps a non-planar Nd:YAG crystal to produce 40 mW of 1.06 μm light.

The foreoptics has a Faraday isolator to keep reflections from reentering the laser, a lens and $\lambda/2$ plate that direct the light onto a GRIN lens. The GRIN lens focuses the light into a polarization preserving single mode optical fibre. This fibre serves two purposes. It allows the light to enter the vacuum system and also takes the elliptical light from the MISER and converts it into the fibre's HE_{11} mode which is nearly the same as a TEM_{00} gaussian beam mode.

The experiment is done in a vacuum to reduce acoustic noise and index of refraction phase fluctuations. A pressure of 10^{-5} mbar was routinely achieved which set the equivalent displacement noise due to index of refraction phase fluctuations at $8 \times 10^{-20} cm/\sqrt{Hz}$. The 24″ vacuum chamber sits on a 4000 kg granite optical table that is supported by pneumatic legs that give the table a resonant frequency of 1 Hz to vertical harmonic motion and to rocking motions. Since the experiment is designed to provide data at frequencies above 1 kHz, this provides the necessary seismic isolation.

The light coming out of the fibre is collimated with a GRIN lens and then mode matched to the cavity with another lens. The beam goes through a Pockels cell that impresses a phase modulation on the light. The beam is then split by a Köster prism

Figure 4.2.2 Optical Layout

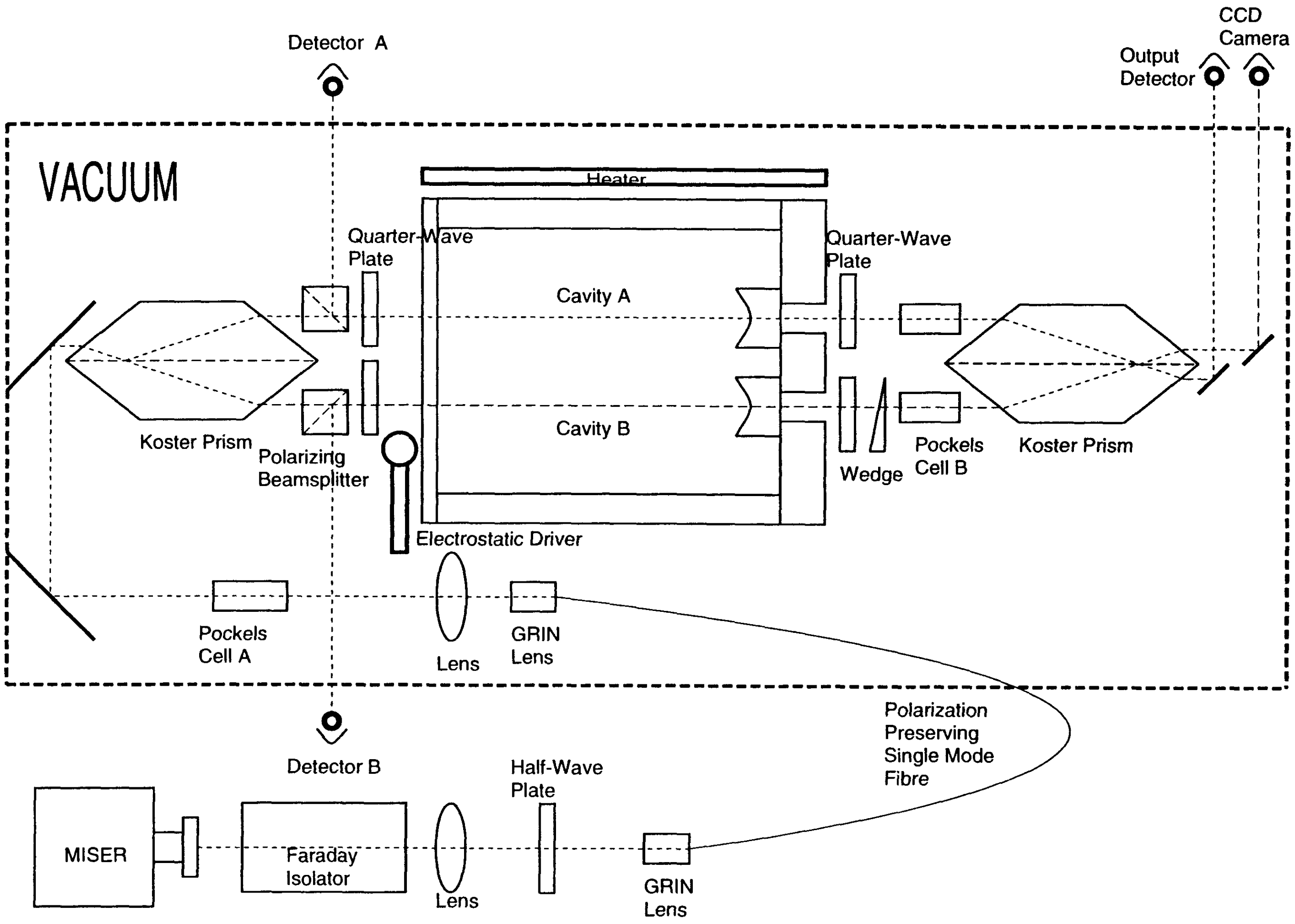

Figure 4.2.3 Signal Extraction and Control System Block Diagram

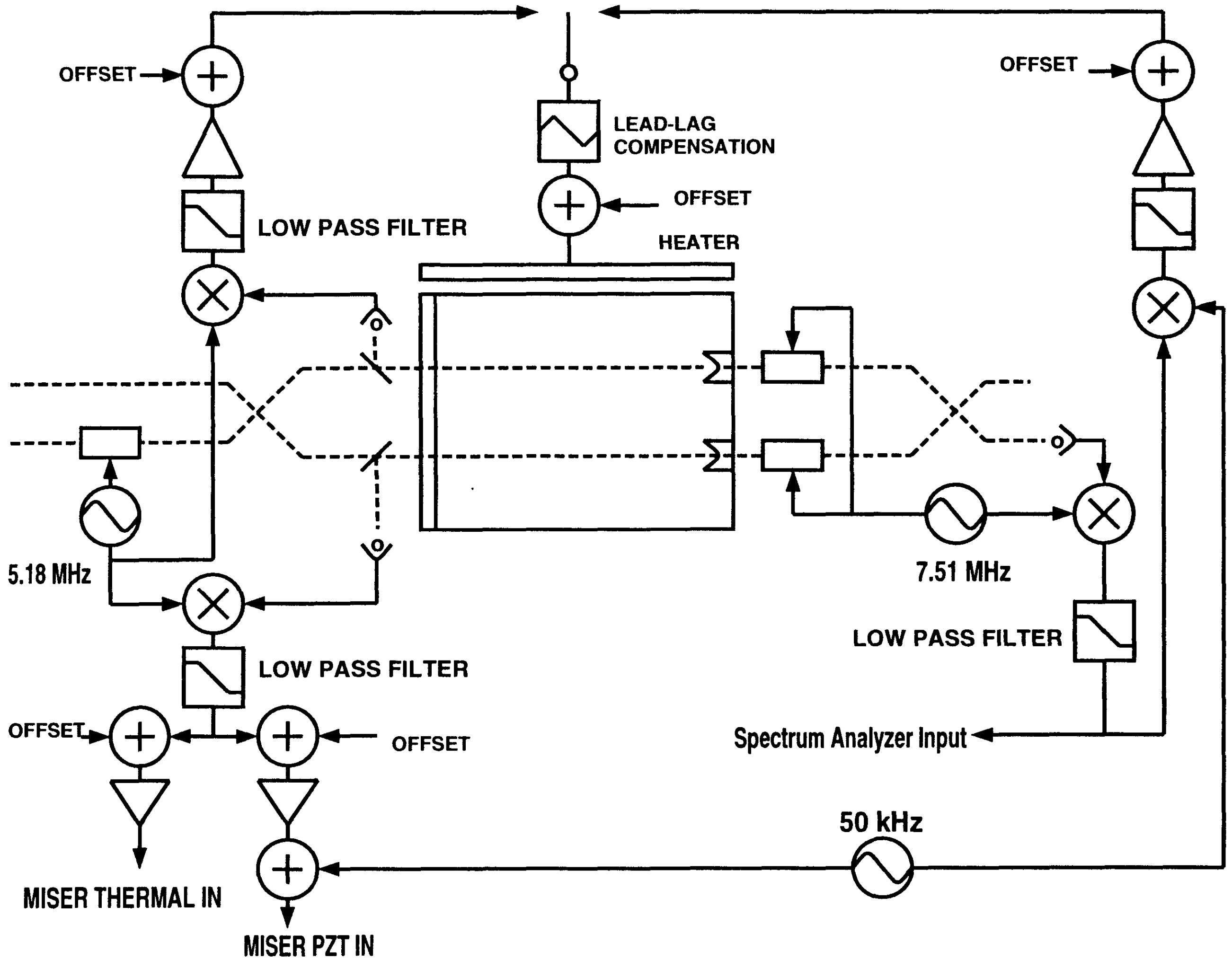

which is a beam splitter that takes a p-polarized light beam and splits it into two parallel beams that each have the same phase (see figure 4.2.4).

Figure 4.2.4 Köster prism.

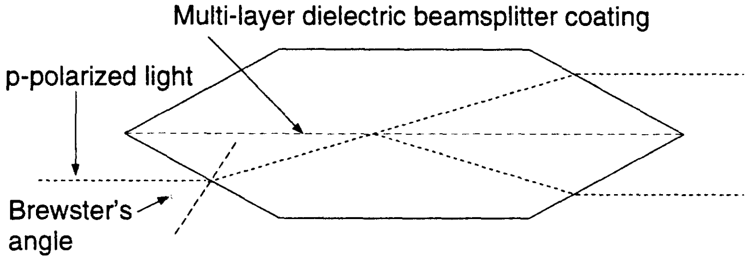

Each separate beam then goes through a polarizing beamsplitter and $\lambda/4$ plate. This produces a reflection lock signal (see section 4.3) for each cavity. The laser frequency is locked to one cavity. The other cavity is heated by a thin metallic strip until it also is in resonance (see sections 4.3 and 4.4 for cavity locking schemes). After leaving the cavity, the light is made linearly polarized again and modulated by another set of Pockels cells. Finally, the light is recombined by another Köster prism and then deflected by steering mirrors through a window out of the vacuum system and onto a RF photodetector.

4.3 Reflection Locking of MISER to One Cavity

There are three controls on the laser. The first is a power control on the pump diode that is usually left at the maximum position for best performance. The two other controls regulate the frequency of the laser. A heater on the Nd:Yag crystal acts as a coarse frequency control with a large dynamic range (about 45 GHz) and a control bandwidth of approximately 1 Hz that is limited by the thermal mass of the crystal.

A finer adjustment with a much higher control bandwidth comes from a PZT mounted on the crystal. Applying a voltage to the PZT squeezes the crystal and changes the effective path length taken by the light. By removing a varistor on the control circuit, one can apply a reasonably high voltage (in this case it never exceeded 100V, although higher voltages should not damage the PZT) to the PZT which gives this adjustment a dynamic range of a few hundred MHz (the calibration of this control was measured to be 4 MHz/V). The bandwidth of this control is limited by the lowest mechanical resonance of the PZT and Nd:YAG crystal system at 190 kHz.

The laser was frequency locked to one cavity by using the Pound-Drever reflection lock technique [26]. The light reflected from a cavity is extracted using a circulator (λ/4 plate and polarizing beamsplitter). The electric field of the phase modulated beam before reflection is (see appendix B)

$$\varepsilon(t) = \varepsilon_0 J_0(\Gamma) e^{i\omega t} - \varepsilon_0 J_1(\Gamma) e^{i(\omega+\omega_m)t} + \varepsilon_0 J_1(\Gamma) e^{i(\omega-\omega_m)t} \tag{4.3.1}$$

After reflection from the cavity, the electric field becomes (see appendix A for an explanation of Fabry-Perot cavity properties)

$$
\begin{aligned}
\frac{\varepsilon_{refl}(t)}{\varepsilon_{inc}(t)} &= J_0(\Gamma)A\left(\frac{2wl}{c}\right)e^{i\varphi\left(\frac{2wl}{c}\right)}e^{i\omega t} \\
&- J_1(\Gamma)A\left(\frac{2(\omega+\omega_m)l}{c}\right)e^{i\varphi\left(\frac{2(\omega+\omega_m)l}{c}\right)}e^{i(\omega+\omega_m)t} \\
&+ J_1(\Gamma)A\left(\frac{2(\omega-\omega_m)l}{c}\right)e^{i\varphi\left(\frac{2(\omega-\omega_m)l}{c}\right)}e^{i(\omega-\omega_m)t}
\end{aligned}
\tag{4.3.2}
$$

where $A(x)$ is the reflected amplitude. Since the cavities have a small bandwidth, the sidebands are rejected by the cavity when it is resonant with the carrier. This simplifies the above expression somewhat by making the following approximations

$$
\begin{aligned}
A\left(\frac{2(\omega+\omega_m)l}{c}\right) &= A\left(\frac{2(\omega-\omega_m)l}{c}\right) = 1 \\
\varphi\left(\frac{2(\omega+\omega_m)l}{c}\right) &= -\varphi\left(\frac{2(\omega-\omega_m)l}{c}\right) = \Delta
\end{aligned}
\tag{4.3.3}
$$

The intensity of the reflected field will be

$$
\begin{aligned}
\frac{I_{refl}}{Iinc} &= J_0(\Gamma)A^2\left(\frac{2\omega l}{c}\right) + 2J_1^2(\Gamma) \\
&- 4J_0(\Gamma)J_1(\Gamma)A\left(\frac{2\omega l}{c}\right)\sin\left(\varphi\left(\frac{2\omega l}{c}\right)\right)\sin\left(\omega_m t + \Delta\right) \\
&- 2J_1^2(\Gamma)\cos\left(2\omega_m t + 2\Delta\right)
\end{aligned}
\tag{4.3.4}
$$

One can then demodulate the intensity of the light by multiplying the signal by $\sin(\omega_m t + \phi)$ and low pass filter terms with a dependence on $2\omega_m$ and its higher order multiples. For small perturbations around the resonance condition, the amplitude and phase can be written

$$
\begin{aligned}
A &= \frac{(1-L-T)L}{L+T} \\
\varphi &= \frac{T}{L(L+T)}\left(\frac{2}{c}\right)\Delta(\omega l)
\end{aligned}
\tag{4.3.5}
$$

where L is the fraction of power lost upon reflection from a mirror and T is the fraction of power transmitted through a mirror. This gives an error signal that is proportional to a change in either the cavity length or frequency of the laser

$$
error\ signal = 4J_0(\Gamma)J_1(\Gamma)\frac{(1-L-T)T}{(L+T)^2}\frac{\Delta(\omega l)}{c}
\tag{4.3.6}
$$

The actual transfer function for the reflection lock servo loop has its lowest pole at 3.2 Hz from a low pass filter. There is also lead-lag compensation with a pole-zero pair at 23.4 kHz-459 kHz. This is necessary to overcome phase discontinuities that start to occur near 50 kHz. The unity gain point occurs at 2.0 kHz. The phase margin here is only a few degrees from 180 degrees. Figures 4.3.1 and 4.3.2 show the magnitude and phase of the closed loop transfer function for the reflection lock servo loop. The coherence is poor below 1 kHz, but the magnitude does have a $1/f$ slope. The phase plot shows that there is still some phase margin at 2 kHz.

Figure 4.3.1 The magnitude of the closed loop transfer function for the reflection lock servo loop.

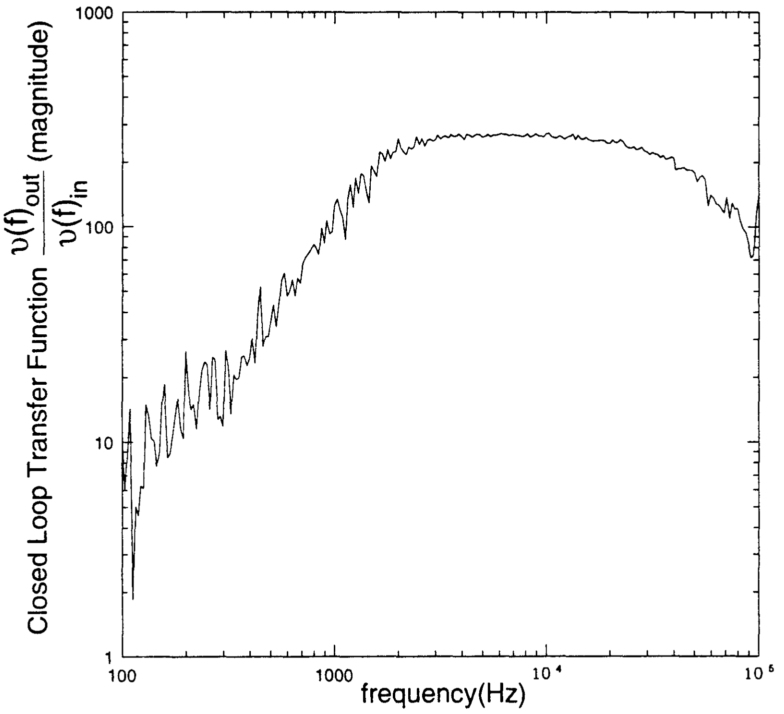

Figure 4.3.2 The phase of the closed loop transfer function for the reflection lock servo loop.

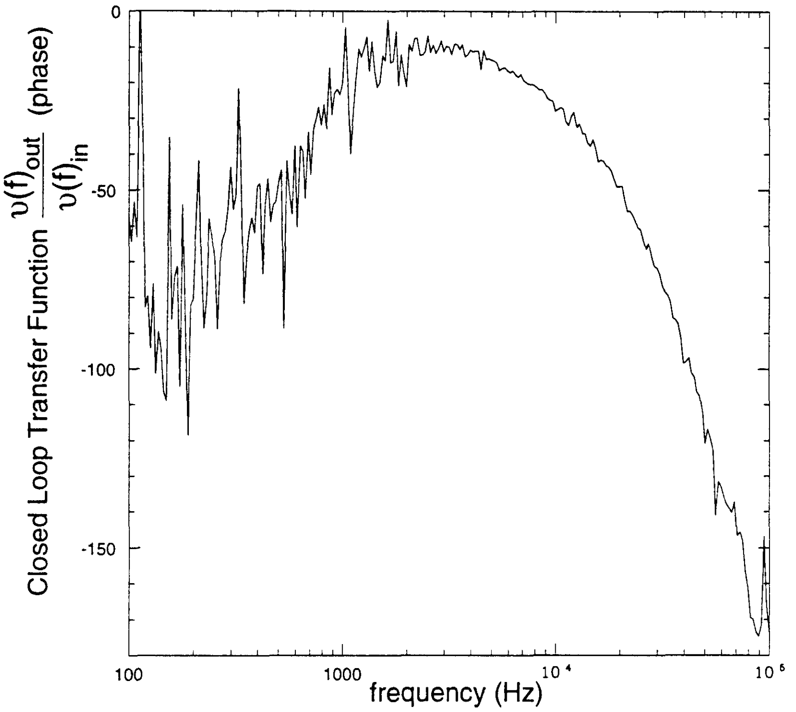

4.4 Thermal Tuning of One Cavity to Another

The difference in length between the two cavities is changed by differentially heating the quartz cylinder. Since the radiative cooling from the surface of the cylinder is larger than the heat flow due to conduction across the circumference of the cylinder, a temperature gradient between the heated side and unheated side occurs. Assume the length of one cavity is l_1 and the other l_2 where $l_2 > l_1$, and the frequency of the laser is locked to

$$l_2 = \frac{n\lambda}{2} \tag{4.4.1}$$

where n is an integer. If one wants to lock the other cavity on resonance, then its length must be changed by an amount δ such that

$$l_1 + \delta = \frac{n'\lambda}{2} \tag{4.4.2}$$

$$\delta < \frac{\lambda = 1.064\mu m}{4} \tag{4.4.3}$$

The differential heating of the cylinder can be approximated as a one dimensional problem. In thermal equilibrium and at steady state

$$[J(\theta) - J(\theta + d\theta)]h - \sigma\epsilon T_c^4(\theta)d\theta(R + (R - h)) + \sigma\epsilon T_r^4(\theta)d\theta(R + (R - h)) = 0 \tag{4.4.4}$$

which reduces to the differential equation

$$\frac{-dJ(\theta)}{d\theta}+\frac{\sigma\epsilon}{h}(2R-h)\big(T_r^4-T_c^4(\theta)\big)=0 \tag{4.4.5}$$

Using the Fourier heat conduction law

$$\begin{aligned} J &= -\kappa\frac{dT}{dl}=-\kappa\frac{dT}{Rd\theta} \\ \frac{dJ}{d\theta} &= \frac{-\kappa}{R}\frac{d^2T}{d\theta^2} \end{aligned} \tag{4.4.6}$$

gives the equation

$$\frac{d^2T_c(\theta)}{d\theta^2}+\frac{\sigma\epsilon R(2R-h)}{\kappa h}\big(T_r^4-T_c^4(\theta)\big)=0 \tag{4.4.7}$$

Since the temperature of the cylinder is not raised much higher than room temperature (otherwise various elements in the vacuum system could start to outgas and ruin the mirror coatings), one can linearize the above equation

Figure 4.4.1 One dimensional cylinder heating problem

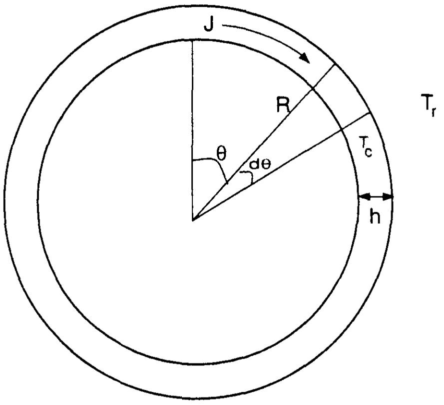

$$\begin{aligned} T_c &= T_r+\Delta T,\ \Delta T << T_r \\ T_r^4-T_c^4 &\approx -4T_r^3(T_c-T_r) \\ \frac{d^2T_c}{d\theta^2}-\frac{4\epsilon\sigma R(2R-h)T_r^3}{\kappa h}T_c &= \frac{4\epsilon\sigma R(2R-h)T_r^4}{\kappa h} \end{aligned} \tag{4.4.8}$$

The solution to this equation is

$$\begin{aligned} T(\theta) &= T(0)e^{-\left(\frac{4\epsilon\sigma R(2R-h)}{\kappa h}T_r^3\right)^{\frac{1}{2}}\theta}+T_r \\ &= T(0)e^{-\alpha\theta}+T_r \end{aligned} \tag{4.4.9}$$

Using typical values for fused quartz gives

$$\begin{aligned} T_r &= 300\ K \\ C_v &= 0.7\ Joules/g\,K \\ \kappa &= 0.01\ Watts/cm\,K \\ \epsilon(\lambda &= 16\mu m)\approx 1 \\ \alpha &= 2.1\ radians^{-1} \end{aligned} \tag{4.4.10}$$

The heat input comes from a thin ribbon of platinum that is placed very close to one side of the fused quartz cylinder. The angle

Figure 4.4.2 Heater element and fused quartz cylinder

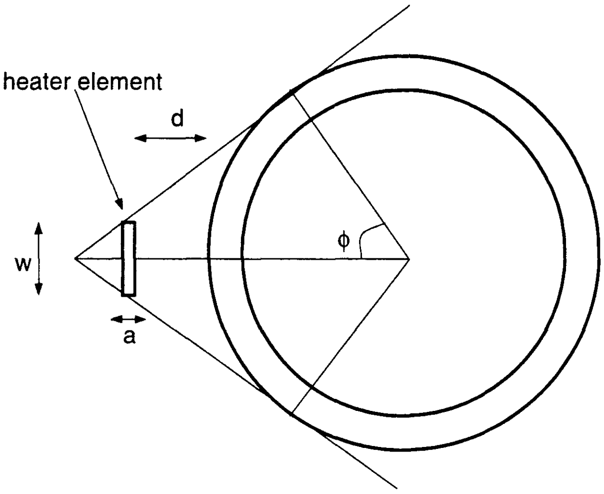

$$\begin{aligned} \cos\phi &= \frac{4R(d+R) - w\sqrt{w^2 + 4d(d+2R)}}{w^2 + 4(d+R)^2} \\ w &= 0.635\,cm \\ d &\approx 0.3\,cm \\ \phi &= 0.49\,radians \end{aligned} \tag{4.4.11}$$

determines how much radiated energy is subtended by the ribbon onto the cylinder. The

Figure 4.4.3 Platinum heater element

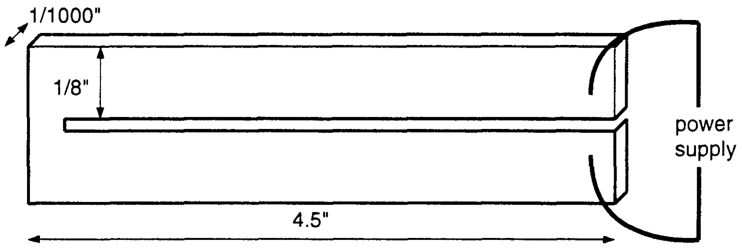

power going into the cylinder is

$$P_{in} = \epsilon_{rib}\sigma(l\,w)\left(\frac{2\phi}{2\pi}\right)\epsilon\left(T_{rib}^4 - T_r^4\right) \tag{4.4.12}$$

The power that is conducting away from the heated part to the unheated part of the cylinder is

$$\begin{aligned} P_{out} &= -2\kappa\frac{dT}{Rd\theta}h\,l \\ &= \frac{2\kappa\alpha l\,h}{R}T(0) \end{aligned} \tag{4.4.13}$$

and the final expression for the temperature of the cylinder as a function of angle is

$$\begin{aligned} T(\theta) &= T(0)\, e^{-\alpha\theta} + T_r \\ T(0) &= \frac{\epsilon_r \sigma w\, R\phi\epsilon}{2\kappa\alpha h\pi}(T_{rib}^4 - T_r^4) \\ \epsilon_r &\approx 0.5 \\ T(0) &= 4.3 \times 10^{-11}(T_{rib}^4 - T_r^4) \end{aligned} \tag{4.4.14}$$

If the maximum differential cavity length is $2.66 \times 10^{-5}\ cm$, then the temperature difference between the two parts of the cylinder will be

$$\Delta T = \frac{\Delta l}{l\alpha_{th}} = \frac{2.66 \times 10^{-5}}{8.89 \times 5 \times 10^{-7}} = 6.1K \tag{4.4.15}$$

where α_{TH} is the linear thermal expansion coefficient. Since

$$\Delta T = T(0)\left[e^{-\theta_1} - e^{-\theta_2}\right] \tag{4.4.16}$$

then the temperature of the ribbon must be $T_{rib} = 990K$

Figure 4.4.4 The angle between the two cavities $\theta_1 = 1.2rad$ and $\theta_2 = 1.9rad$

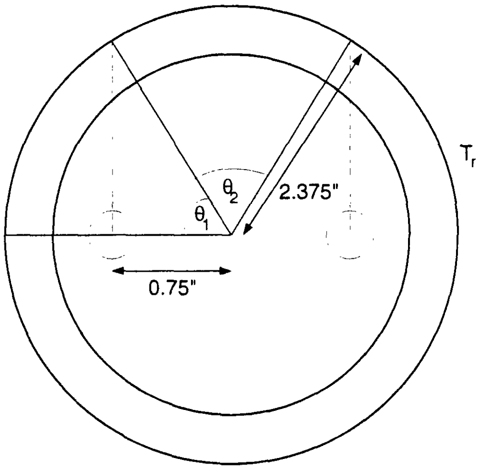

The power dissipated by the ribbon comes from its electrical resistance

$$\begin{aligned} P &= i^2 R = \sigma\varepsilon_{rib} w l(T_{rib}^4 - T_r^4) \\ R &= \frac{2l\rho}{a(\frac{w}{2})} = 0.57\ ohms \\ \rho(1200K) &= 2 \times 10^{-5} ohms\ cm \\ P &= 43\ watts \\ i &= 8.7\ amps \end{aligned} \tag{4.4.17}$$

By placing a reflective heat shield on one side of the heater (in this case, a piece of sheet aluminum), the amount of power from the heater that is directed towards the jewel is essentially doubled. This reduces the temperature of the heater by about $2^{1/4}$.

The thermal lock procedure starts by placing a DC offset on the voltage across the heater. This voltage is determined by increasing the voltage on the heater by small amounts and waiting for the temperature to equilibrate. By sweeping the frequency of the MISER, the difference in distance between the TEM_{00} modes of each cavity can be determined. When the heater reaches the right temperature, each cavity will lock in a TEM_{00} mode for the same frequency of the MISER. This is the operating point of the heater.

Figure 4.4.5 Plot of the difference in length between the two optical cavities vs. time while heating one side of cylinder with a thin ribbon element. The time constant for heating this thermal mass is 23.8 minutes.

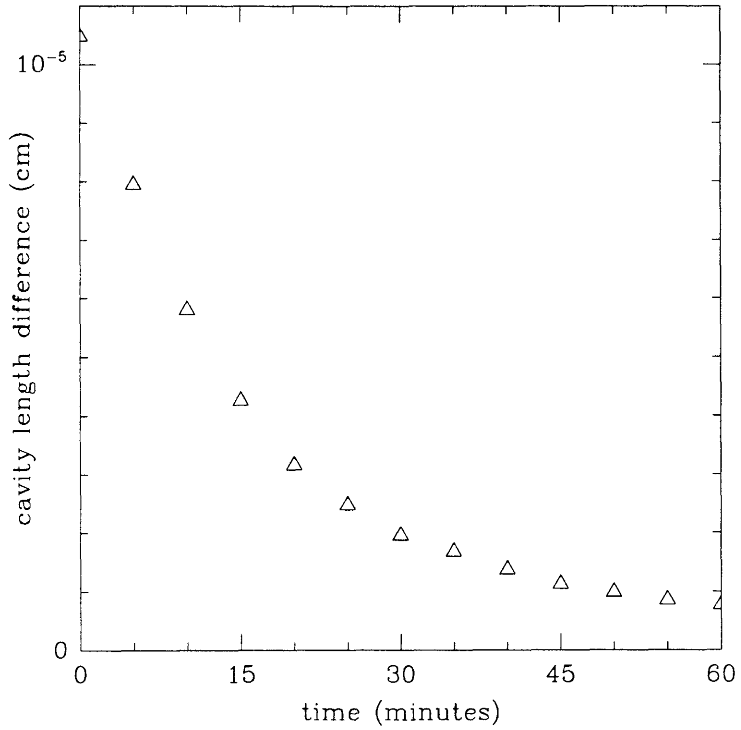

Once the thermally tuned cavity is near resonance, the error signal from its reflected light becomes available. This error signal is fedback into the heater control and acts as the servo to keep this cavity locked on resonance. The first two poles in the servo loop come from the jewel that has a time constant of 23.8 minutes and the heater strip that has a time constant of 12.4 seconds. The servo loop has some lead-lag compensation with a pole-zero pair at 10.6 mHz-120 mHz to gain some phase margin over the second pole. There were no other filters added to the loop. The gain was set to stop the loop from oscillating. The typical forward DC gain was 30.

The error signal from the thermally tuned cavity does give the heater an adequate control to keep the cavity locked on resonance. In this experiment, however, the important consideration is the amount of common mode rejection obtained by interferometrically combining the outputs of two cavities. Since the losses of the cavity mirrors do not necessarily match exactly, the finesse or optical gain of each cavity can be slightly different. This problem is overcome by holding the poorer cavity on resonance and the better cavity off-resonance. In this case, the feedback signal for thermal tuning comes from adding a frequency modulation to the MISER and then mixing it with the interferometer output. This produces a signal that minimizes the transmission of frequency noise through the interferometer (see section 4.8 on residual frequency noise).

4.5 Mode Matching and Cavity Alignment

The mode matching of the light beam to the cavity input is achieved by using a single mode fibre, a GRIN lens and a regular lens. The light is coupled into the fibre by focusing the MISER output beam onto a GRIN lens and then aligning the fibre with the output from the GRIN to achieve a typical coupling efficiency of about 50%. The fibre is then epoxied in place. This set up remains stable over time with no change in the coupling efficiency detectable.

The fibre is threaded through a small hole in a flange to the vacuum system. The plastic jacket is carefully removed and the hole is sealed with epoxy.

Inside the vacuum system, the output from the fibre is coupled through another GRIN lens. This takes a quickly diverging beam from the fibre output and collimates it. The output from the GRIN is checked using a CCD wavefront analyzer. When it looks sufficiently gaussian, it is epoxied in place. The CCD wavefront analyzer is then used to make a series of measurements of the beam waist as a function of distance.

Once the beam waist and its position are characterized, a one lens solution to the cavity mode matching is attempted. If this is possible, the lens is installed at the appropriate distance from the fibre and the CCD wavefront analyzer is again used to make a series of measurements of the beam waist as a function of distance. Small adjustments are made if necessary. Finally, the fibre-GRIN combination and lens is placed at the appropriate distance from the cavity to achieve the proper mode matching.

If the one lens solution does not give reasonable possibilities for distances between components or lens focal length, a two lens solution can be used. In this experiment, a one lens solution was used.

The alignment of the two cavities simultaneously is tricky, but is really just a process of finding a position for the jewel whereby each beam hits a spot on its respective curved mirror that is normal to the flat, thin mirror. The biggest problem initially is to find a place that is close enough to alignment so that the different spatial modes of the light are visible. Since the transmission of the mirrors is very small (22 parts per million or ppm.), there is almost no light coming through the mirrors unless the cavity is aligned and resonant. Also, since the light is at 1.06 μm, one must use CCD cameras to see the light beam.

The first step is to dead reckon the alignment as much as possible. The two beams from the Köster prism should be parallel and aimed to the centre of each spherical. Then, the frequency of the MISER should be swept through a few spectral ranges. Since the time constant for the thermal tuning is about 1 second, the sweep rate must be about 1/10 Hz for the frequency to change smoothly. By placing a CCD camera directly at the output of each cavity, light whose frequency is resonant with an optical mode of the cavity can be seen. The positioning knobs of the stages that hold the jewel are then adjusted until a TEM_{00} mode is seen as one of the optical modes of each cavity. This involves turning the adjustment knobs in a way that symmetrizes the high order spatial modes coming out of the cavities.

Once a TEM_{00} mode is visible in each cavity, a frequency modulation is impressed on the MISER PZT (at about 100 Hz) and the MISER is tuned thermally until a TEM_{00} mode is resonant inside a cavity. This output then can be maximized visually by looking at the CCD television screen output.

The final part of the alignment involves locking each cavity independently and making adjustments until there is a maximum output (or some compromise) from each cavity.

The actual movement of the beams and the jewel is done by various means. The parallelism of the input beams is controlled by the input angle to the Köster prism and their separation by translating the Köster prism. The jewel sits on a flexure mount that allows translation in the two dimensions perpendicular to the light beam and tilt in all three degrees of freedom. This allows enough control to align both cavities.

Finally, the output Köster prism must be aligned so that the cavity output beams overlap in position and angle. This is done by locking each cavity independently and measuring the position of its beam on the wavefront analysis camera at two widely separated distances. The Köster prism is moved until each beam is in the same spot at the near and far measurement position. The best contrast achieved in this way was 0.9. This was limited by the angular difference between the two interfering beams.

4.6 Output Signal Extraction

Since the MISER intensity is not shot noise limited until about 10 MHz, the phase of the light must be interrogated at a sufficiently high frequency so that excess amplitude noise is not added to the signal. Also, the Fabry-Perot cavities have a bandwidth on the order of tens of kHz so that the amplitude noise is not filtered in the measurement band (from 0 to 20 kHz), but is filtered at the fringe interrogation frequency (7 MHz).

The output from each cavity is modulated anti-symmetrically by a Pockels cell. The electric field at the cavity output is

$$\begin{aligned} \varepsilon_1 &= r_1 t_2 A_1 e^{i(\varphi_1+\varphi_m)} \times \varepsilon_0 \\ \varepsilon_2 &= t_1 r_2 A_2 e^{i(\varphi_2-\varphi_m)} \times \varepsilon_0 \end{aligned} \tag{4.6.1}$$

where r_1, t_1 and r_2, t_2 are the reflection and transmission coefficients of the first and second Köster prism beamsplitter and A_1, A_2 are the transmission amplitudes of each cavity. The dark fringe output of the interferometer is

$$\begin{aligned}
&\varepsilon_{anti} = \varepsilon_0 A_2 t_1 r_2\, e^{i(\varphi_2-\varphi_m)} - \varepsilon_0 A_1 r_1 t_2 e^{i(\varphi_1+\varphi_m)} \\
&\varphi_m = \Gamma \sin(\omega_m t) \\
&I_{anti} = I_{trans}\times \\
&[1 - K[J_0(2\Gamma)\cos(\varphi_2-\varphi_1) - 2J_1(2\Gamma)\sin(\varphi_2-\varphi_1)\sin(\omega_m t)]] \\
&I_{trans} = \varepsilon_0^2\Big[(t_1 r_2 A_2)^2 + (r_1 t_2 A_1)^2\Big] \\
&K = \frac{2 r_1 t_1 r_2 t_2 A_1 A_2}{(t_1 r_2 A_2)^2 + (r_1 t_2 A_1)^2}
\end{aligned} \tag{4.6.2}$$

The term, ε_0^2, in the output intensity, I_{trans}, depends upon the output power of the MISER and the transmission or throughput of the optics

$$\varepsilon_0^2 = throughput \times output\; power \tag{4.6.3}$$

This signal is then demodulated at ω_m.

The dependence of this signal on length is

$$\begin{aligned}
\frac{dI}{dl} &= 2rt\varepsilon_1\varepsilon_2 J_1(2\Gamma)[A_1A_2\cos(\varphi_2-\varphi_1)\left(\frac{d\varphi_2}{dx} - \frac{d\varphi_1}{dx}\right) \\
&+ \sin(\varphi_2+\varphi_1)\left(A_1\frac{dA_2}{dx} + A_2\frac{dA_1}{dx}\right)]\frac{2\omega}{c}
\end{aligned} \tag{4.6.4}$$

For both cavities on resonance, this reduces to

$$\begin{aligned}
\frac{dI}{dl} &= 2r_1t_1r_2t_2\varepsilon_0^2 J_1(2\Gamma)A_1A_2\left(\frac{d\varphi_2}{dx} - \frac{d\varphi_1}{dx}\right)\frac{2\omega}{c} \\
&= I_{trans}\times KJ_1(2\Gamma)\left(\frac{d\varphi_2}{dx} - \frac{d\varphi_1}{dx}\right)\frac{2\omega}{c}
\end{aligned} \tag{4.6.5}$$

If both cavities are not exactly matched, then one cavity is locked on resonance ($x = 0$) and the other is held slightly off-resonance. This changes the above equation to

$$\begin{aligned}
\frac{dI}{dl} &= 2r_1t_1r_2t_2\varepsilon_0^2 J_1(2\Gamma)[A_1A_2\cos(\varphi_2)\left(\frac{d\varphi_2}{dx} - \frac{d\varphi_1}{dx}\right) \\
&+ \sin(\varphi_2)\left(A_1\frac{dA_2}{dx}\right)]\frac{2\omega}{c}
\end{aligned} \tag{4.6.6}$$

4.7 Shot Noise Limit

Assuming the system sensitivity is shot noise limited, the calculation for the sensitivity goes as follows. The measured throughput of the optics is:

$$\begin{gathered}
throughput = (Faraday\; isolator = 0.7)(lens = 0.96)^2\times \\
(fibre\;\&\; GRIN = 0.5)(lens = 0.96)^2(Pockels\; cell = 0.86)^2\times \\
(mode\;\; match = 0.9)(Koster\; prism = 0.9)^2\times \\
(polarizing\; beamsplitter = 0.98)\times \\
(Pockels\; cell = 0.86)^2(Window = 0.96)^2 \\
= 0.11
\end{gathered} \tag{4.7.1}$$

The shot noise intensity is

$$I_{shot} = \sqrt{\frac{h\nu I_{DC}}{\eta}} \tag{4.7.2}$$

The detector efficiency η is 0.43. For both cavities on resonance, the DC intensity is

$$I_{DC} = [1 - KJ_0(2\Gamma)]I_{trans} \tag{4.7.3}$$

The position noise is then the result of this intensity noise

$$\begin{aligned} equivalent\ displacement\ noise &= \frac{I_{shot}}{\frac{dI}{dl}} \\ &= \frac{\sqrt{h\lambda c}}{4\pi J_1(2\Gamma)K}\sqrt{\frac{1 - KJ_0(2\Gamma)}{\eta I_{trans}}}\frac{1}{\frac{d\varphi_2}{dx} - \frac{d\varphi_1}{dx}} \\ &= \frac{1.76 \times 10^{-11}}{J_1(2\Gamma)K}\sqrt{\frac{1 - KJ_0(2\Gamma)}{I_{trans}}}\frac{1}{\frac{d\varphi_2}{dx} - \frac{d\varphi_1}{dx}} \end{aligned} \tag{4.7.4}$$

where I_{trans} is the transmitted intensity as defined in equations 4.6.2 and 4.6.3. Since the signal is antisymmetric, the derivative of the phase is also antisymmetric

$$\frac{d\varphi_2}{dx} - \frac{d\varphi_2}{dx} = 2\frac{d\varphi}{dx}|_{x=0} \tag{4.7.5}$$

The best possible sensitivity occurs when both cavities are on resonance and each cavity is exactly the same. If one also assumes a perfect contrast (K=1) and a modulation index that approaches 0 (Γ<<1), the above expression simplifies to

$$equiv.\ displ.\ noise = \frac{1.76 \times 10^{-11}}{\sqrt{I_{trans}(ergs/sec)}\left(2\frac{d\varphi}{dx}\right)} \tag{4.7.6}$$

The transmitted intensity in terms of mirror losses and transmissions for both cavities on resonance is

$$\begin{aligned} I_{trans} &= throughput \times I_{MISER} \times \left[(t_1 r_2 A_2)^2 + (r_1 t_2 A_1)^2\right] \\ r_1 = t_1 &= r_1 = t_1 = 1/\sqrt{2} \\ A_1(0) = A_2(0) &= \frac{T}{L+T} \\ I_{trans} &= loss \times I_{miser} \times \frac{1}{2} \times \left(\frac{T}{L+T}\right)^2 \\ I_{trans} &= 2.2 \times 10^4\left(\frac{T}{L+T}\right)^2 \end{aligned} \tag{4.7.7}$$

The derivative of the phase is

$$\frac{d\varphi}{dx}|_{x=0} = \frac{(1 - L - T)}{L+T} \tag{4.7.8}$$

Putting all of this together gives the sensitivity as a function of mirror transmission and loss

$$equiv.\ displ.\ noise = 5.9 \times 10^{-14} \frac{(L+T)^2}{T(1-L-T)}\ cm/\sqrt{Hz} \tag{4.7.9}$$

For L<<1, the maximum sensitivity occurs when T=L.

Current multi-layer dielectric coating technologies allow mirror losses on the order of a few parts per million. Since some degradation of the mirror can occur from the accumulation of dirt on the surface, the transmission is chosen to be more than the expected loss. It is clear from figure 4.7.1 that a sensitivity of $10^{-17} cm/\sqrt{Hz}$ is a reasonable goal.

Figure 4.7.1 Plot of sensitivity vs. Transmission for different losses

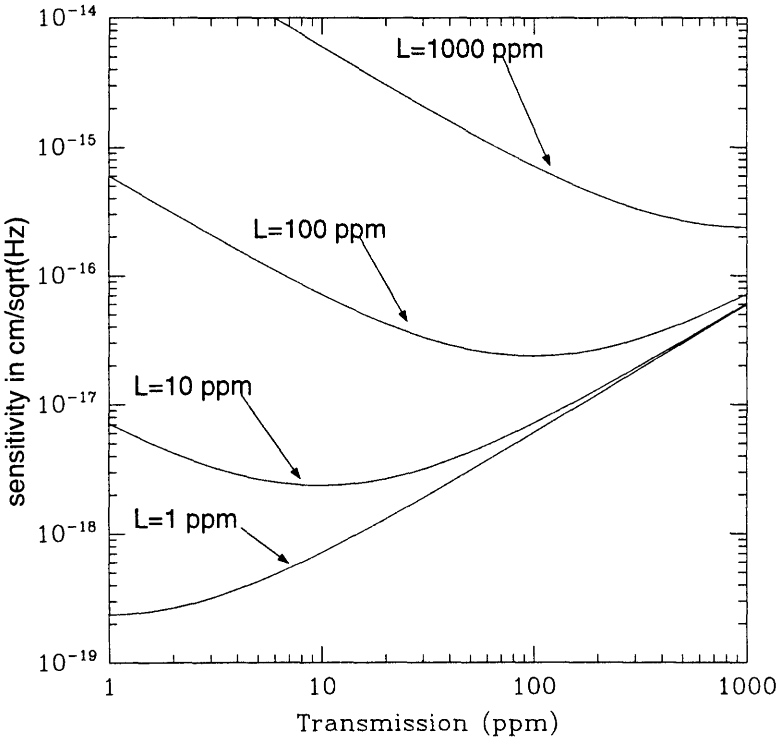

4.8 Residual Frequency Noise

The MISER is an inherently stable laser. Its frequency noise at a few kHz is typically less than 10 $Hz/\sqrt{Hz}$ and falls as $1/\sqrt{f}$ $(\delta\nu^2(f) \propto 1/f)$. However, it still adds a significant noise term unless it is cancelled exactly by the interferometer through common mode rejection.

If one cavity is held on resonance and the other off-resonance, the dependence of the interferometer output noise on frequency noise is

$$\begin{aligned}
noise &= \frac{\frac{dI}{df} \times \Delta f}{\frac{dI}{dl}} \\
\frac{dI}{df} &= 2r_1t_1r_2t_2\varepsilon_0^2 J_1(2\Gamma)[A_1A_2\cos(\varphi_2)\left(\frac{d\varphi_2}{dx} - \frac{d\varphi_1}{dx}\right) \\
&\quad + \sin(\varphi_2)\left(A_1\frac{dA_2}{dx}\right)]\frac{4\pi l}{c} \\
\frac{dI}{dl} &= 2r_1t_1r_2t_2\varepsilon_0^2 J_1(2\Gamma)[A_1A_2\cos(\varphi_2)\left(\frac{d\varphi_2}{dx} + \frac{d\varphi_1}{dx}\right) \\
&\quad + \sin(\varphi_2)\left(A_1\frac{dA_2}{dx}\right)]\frac{2\omega}{c} \\
equiv.\ displ.\ noise &= \epsilon_{freq.\ noise} \times \frac{l}{f} \times \Delta f \\
equiv.\ displ.\ noise &= 3.15 \times 10^{-14} \times \epsilon_{freq.\ noise} \times \Delta f\ cm/\sqrt{Hz} \\
\epsilon_{freq.\ noise} &= \frac{A_1A_2\cos(\varphi_2)\left(\frac{d\varphi_2}{dx} - \frac{d\varphi_1}{dx}\right) + \sin(\varphi_2)(A_1\frac{dA_2}{dx})}{A_1A_2\cos(\varphi_2)\left(\frac{d\varphi_2}{dx} + \frac{d\varphi_1}{dx}\right) + \sin(\varphi_2)(A_1\frac{dA_2}{dx})}
\end{aligned} \tag{4.8.1}$$

(Note that the phases for the two cavities are subtracted by the interferometer. Since the position displacement is anti-symmetric for the motions measured in this experiment, its signal will add while the frequency noise which is symmetric will subtract).

Figure 4.8.1 A plot of $\epsilon_{\text{freq. noise}}$ vs. δx for a transmission of 22 ppm, a loss of 20 ppm per mirror for one cavity and a loss of 10 ppm per mirror for the better cavity. The offset parameter δx is $\frac{2\omega}{c} \times \delta l$ where δl is the distance the cavity is off-resonance. Since the RMS noise is the important consideration, the $| \epsilon_{freq.\ noise} |$ is the relevant parameter. The FWHM for a cavity with a transmission of 22 ppm and a loss of 10 ppm per mirror is 17.2 kHz or 6.4×10^{-5} in units of δx. The better cavity is thus detuned to a point that is still well within its bandwidth.

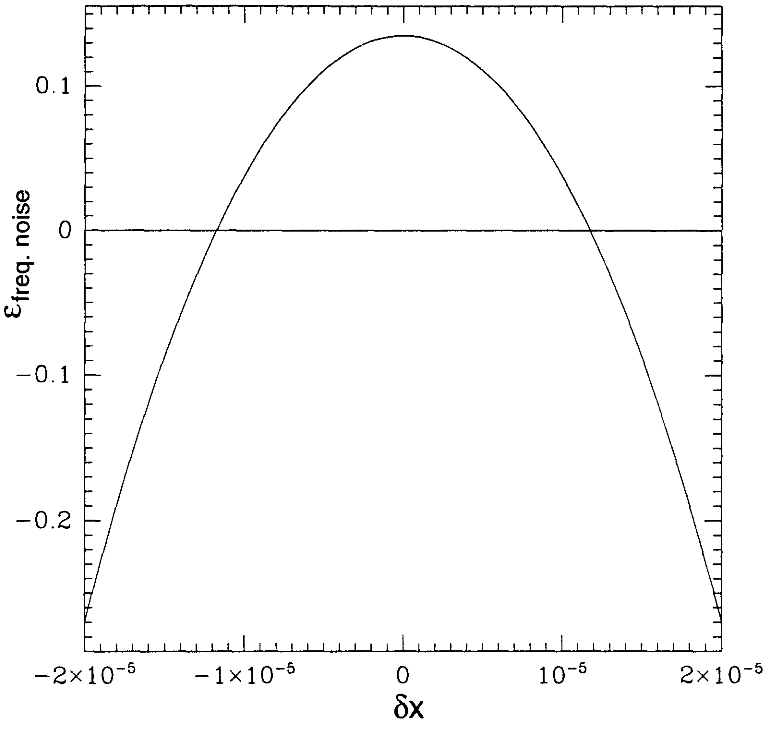

To achieve a sensitivity of $10^{-17} cm/\sqrt{Hz}$, the factor $\epsilon_{\text{freq. noise}}$ must be on the order of 10^{-5}. Since this requires the offset to be held to approximately one part in 10^4 (see figure 4.8.2) an additional servo that matches the two cavities and nulls the frequency noise is necessary.

Figure 4.8.2 A plot of | $\epsilon_{freq.\ noise}$ | vs. x for the same parameters as figure.4.8.1 The offset must be held to within one part in 10^4 to achieve sufficient frequency noise rejection.

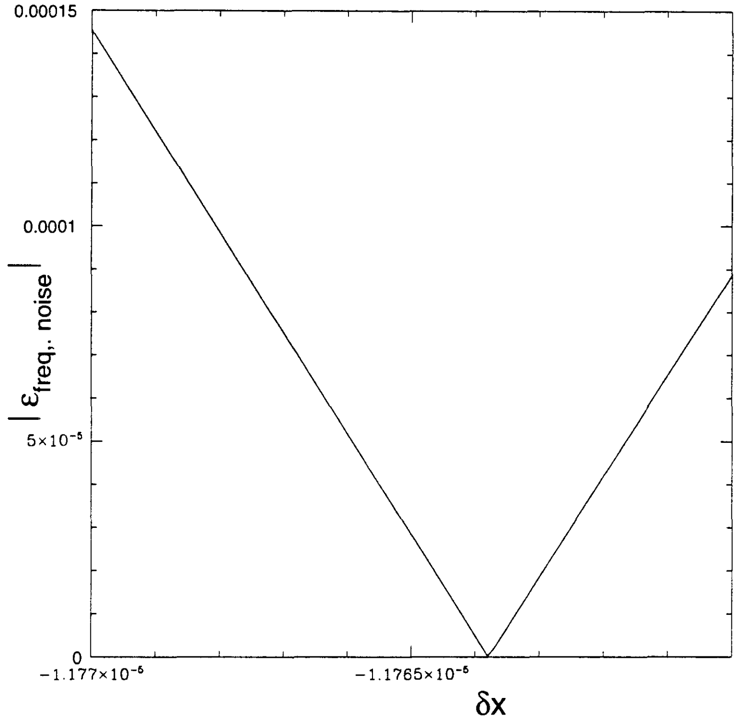

A single tone (in this case, 50 kHz) of FM is added to the frequency of the MISER by putting a signal into the PZT frequency control. The optimum operating condition for the system is one where any frequency noise on the MISER, including this deliberate FM, is cancelled by the interfering the two output beams. By taking the interferometer output and mixing it with the FM signal in a lock-in amplifier, an error signal that minimizes the frequency noise transmission of the interferometer is obtained. The reflection lock error signal is disabled and this new error signal is then connected to the heater control.

Chapter 5 Experimental Results

5.1 Measured Optical Properties

Very small losses on the order of a few ppm. are necessary to obtain the desired sensitivity for this experiment. Since even a small amount of contamination can increase the losses by a few hundred ppm, a great deal of care is required to insure that the mirrors remain clean. Also, since the amount of light transmitted through the cavities decreases with increased mirror losses (see figure A.4 in appendix A), the experiment becomes more difficult to perform both from a practical viewpoint (one must be able to see the transmitted light beams readily on a CCD camera) and because the transmitted light intensity should be larger than the dark noise of the photodetector and its electronics.

Table 5.1.6 gives a list of the expected and measured values for various cavity properties. The history of the mirrors requires some explanation. The mirrors originally had a specified transmission of 22 ppm and a loss of less than 5 ppm. Unfortunately, during the initial optical contacting process, the mirrors were contaminated by an improper cleaning technique that was used despite a work order that explicitly gave instructions to do otherwise. After this was thoroughly investigated, the jewel was uncontacted, cleaned and recontacted. The measured losses then more closely approached their predicted values. Unfortunately, contaminations from the vacuum system and the dry nitrogen back fill process slowly increased the losses of the mirror over time.

Table 5.1.6 Properties of one of the Fabry-Perot cavities. The predicted values come from the mirror specifications. The measured values were the those measured initially when the optics were delivered. The cleaned values are after the optics were disassembled, cleaned and reassembled. Finally, the actual values are those of the cavity from when the data presented in the subsequent sections was taken.

	predicted	measured	cleaned	actual
Transmission	22 ppm	22 ppm	22 ppm	22 ppm
Loss	5 ppm	440 ppm	9 ppm	106 ppm
Bandwidth	15 kHz	250 kHz	17 kHz	69 kHz
Finesse	1.2×10^5	6.7×10^3	9.9×10^4	2.4×10^4

The linewidths of the cavities were measured by sweeping the frequency of the MISER and then measuring the FWHM of the output intensity. This was checked against the cavity transmission and the cavity reflection to insure consistency.

Figure 5.1.1 shows a typical transmission intensity spectrum for each cavity as the MISER frequency is swept across a few spectral ranges. One cavity is well aligned (only the TEM_{00} mode is visible) while the other is slightly misaligned (both the TEM_{01} and TEM_{10} modes are visible). Since the cavity losses were not well matched, the better cavity was slightly misaligned so that its output intensity was closer to that of the worse cavity. This was fortunate since the alignment of both cavities simultaneously was difficult to achieve. The varying heights of each transmitted peak comes from the time sampling window limitations of the storage oscilloscope for the given sweep rate.

Figure 5.1.1 The output intensity of each cavity as the frequency of the MISER is swept across several free spectral ranges.

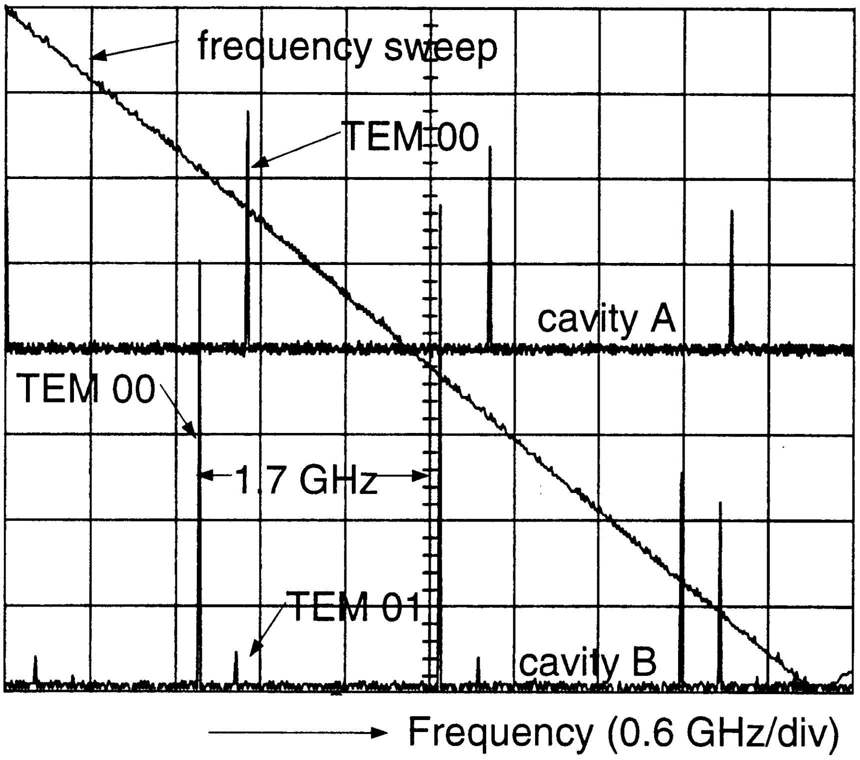

Figure 5.1.2 shows the transmitted intensity and the reflection lock error signal as the frequency of the MISER is swept through the cavity resonance. The blow up along the frequency axis of the error signal shows its change in slope as the frequency moves off of the resonance.

Figure 5.1.2 The transmitted intensity and reflection lock error signal as the frequency of the MISER is swept through a cavity resonance.

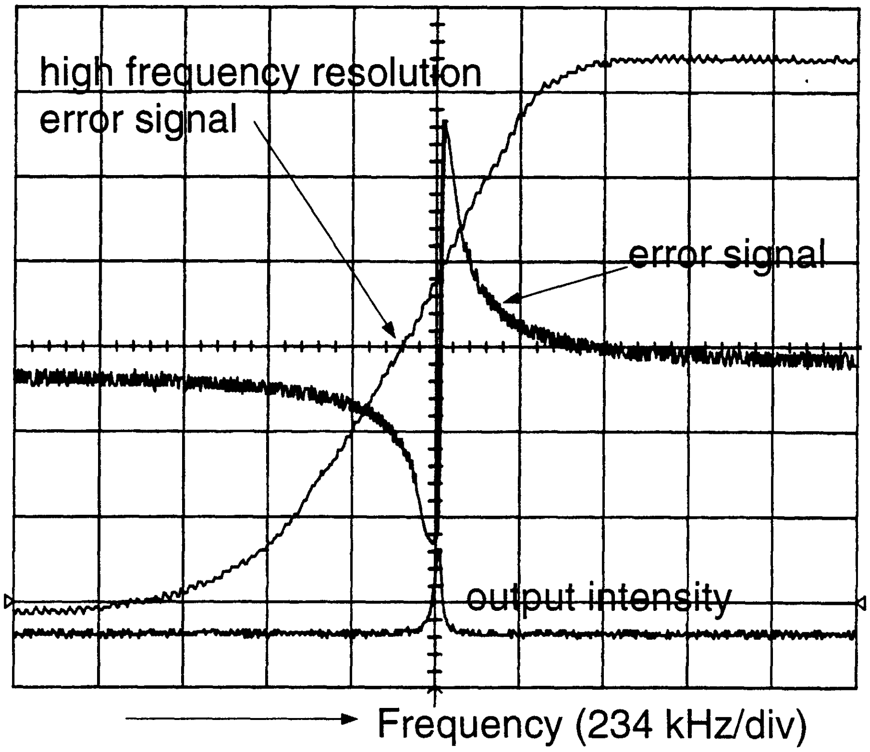

5.2 Measured Q's of the Plate

Once the optical system properties are understood sufficiently, the actual thermal noise experiment can begin. The first data was a measurement of both the frequencies and Q's of the various normal modes of the plate in air.

The electrostatic driver was used to excite the normal modes of the plate. The electrostatic driver is a 0.750 ″ stainless steel ball that is placed as close to the fused quartz plate as possible without actually touching it (usually less than 0.050″). A dielectric placed near the ball will feel a force acting upon it since the ball produces an electric field with a gradient. The force is proportional to the square of the voltage applied to the ball. The SS ball is biased to between 500 V and 800 V with a DC potential. An AC voltage of about 100 V is superposed on the DC potential. This produces a linear force at the frequency of the AC voltage that is proportional to the bias voltage times the AC voltage.

$$\begin{aligned} F &\propto V^2 \\ &\propto (V_{DC} + V_{AC}\sin(\omega t))^2 \\ &\propto V_{DC}^2 + V_{DC}V_{AC}\sin(\omega t) + V_{AC}^2\frac{1-\cos(2\omega t)}{2} \\ &\propto V_{DC}V_{AC}\left[\sin(\omega t) + D.C\ term + \frac{V_{AC}}{V_{DC}}\cos(2\omega t)\right] \end{aligned} \tag{5.2.1}$$

The first series of measurements in air showed that all of the modes except the fundamental one

$$(n = 0, k = 0) \tag{5.2.2}$$

were split in frequency by about 10%. These frequencies were, in turn, split by another 0.5%. Since the frequency of a mode is

$$f \propto \frac{\lambda^2 h}{r^2} \tag{5.2.3}$$

then f/λ^2 must give some constant that determines the ratio h/r^2. Figure 5.2.1 shows such a plot. Both the 10% and 0.5% splittings in frequency must be due to some irregularity in the shape or clamping condition. The fabrication specifications for the optical components required tolerances of less than 0.005″. This seems like the most likely explanation for the 0.5% splittings. The 10% splittings are too large to be explained by a shape irregularity. It seems most likely that there is some asymmetry in the clamping from the optical contact between the thin plate and the cylinder end. By assigning a clamping radius to each set of frequencies, one finds that the plate is clamped at diameter of 4.5″ and 4.75″. Curiously, the lowest order mode is not visible for the 4.5″ set of frequencies.

Figure 5.2.1 A plot of the constant f/λ^2 vs. λ for normal modes of the plate. The numbers in the parentheses represent the (n, k) of the mode. The triangles represent a set of frequencies that correspond to a clamp diameter of 4.5″. The squares represent a set of frequencies that correspond to a clamp diameter of 4.75″.

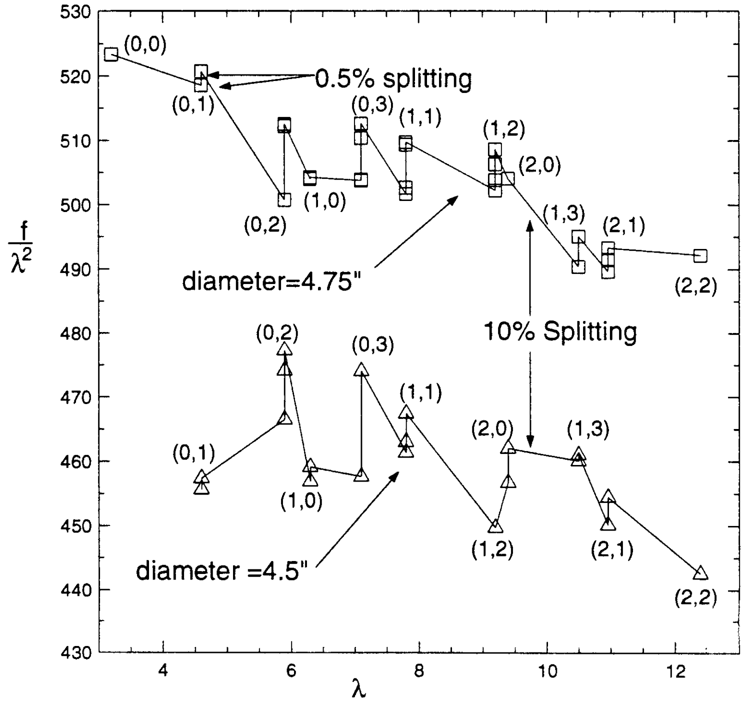

The electrostatic driver was used to map out the sensitivity of different modes to excitation as a function of position on the plate. The results confirmed that the frequencies were properly identified with their respective normal modes. It was also clear that most of the resonances seen were not due to the plate, but to other parts of the jewel including the cylinder and the thick plate on the opposite end of the cylinder.

The Q's of modes were measured by using the electrostatic driver to perform a swept sine transfer function. The FWHM of the peak gives the Q. The first measurements were performed in air and gave Q's on the order of 500 which was unexpectedly low. A quick calculation of losses from frictional air damping shows that it would give a Q of about 500000. Another loss mechanism in air is from friction of the column of air inside the holes in the side of the cylinder against the walls of the hole. A quick calculation here gives a Q on the order of 80000.

Since the Q's in air were rather low, an attempt to understand the frequency dependence of the damping mechanism in air was undertaken by measuring the phase angle between the applied force and the response of the normal mode and fitting the phase for each model. For a viscous damping model, the phase angle is:

$$\tan\delta = \frac{\beta\omega/m}{\omega_0^2 - \omega^2} \tag{5.2.4}$$

and for structure damping model, the phase angle is:

$$\tan\delta = \frac{\omega_0^2\phi}{\omega_0^2 - \omega^2} \tag{5.2.5}$$

Since the bandwidth of the peak is $\omega_{0/Q}$ and the electrostatic drive only has enough force to excite the resonance itself, one can only measure a reasonable transfer function a factor of $\omega_{0/Q}$ outside the resonance. The viscous damping phase angle is then

$$\begin{aligned} \tan\delta &= \frac{\beta(w_0 + \omega_0/Q)/m}{w_0^2 - \omega^2} \\ &= \frac{(1/Q + 1/Q^2)w_0^2}{w_0^2 - \omega^2} \\ &= \frac{(\phi + 1/Q^2)w_0^2}{w_0^2 - \omega^2} \end{aligned} \tag{5.2.6}$$

The difference between the two models will be only a factor of $1/Q^2$ or 4×10^{-6}. The signal to noise was such that the two models were indistinguishable when fit to the measured phase and no conclusions could be made.

When the system is under vacuum (10^{-5} mbar), the resonant frequencies do not change, but the Q's increase to between 7000 and 100000 (see figure5.2.2). Again, a Q of 7000 does seem low for fused quartz.

Figure 5.2.2 A plot of measured Q vs. frequency for the normal modes of the plate. The triangles represent a set of frequencies that correspond to a clamp diameter of 4.5″. The squares represent a set of frequencies that correspond to a clamp diameter of 4.75″.

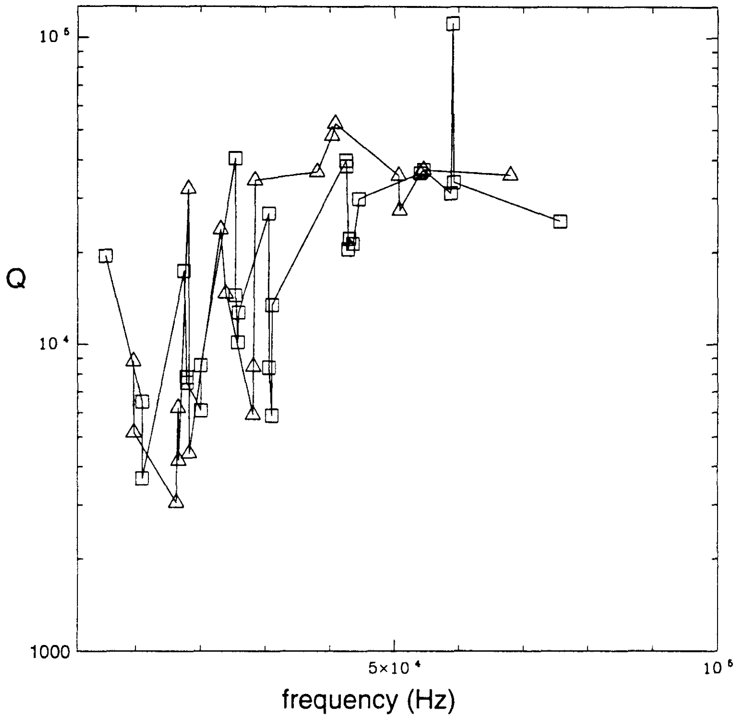

There were many other resonances besides those of the thin plate. Most of these can be attributed to either the cylinder of the jewel or the 1″ thick plate where the small mirrors are optically contacted. They all have Q's on the same order as those of the thin plate (see figure 5.2.3).

Figure 5.2.3 Plot of the measured Q vs. frequency for every resonance that could be seen. Most of the resonances are not from the plate.

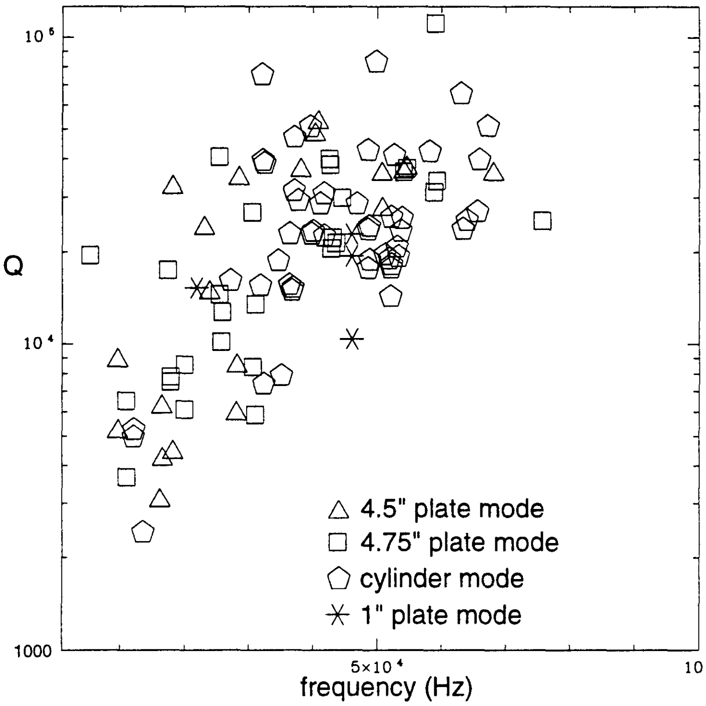

5.3 Measured Noise Spectrum

The noise spectrum was measured on a HP3562A Dynamic Signal Analyzer and is displayed for different frequency spans. The noise signal from the reflection lock control was calibrated by measuring its slope. The frequency of the MISER was swept and an error signal was recorded as in figure 5.1.2. The x axis was converted into units of frequency by measuring the distance between the two 5.18 MHz sidebands that were impressed on the light. The frequency of the sidebands could be easily measured on the oscilloscope. This gives a calibration in terms of volts/Hz. Since the length of the cavity is known, this can be converted into a signal of volts/cm by using the relation

$$\frac{\Delta l}{l}=\frac{\Delta f}{f}=\frac{\Delta f\lambda}{c} \tag{5.3.1}$$

Since the bandwidth of the frequency control servo is under 2 kHz, it is safe to use this open-loop calibration at frequencies above 2 kHz when the loop is closed.

The calibration for the interferometer output is obtained by relating the phase dependence of the output signal to the finesse of the Fabry-Perot cavity. The Pockels cell is calibrated by measuring the amount of voltage necessary to go from the bright to the dark fringe or a change in phase of π. Then, the Pockels cell phase is changed by putting a known voltage on it. The interferometer output signal is measured to obtain its dependence on this induced phase change. Finally, the linewidth of the cavity is measured. This gives a measure of the amount of phase accumulated by storage in the cavity and relates the phase dependence of the light in the cavity to changes of length of the cavity.

$$\begin{aligned} \frac{d\varphi}{dl} &\approx \frac{1}{T+L}\frac{2\omega}{c} \\ \Delta f &\approx \frac{T+L}{\pi}\frac{c}{2l} \\ \frac{d\varphi}{dl} &\approx \frac{2c}{\Delta f l \lambda} \end{aligned} \tag{5.3.2}$$

The power spectra have a steep $1/f$ noise dependence below about 10Hz. There are some low frequency and low Q resonances up to about 500 Hz that correspond to normal modes of the mechanical structure that holds the jewel. The spectrum above 1 kHz is dominated by a broadband white noise with a magnitude on the order of $2 \times 10^{-15} cm/\sqrt{Hz}$. The roll off in the background noise comes from two sources. First, the Fabry-Perot cavities themselves have a bandwidth on the order of 80 kHz when these measurements were taken. The second comes from the tuned resonant RF circuit in the photodetector that had a narrow bandwidth (in this case, also 80 kHz) in order to reduce the noise contribution from the equivalent detector dark photocurrent. The impedance of the circuit at the modulation frequency is increased to make the signal larger. This comes at the expense of a narrower bandwidth.

Figure 5.3.1 A 100 kHz spectrum of the displacement noise output from the interferometer. The large signal at 50 kHz is from the FM applied to the MISER in order to obtain a control signal to reduce frequency noise.

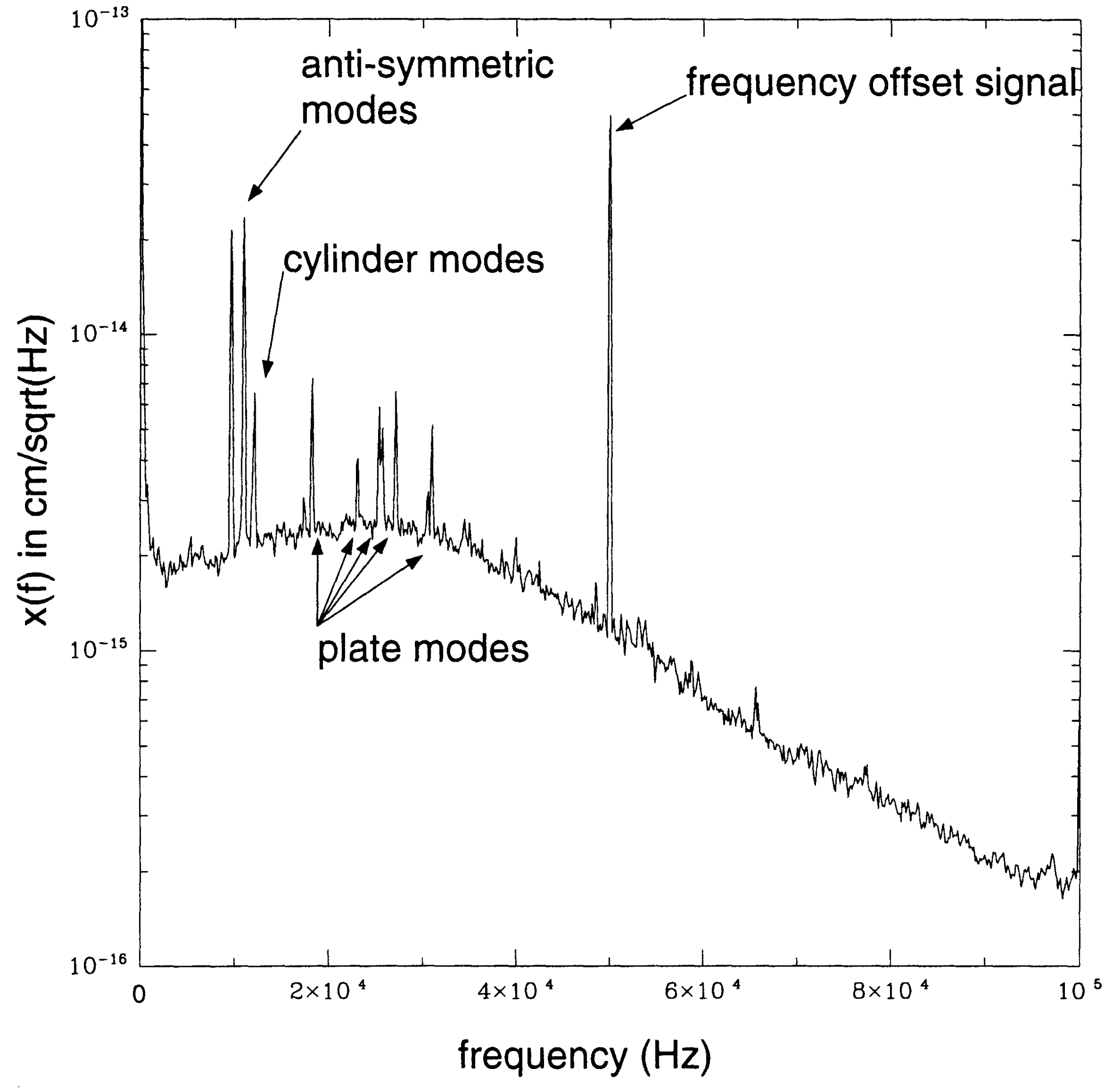

The narrow spectral features are from resonances of the plate and the jewel. The plate anti-symmetric mode of interest here is split and is seen at a frequency of 9.64 kHz and 10.98 kHz. The lowest order mode is at 5.36 kHz and is suppressed with respect to the antisymmetric mode. The next two resonant peaks at 12 kHz are the resonant modes of the cylinder

Figure 5.3.2 A 20 kHz spectrum of the displacement noise output from the interferometer. The 10% splitting between the two antisymmetric (0,1) modes is clearly visible.

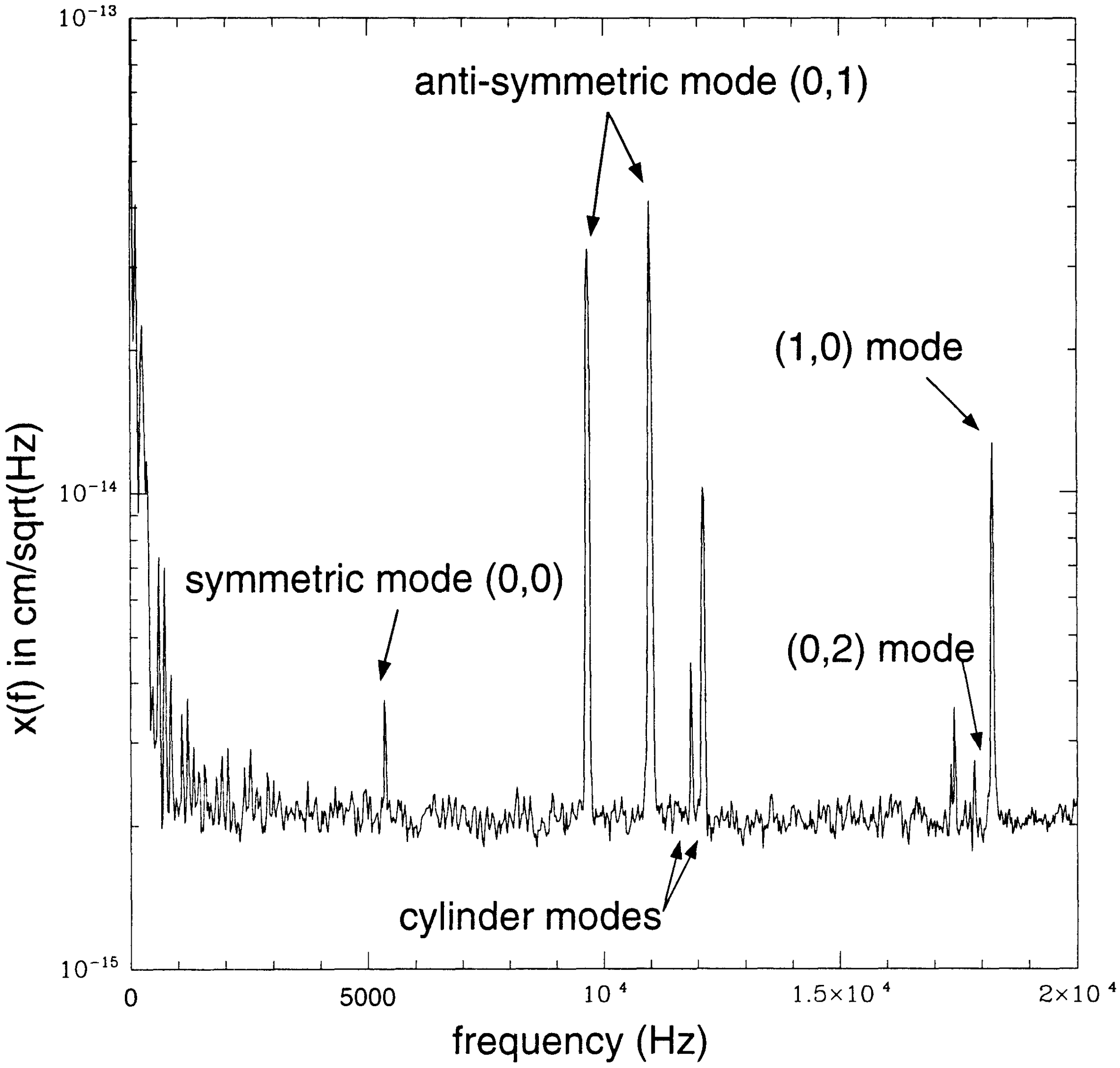

Figure 5.3.3 A 1 kHz spectrum of the displacement noise output from the interferometer. The x's represent multiples of the 60 Hz line frequency.

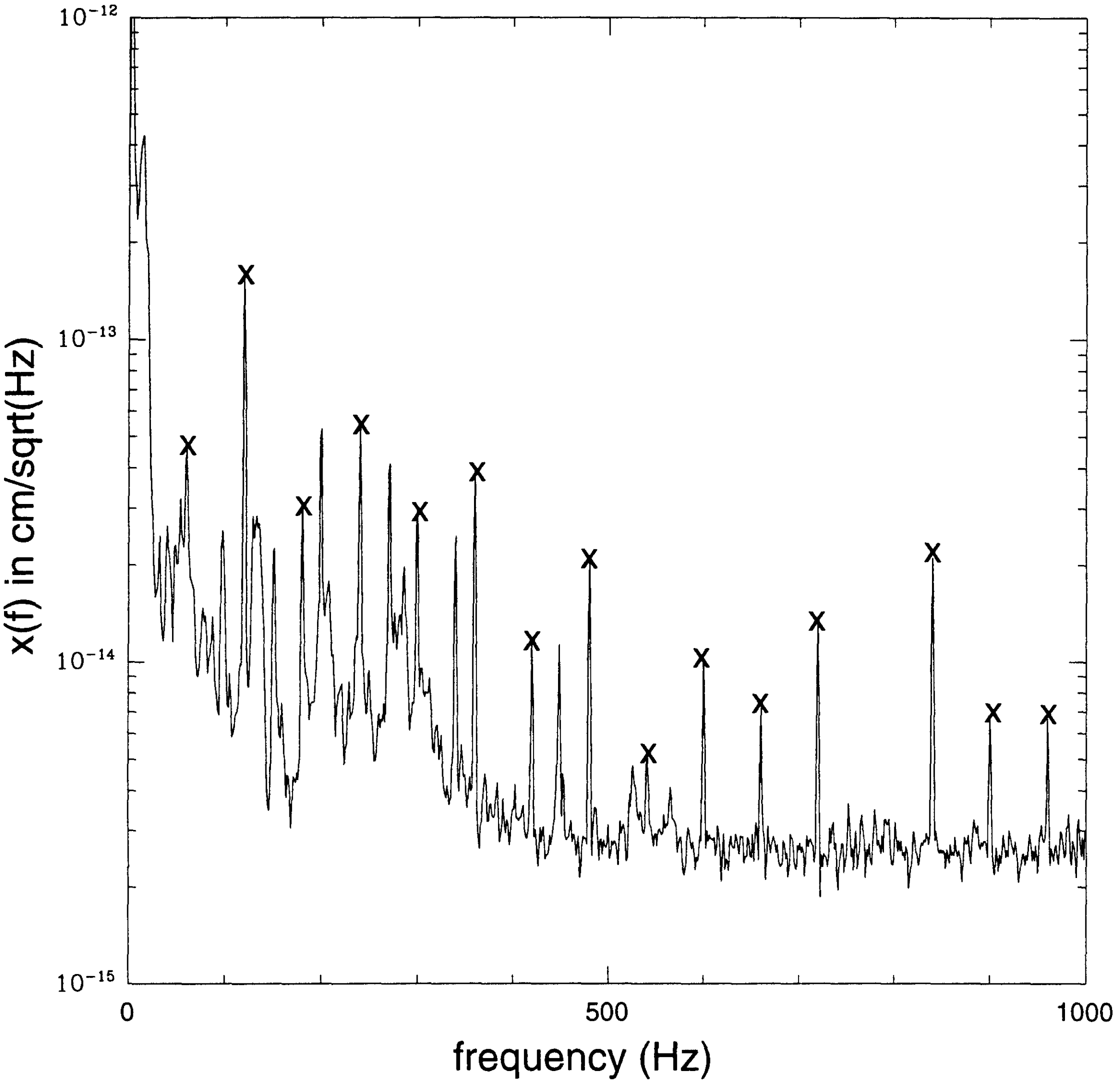

Figure 5.3.4 shows a 1 kHz narrow band spectrum centered at an anti-symmetric resonance. Figure 5.3.5 shows a 25 kHz spectrum of the left most peak from the 0.5% splitting in frequency. Both figures are fit to a curve that follows equation 3.4.13 with parameters

$$\begin{aligned} h &= 0.635\ cm \\ r_0 &= 5.72\ cm \\ r &= 1.93\ cm \\ \phi(\omega) &= 1.54 \times 10^{-4} \\ \cos\theta &= 0.4 \end{aligned} \qquad (5.3.3)$$

It is clear that the background noise cannot be due to the off-resonance noise. The resonance shown in this case has a Q of 6500, yet the peak is only a factor of 150 above the background. The peak height, however, does correspond to a thermally driven process in the plate for that frequency and Q. The usual noise sources in laser interferometry need to be considered in order to determine whether the background is a real signal or simply instrument noise.

Figure 5.3.4 A 1 kHz spectrum of the displacement noise output from the interferometer centered at 10.975 kHz where a peak from the anti-symmetric mode is located. The 0.5% splitting of this mode is clearly visible. A fit of the thermal noise spectrum for one of these modes to the data shows that the off-resonance data is not due to the off-resonance thermal noise spectrum.

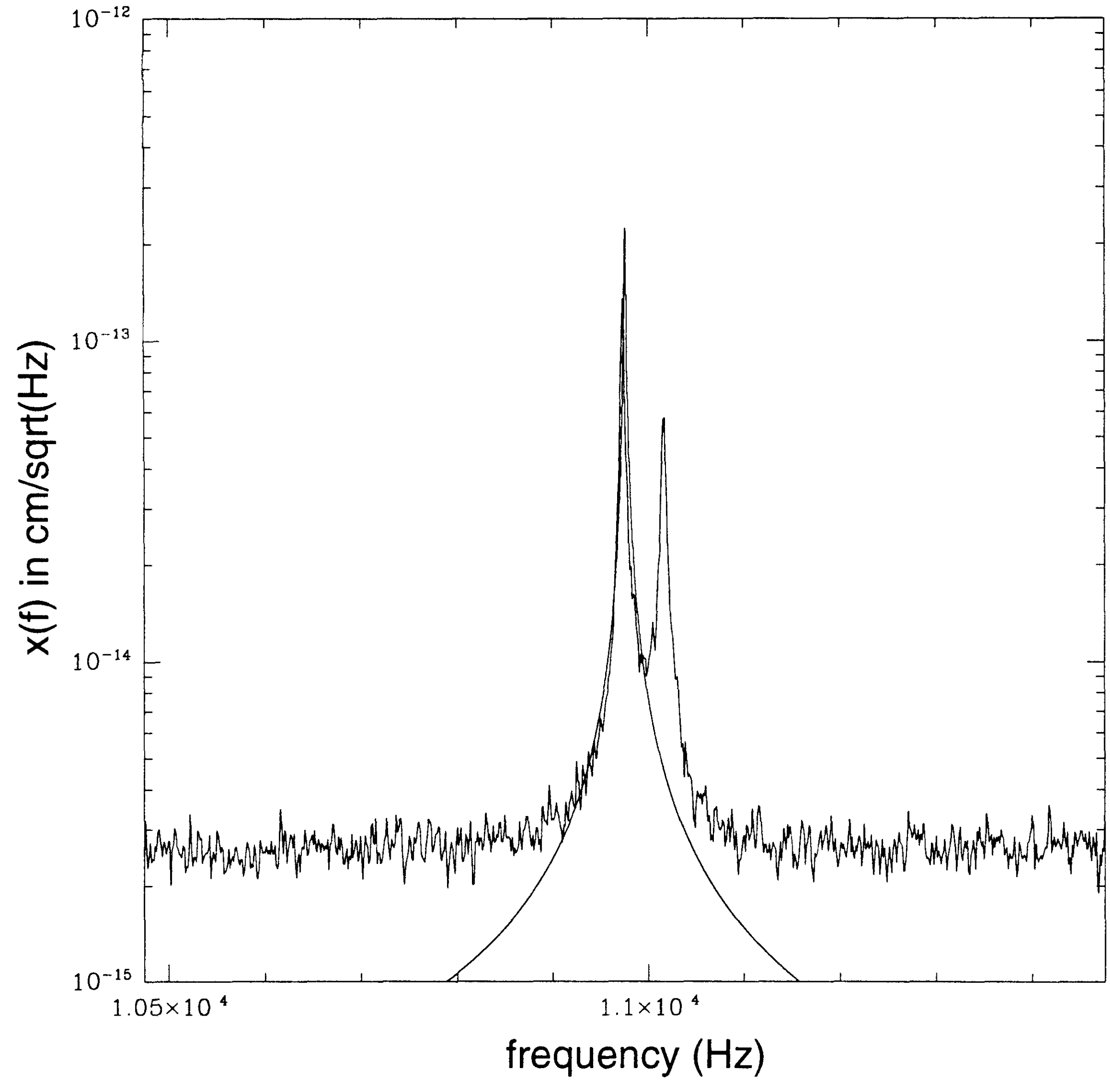

Figure 5.3.5 A 25 Hz spectrum of the displacement noise output from the interferometer centered at 10.975 kHz where a peak from the anti-symmetric mode is located. The Q of this resonance is 6500. The fit to the data shows that it is the thermal noise from a resonant mode.

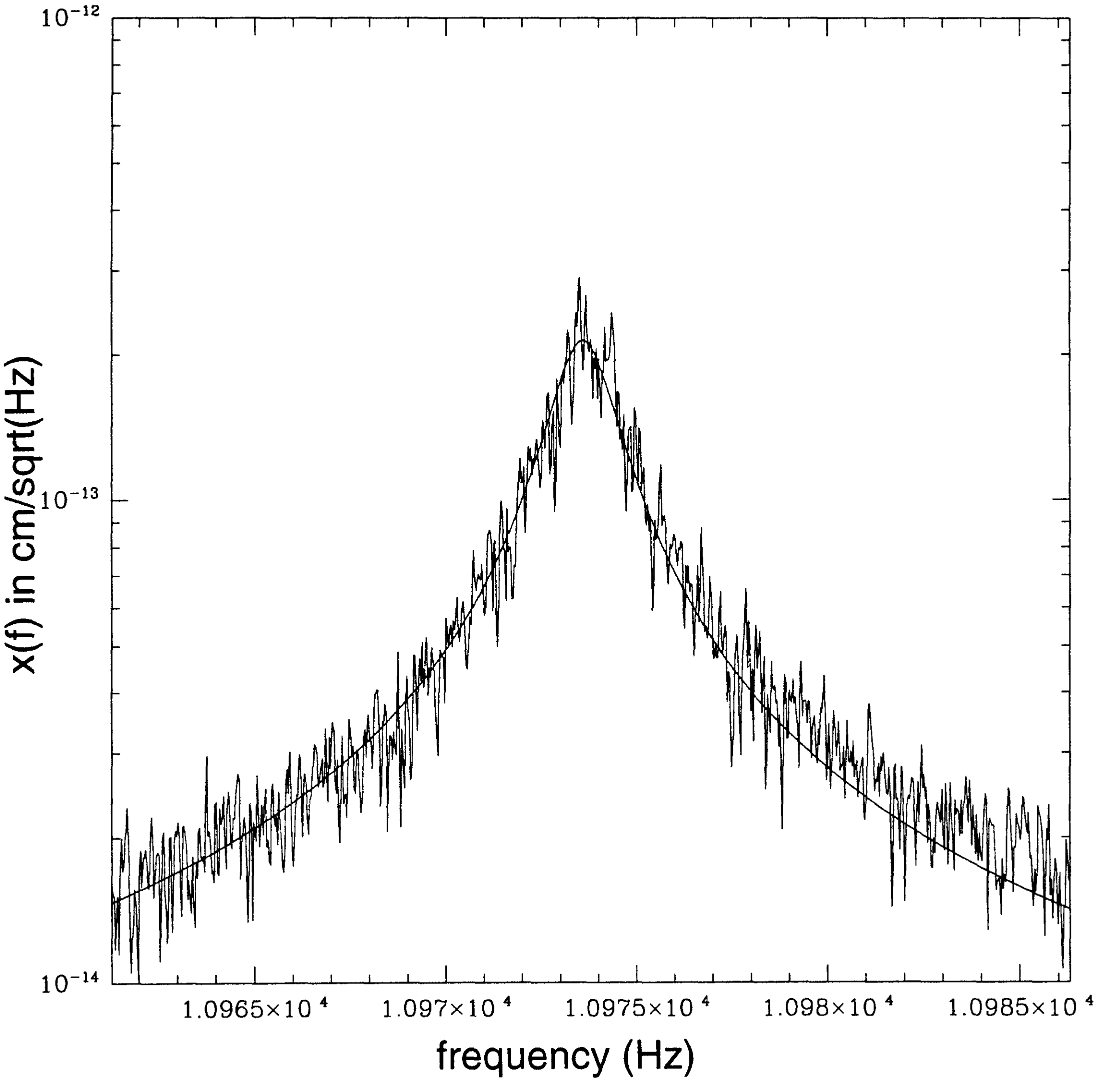

Chapter 6 Instrument Noise

6.1 Electronic Noise

The detector dark current noise had a shot noise equivalent of 2.1 μamps. By the time most measurements were taken, the losses in the mirrors had increased to the point that there was not very much transmitted light intensity through the cavities. The typical dark fringe intensity at the photodetector was 0.15 μamps with a contrast of 0.90. The measured noise signal, however, does comfortably exceed the detector dark noise as can be seen in figures 6.1.1, 6.1.2 and 6.1.3.

Figure 6.1.1 A 100 kHz spectrum of the displacement noise output from the interferometer and of the electronic noise when the photodetector is covered.

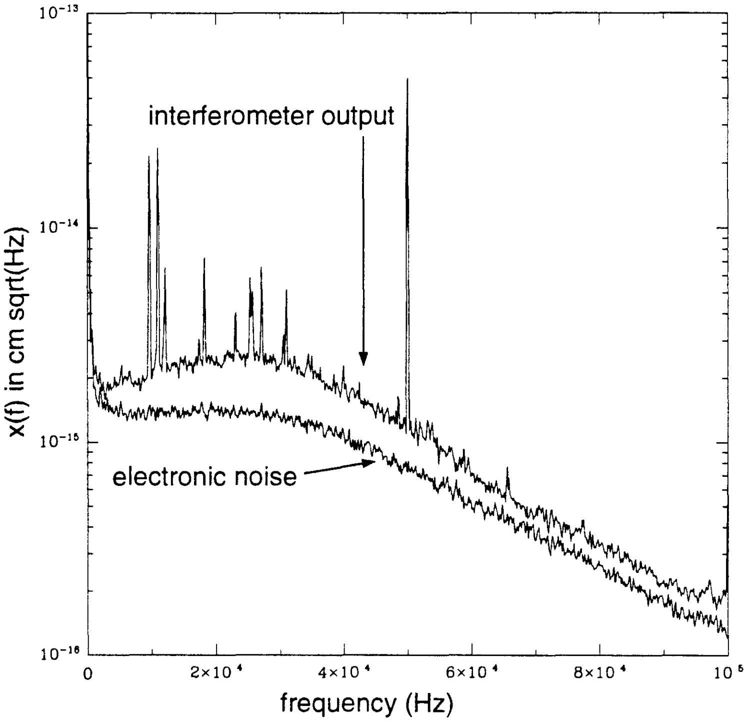

Figure 6.1.2 A 20 kHz spectrum of the displacement noise output from the interferometer and of the electronic noise when the photodetector is covered.

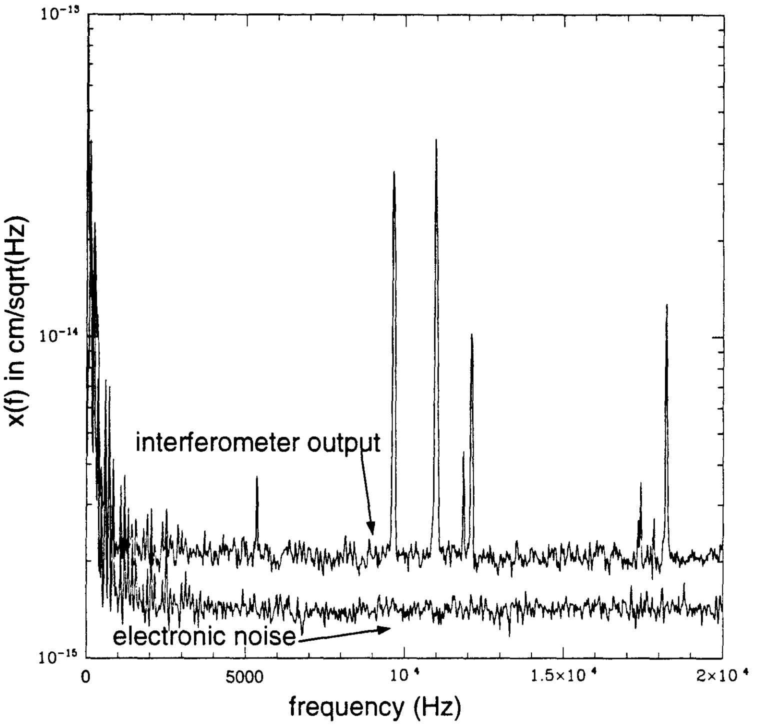

Figure 6.1.3 A 1 kHz spectrum of the displacement noise output from the interferometer.

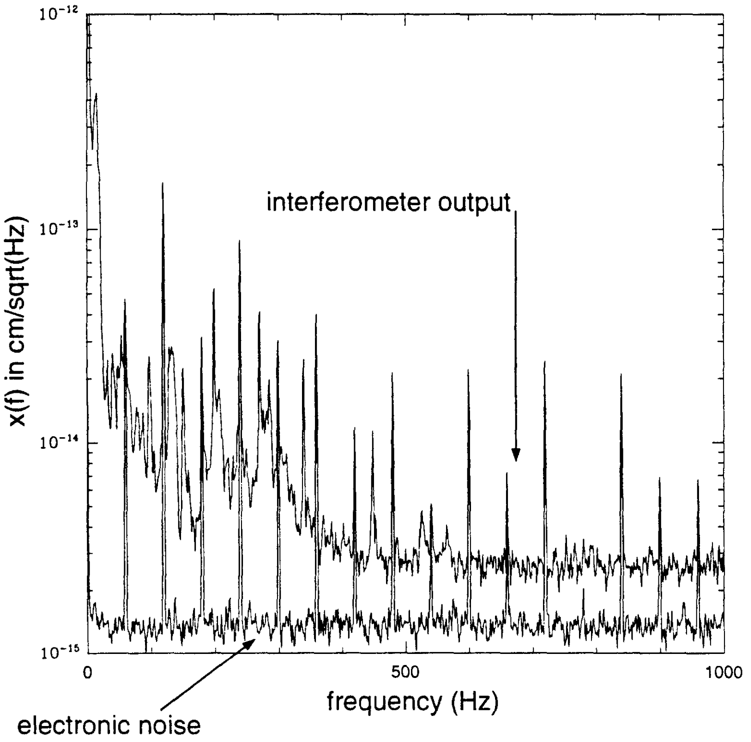

6.2 Amplitude Noise

The amplitude noise of the MISER is dominated by a relaxation oscillation at 282 kHz and reaches the shot noise limit at 30 MHz at 40 mW of output power. In this experiment, there was no attempt to stabilize the amplitude of the MISER. The light was phase modulated at 7.51 MHz where the amplitude noise of the MISER which is only 1.1 times as large as the shot noise limit is further filtered by the 80 kHz bandwidth of the Fabry-Perot cavities.

The contribution of amplitude noise to the output signal can easily be obtained by looking at both the dark and the bright fringe output. If the signal is spectrum is dominated by amplitude noise, then the ratio of the noise in the bright fringe to the noise in the dark fringe will scale as the ratio of the DC intensity in the bright fringe to the DC intensity in the dark fringe. If the signal is dominated by shot noise, then the ratio of the noise in the bright fringe to the noise in the dark fringe will scale as the square root of the ratio of the DC intensity in the bright fringe to the DC intensity in the dark fringe. It is clear from figure 6.2.1 that neither amplitude nor shot noise come close to accounting for the noise spectrum in the dark fringe.

Figure 6.2.1 The output spectrum for both the dark and the bright fringe is plotted. The contrast was 0.90. The amount of noise on the dark fringe is plotted assuming the bright fringe is either shot noise (the ratio of the noise in the bright fringe to the dark fringe is the square root of the ratio of the intensity) or amplitude noise limited (the ratio of the noise in the bright fringe to the dark fringe is linear in the intensity).

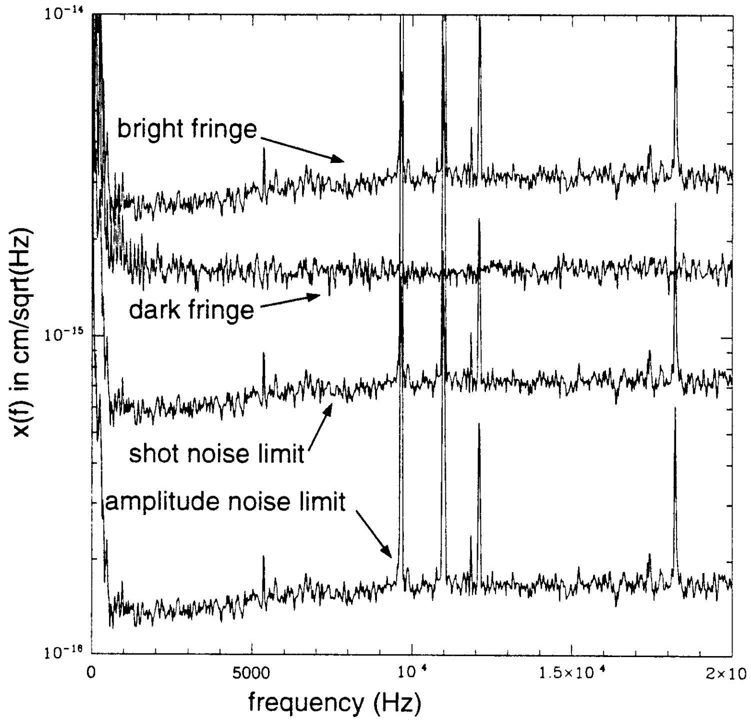

6.3 Residual Frequency Noise

The dependence of the output noise on residual frequency noise is discussed in detail in section 4.8. A great deal of effort was placed into understanding and solving this problem. Figure 6.3.1 shows the transmission of frequency noise through the interferometer as function of the offset from resonance of one cavity with respect to the other. It is clear that the frequency noise transmitted through the interferometer can be reduced arbitrarily with adequate tuning.

Figure 6.3.1 A plot of the frequency noise transmitted through the interferometer vs. the offset from resonance of one cavity. 0 on the x axis corresponds to the cavity on resonance. The FWHM of the cavity is 83 kHz.

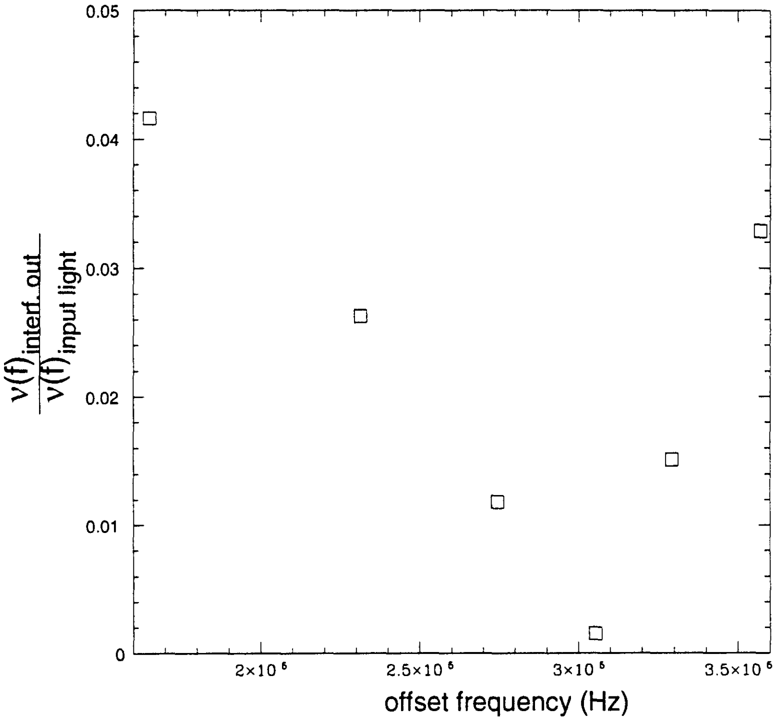

Figure 6.3.2 shows the noise spectrum of the reflection lock signal. Since the unity gain point of the frequency servo is at 2.0 kHz, the spectrum from the cavity locked on resonance is clearly dominated by the frequency noise of the MISER. The linear frequency scale obscures the $1/\sqrt{f}$ ($\delta\nu^2(f) \propto 1/f$) spectrum of the MISER frequency noise.

Figure 6.3.2 The noise spectrum of the reflection lock signal on the frequency of the MISER. The frequency noise spectrum comes directly from the error signal when the cavity is locked on resonance. The amplitude spectrum comes from measuring the noise spectrum of the reflection lock signal with the cavity off-resonance and the same DC intensity on the photodetector as the cavity on resonance. The electronic noise is the noise spectrum obtained when the photodetector is covered.

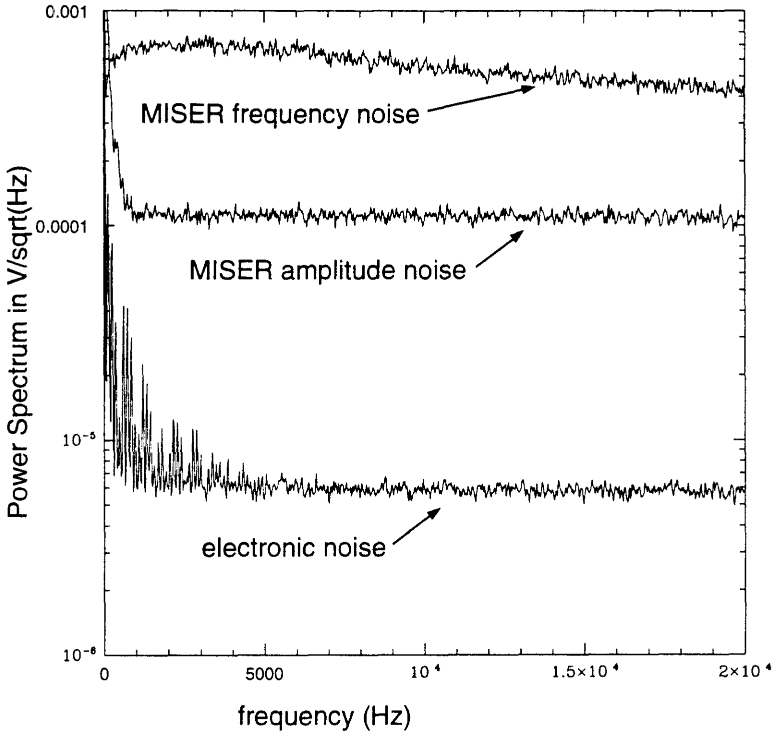

Figure 6.3.3 is the residual amount of frequency noise from the MISER that is transmitted through the interferometer. It is obtained by driving the MISER PZT input with broadband white noise. This impresses extra frequency noise on the MISER. The background noise is subtracted from this extra noisy signal (in quadrature). The ratio of the amount of signal transmitted through the interferometer over the amount seen in the reflected signal gives frequency noise rejection of the interferometer. This is then multiplied by the reflection lock signal which is the frequency noise of the MISER. The result is the amount of MISER frequency noise that is transmitted by the interferometer. The linearity of this technique was verified by changing the drive level of the broadband white noise.

$$residual\ noise = (refl.\ out) \times \sqrt{\frac{(interfer.\ out + freq.\ noise)^2 - (interfer.\ out)^2}{(refl.\ out + freq.\ noise)^2 - (refl.\ out)^2}} \tag{6.3.1}$$

The frequency noise rejection is good down to a few hundred Hertz.

Figure 6.3.3 The noise spectrum from both reflected signals is plotted. They are dominated by frequency noise in the MISER. The bottom curve shows the residual amount of frequency noise from the MISER that is transmitted through the interferometer. The boxes represent the residual noise using the reflection signal from the thermal loop which is disconnected at this point. It is essentially the same as the residual noise obtained from the MISER reflection frequency lock signal.

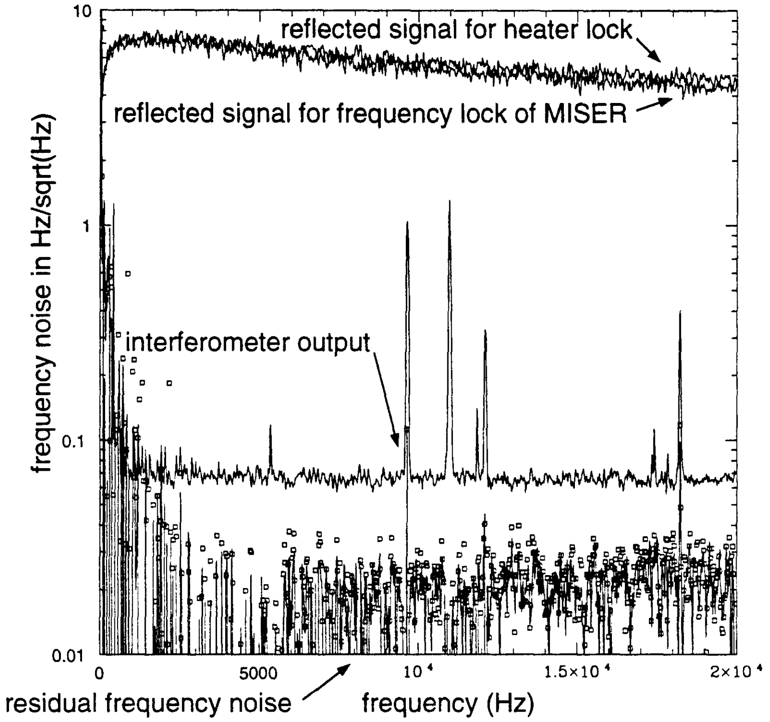

6.4 Input Beam Jitter Noise

Input beam jitter causes the effective cavity length to change and hence, looks like a noise term that is indistinguishable from the MISER frequency noise or plate displacement noise. Any beam jitter noise would be coloured by the various mechanical resonances in the various support structures. The noise spectrum below 1 kHz does have this characteristic. Above 1 kHz, however, the noise does appear quite broadband which makes it unlikely that input beam jitter is the cause of the background noise.

One way to place a limit on this noise term is to assume that the noise in the reflection lock signal is dominated by beam jitter noise. From figure 6.3.2, the beam jitter noise is less than $3 \times 10^{-13} cm/\sqrt{Hz}$. The fraction of incident light power transmitted by the Fabry-Perot cavity is (see for example Rudiger [27])

$$\frac{T^2}{(L+T)^2} \frac{1}{1 + \frac{4(1-L-T)}{(L+T)^2} \sin^2 N\psi} \tag{6.4.1}$$

where

$$\begin{aligned}\psi &= N\left[\arctan\left(\frac{z_2}{z_0}\right) - \arctan\left(\frac{z_1}{z_0}\right)\right]\\ z_2 &= 8.89\,cm + \delta z,\ z_1 = 0,\ z_0 = \frac{\pi\omega_0^2 n}{\lambda} = 17\,cm\\ &= N\arctan\left(\frac{8.89\,cm + \delta z}{17}\right)\end{aligned} \tag{6.4.2}$$

δz is the displacement caused by the beam jitter and N is the sum of the mode indices *m,n*. For N=0 or the TEM_{00} mode, this is just the transmission of the cavity. For N=1 (TEM_{01}), the intensity is suppressed by a factor

$$\frac{1}{1+\frac{4(1-L-T)}{(L+T)^2}\sin^2\psi} \approx \frac{(L+T)^2}{4(1-L-T)}(4.76 + .86\delta z) \tag{6.4.3}$$

with respect to the TEM_{00} mode.

If T=22 ppm. and L=106 ppm., the beam jitter in terms of a displacement noise will be suppressed by a factor of 3×10^8 on the cavity output with respect to the cavity input. The amount of beam jitter contribution to the interferometer output noise then can be no greater than

$$\begin{aligned}beam\ \ jitter\,noise &< 3 \times 10^{-13} cm/\sqrt{Hz}/3 \times 10^8\\ &< 1 \times 10^{-21} cm/\sqrt{Hz}\end{aligned} \tag{6.4.4}$$

6.5 Pockels Cell Phase Noise

Another possibility for the background noise spectrum is phase noise introduced by the output Pockels cells. If the electro-optic medium adds extra phase or amplitude noise to the light, then it will appear as an additional noise that is indistinguishable from displacement noise of the plate. It can be measured by looking at the output noise of the interferometer with the jewel removed. If the phase noise is coming after the Fabry-Perot cavities, then phase gain of the cavities is not contributing to the noise. Figure 6.5.1 shows such a measurement.

Figure 6.5.1 Noise spectrum with Fabry-Perot cavities and noise spectrum of simple Mach-Zender interferometer assuming noise is phase noise from the Pockels cells.

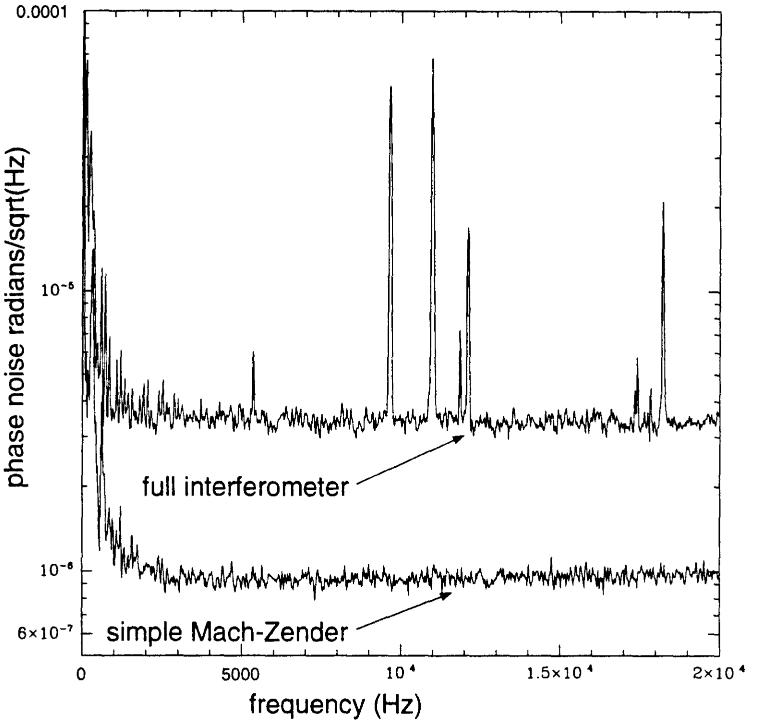

The jewel was removed and the beams realigned slightly to produce a suitable contrast. A spectrum of the dark fringe output was obtained. It was then calibrated in terms of phase by measuring the DC response of interferometer output signal to a known voltage, hence phase, applied to the Pockels cells.

The Pockels cells are clearly not introducing a phase noise that accounts for the background noise spectrum. It is important to note that the noise of the simple Mach-Zender interferometer is not limited by Pockels cell phase noise, but rather MISER amplitude noise and detector noise. The curve in figure 6.5.1 therefore only sets an upper limit on the phase noise of the Pockels cell.

6.6 Scattered Light Noise

Scattered light can introduce an effective phase noise. The scattered light must be examined in two different places: outside and inside the cavities.

There are two ways light scattered outside the cavity can produce extra phase noise. Light can scatter after the phase modulation and it will be seen in the demodulated signal. The previous section on Pockels cell phase noise eliminates this as a significant noise source since this noise would be the same irrespective of whether the cavities are present.

Another possible source of scattered light phase noise is light scattering outside the modulation recombining with the beam. If this light has a delay with respect to the main beam that its recombines with, there will be some phase noise

$$\varphi^2(f) = \alpha \times \left[\frac{2\pi\delta\nu(f)}{c}(l_2 - l_1)\right]^2 \tag{6.6.1}$$

where α is the overlap between the scattered beam and main beam (it has the form of the integral in equation 6.6.3), $\delta\nu(f)$ is the frequency noise and $l_2 - l_1$ is the path difference between the scattered beam and the main beam. The largest distance the beams will travel will be on the order of 1 metre. Using a frequency noise of $10Hz/\sqrt{Hz}$ gives a phase noise of $2 \times 10^{-7} rad/\sqrt{Hz} \times \sqrt{\alpha}$. Since the scattered light beam will have an intensity that is much less than the main beam, $\sqrt{\alpha} << 1$ and $\varphi(f) << 2 \times 10^{-7} rad/\sqrt{Hz}$. The measured phase noise is $4 \times 10^{-6} rad/\sqrt{Hz}$ (see figure 6.5.1). It is safe to assume that light scattering outside the cavities is not an important noise source.

Another possible instrument noise source is light scattering from one Fabry-Perot cavity into the other cavity. This is a more significant problem because the scattered light gets amplified by the finesse of the cavities. Since the losses on the mirrors are about 100 ppm., it sets an upper limit for the total amount of light that is scattered. If the light scatters isotropically at site A (see figure 6.6.1), then only the light that falls onto an area within the beam spot at scatter site B is important. This gives the power of the scattered light as

$$\begin{aligned} scattered\, power &= \frac{r_{beam}^2}{(9.69)^2/2} \times 100ppm \\ &= 1 \times 10^{-9} \end{aligned} \tag{6.6.2}$$

The amount of light that is initially scattered can be no greater than this. This scattered light must then be scattered back into the main beam at B. A first order assumption would be to allow all of the light scattered at B back into the main beam. The phase from this scatter will be

$$\begin{aligned} \varphi^2(f) = &\int_{paths} [I_{recomb}]\left[\frac{\partial P_{scat}(\theta)}{\partial\Omega}\right]\frac{d\Omega dA}{I_{main\, beam}} \\ &\times \left(\frac{2\pi x_{scat}(f)}{\lambda}\right)^2 \times \left(\frac{1}{1-R}\right)^2 \\ &= \sqrt{1 \times 10^{-9}}(5.9 \times 10^4)^2 \times (7.8 \times 10^3)^2 x_{scat}^2(f) \end{aligned} \tag{6.6.3}$$

In this case the overlap integral between the scattered beam and the main beam was done by equating it to the amount of electric field scattered onto the beam waist at B multiplied by the main beam electric field. This sets

$$\varphi(f) = 2.6 \times 10^6 x_{scatt}(f) \tag{6.6.4}$$

Figure 6.6.1 Sketch of scattering path

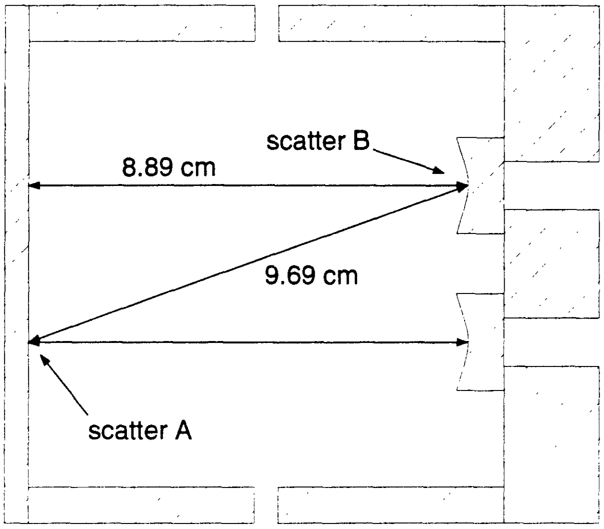

Using a phase noise of $4 \times 10^{-6} rad/\sqrt{Hz}$ from figure 6.5.1 sets

$$x_{scatt}(f) = 1 \times 10^{-12} cm/\sqrt{Hz} \qquad (6.6.5)$$

It is unlikely that there is anything in the jewel that is moving with a white spectrum at that amplitude. The ground noise has a $1/f^2$ displacement spectrum so it cannot be responsible for a spectrum that is flat from 500 Hz to 30 kHz. An even simpler argument is that the scattering surface is assumed to be one of the small mirrors whose displacement is limited by what was actually measured $\left(2 \times 10^{-15} cm/\sqrt{Hz}\right)$. The phase noise contribution from scattered light inside the interferometer then is not responsible for the background noise spectrum.

Chapter 7 Mechanical Noise Other than Plate Thermal Noise

7.1 Thermal Noise from Other Normal Modes

Since many different modes were seen, there is a possibility that they all add up to produce a background much higher than that expected from a single mode. The simplest model for the thermal noise from a mode can be obtained from equation 1.4.12. The first assumption is that the mass of the oscillator is simply that of the plate or 113g. This gives an overestimate of the thermal noise that is measured for each mode since a proper calculation must take the geometry of the plate into account (see section 3.4). The other assumption is that all of the measured resonant frequencies are from the thin plate. This is not true because some of the resonances are from the thick plate or the cylinder. Since both the cylinder and the thick plate have a higher mass than the thin plate, this assumption again tends to overestimate the thermal noise. Finally, the thermal noise from all of these resonant frequencies and their measured Q's are added in quadrature. This is another overestimate because most of these resonant frequencies do not show up in the actual measured noise spectrum; they can only be seen when the jewel is driven electrostatically. Figure 7.1.1 shows the result of this calculation. The measured background noise spectrum is still a factor of 10 too large.

Figure 7.1.1 Plot of the measured noise spectrum and a simple theoretical model of the thermal noise from all of the frequencies and the Q's measured

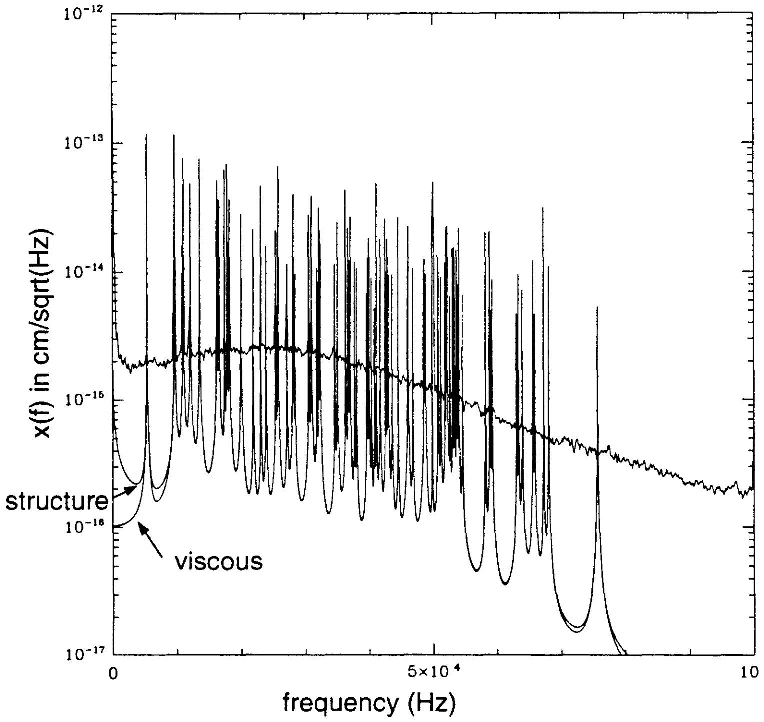

A more complete addition of the noise from higher order modes must take into account all of the modes until the beam spot size is the same as the distance between the nodes in a mode. This assumption is valid because the phase of the beam averages to zero when the beam size contains many different oscillations of the surface inside its diameter. One way to model this effect is to give the surface the following equation to describes its motions

$$z = \sum_{l,m} u_{lm} \cos\left(\frac{x}{a_l}\right) \cos\left(\frac{y}{b_m}\right) \sin\left(\omega_{lm} t\right) \tag{7.1.1}$$

where u_{lm} is the amplitude and a_l, b_m are $2\pi \times \lambda$ of the surface wave. The electric field at the surface will then be (assuming the beam is at its waist)

$$\varepsilon(x,y) = \varepsilon_0 \times \exp\left[-ikz - \frac{(x^2+y2)}{w_0^2}\right] \tag{7.1.2}$$

In most thermal noise applications, the amplitude of the surface motion is very small. In this experiment, the largest motion less than $10^{-12} cm$. Since the light wavelength used in this experiment is 1.06 μm, the phase change in the light will be very small (less than 10^{-7}). The oscillatory part of the electric field can then be expanded.

$$\begin{aligned}
e^{ikz} &= \exp\left[ik \times \sum_{l,m} u_{lm} \cos\left(\frac{x}{a_l}\right) \cos\left(\frac{y}{b_l}\right) \sin\left(\omega_{lm} t\right)\right] \\
&= \prod_{l,m} \exp\left[ik \times u_{lm} \cos\left(\frac{x}{a_l}\right) \cos\left(\frac{y}{b_l}\right) \sin\left(\omega_{lm} t\right)\right] \\
&\approx \prod_{l,m} J_0\left(ik \times u_{lm} \cos\left(\frac{x}{a_l}\right) \cos\left(\frac{y}{b_l}\right)\right) \\
&+ 2J_1\left(ik \times u_{lm} \cos\left(\frac{x}{a_l}\right) \cos\left(\frac{y}{b_l}\right)\right) \sin\left(\omega_{lm} t\right) \\
&\approx \prod_{l,m} 1 + ik \times u_{lm} \cos\left(\frac{x}{a_l}\right) \cos\left(\frac{y}{b_l}\right) \sin\left(\omega_{lm} t\right) \\
&\approx 1 + ik \times \sum_{l,m} u_{lm} \cos\left(\frac{x}{a_l}\right) \cos\left(\frac{y}{b_l}\right) \sin\left(\omega_{lm} t\right)
\end{aligned} \tag{7.1.3}$$

This must be weighted against the TEM$_{00}$ gaussian beam shape to obtain the electric field of the entire beam

$$\begin{aligned}
\varepsilon = \varepsilon_0 \times \int_{-\infty}^{+\infty}\int_{-\infty}^{+\infty} &\left(1 + ik \times \sum_{l,m} u_{lm} \cos\left(\frac{x}{a_l}\right) \cos\left(\frac{y}{b_l}\right)\right) \sin\left(\omega_{lm} t\right) \\
\times \exp&\left[\frac{-(x^2+y^2)}{\omega_0^2}\right] dx dy \\
= \pi\omega_0^2\varepsilon_0 &\left[1 + ik \times \sum_{l,m} u_{lm} \sin\left(\omega_{lm} t\right) \exp\left[\frac{-\omega_0^2}{4a_l^2}\right] \exp\left[\frac{-\omega_0^2}{4b_m^2}\right]\right]
\end{aligned} \tag{7.1.4}$$

This expression shows that for $a_l, b_l >> w_0$ the amount of phase added to the field is iku_{lm} or the amount of phase that light travelling a distance equal to the amplitude of the surface wave would accumulate. For $a_l, b_l << w_0$ there is no phase added to the electric field.

Since the plate diameter is 12.065 cm and the beam diameter is 0.048 cm, all modes up to those that have at least 251 nodal lines must be included. One way to place an upper bound on the sum of the thermal noise from all of the higher order modes is to look at the off resonance noise from a higher order mode and then scale it with the resonant frequencies of even higher order modes. The thermal noise peak for a 40 kHz mode $(n = 2, k = 0, \lambda_{20} = 9.4)$ with a Q greater than 10^4 is only a factor of 2 above the background noise of $2 \times 10^{-15} cm/\sqrt{Hz}$ (see figure 7.1.2). This means that the off-resonance noise for this particular mode will be less than $4 \times 10^{-19} cm/\sqrt{Hz}$.

Figure 7.1.2 A plot of the displacement noise between 40 kHz and 60 kHz. The y-axis has a linear scale to show the various resonance peaks. The signal at 50 kHz comes from the FM on the MISER that controls the frequency noise minimization servo. The largest resonant peak is a factor of 2 above the noise (when it is resolved).

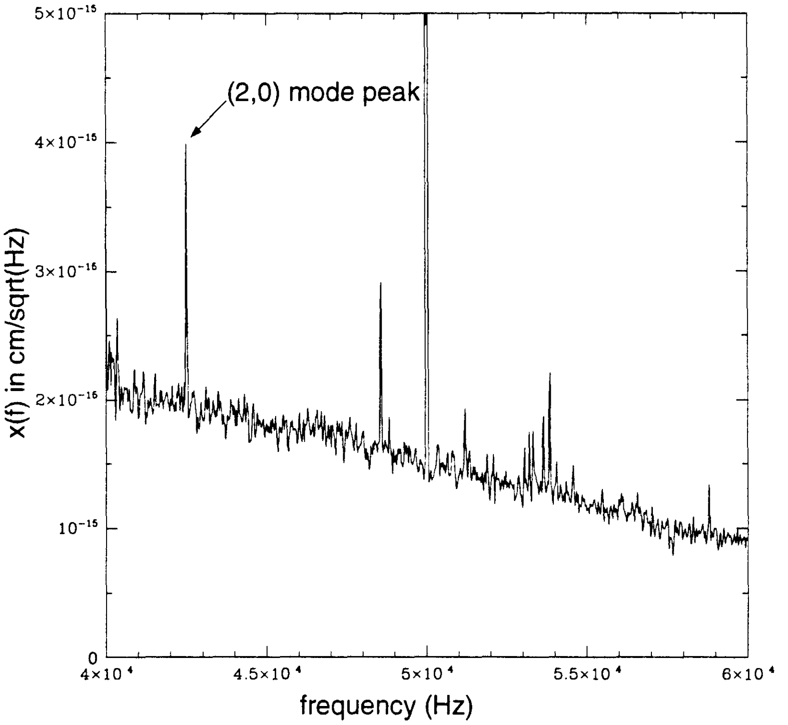

For a viscous damping model and $\omega << \omega_0$,

$$
\begin{aligned}
x^2(\omega) &\propto \frac{1}{f_{nk}^3 Q} \\
&\propto \frac{1}{(\lambda_{nk})^6 Q}
\end{aligned}
\qquad (7.1.5)
$$

and λ has an asymptotic value of $3n$ where n is the number of radial nodes. When making the sum for the thermal noise from all the modes, a multiplicity of n must be included for each mode since there are both radial and circumferential nodes. It is also worthwhile to include another factor of n to take into account any splitting of the modes. Finally, the density of states for the number of modes at a given n cannot grow faster than n^2. This gives a sum

$$\begin{aligned} x^2(f) &= \sum_{k=3}^{252} \frac{1}{(3n)^6}(3 \times 3)^6 \times n^4 \times 1.6 \times 10^{-37} cm/\sqrt{Hz} \\ &= 1.2 \times 10^{-34} \sum_{k=3}^{252} \frac{1}{n^2} \end{aligned} \tag{7.1.6}$$

The sum is less than 1, even if the sum is extended to include an infinite number of terms. The addition of thermal noise from higher order modes then is less than $1 \times 10^{-17} cm/\sqrt{Hz}$ and is not a likely explanation for the background noise.

Another approach to include the thermal noise from higher order modes is to use the Debye model to obtain a density of states for the number of modes at a given frequency. For a sound wave with wave vector κ and angular frequency $\omega = c_s \kappa$ where c_s is the effective sound velocity, The number of wave modes with a frequency between ω and $\omega + d\omega$, is (see for example Reif [7])

$$\sigma_c(\omega) d\omega = 3\frac{V}{2\pi c_s^2}\omega^2 d\omega \tag{7.1.7}$$

where V is the volume. The total thermal noise form all the modes between ω_1 and ω_D is

$$\begin{aligned} x^2(\omega) &= \int_{\omega_1}^{\omega_D} \frac{4k_B T}{m\omega^3 Q} \times \frac{3V}{2\pi^2 c_s^3} w^2 dw \\ &= \frac{6k_B T V}{\pi m c_s^3 Q} \ln\left(\frac{\omega_D}{\omega_1}\right) \\ &= \frac{6k_B T \times 73cm^3}{\pi \times 160g \times (5 \times 10^5 cm/sec)^3 10^4} \ln\left(\frac{\omega_D}{\omega_1}\right) \\ &= 3 \times 10^{-35} cm^2/Hz \ln\left(\frac{\omega_D}{\omega_1}\right) \end{aligned} \tag{7.1.8}$$

ω_D is the Debye frequency

$$\begin{aligned} \omega_D &= c_s\left(6\pi^2\frac{N}{V}\right)^{\frac{1}{3}} \\ &= 5 \times 10^5 cm/sec(6\pi^2 \times 2 \times 10^{22} cm^{-3})^{\frac{1}{3}} \\ &= 10^{14} sec^{-1} \end{aligned} \tag{7.1.9}$$

Using a value for $\omega_1 = 2\pi \times 1kHz$ gives

$$\ln\left(\frac{\omega_D}{\omega_1}\right) = 23 \tag{7.1.10}$$

and the noise is $x(f) = 3 \times 10^{-17} cm/Hz$. A better integration has to include the phase averaged over the beam size as shown in equation 7. Assuming the wavelength scale is

$$a = b = \frac{\lambda}{2\pi} = \frac{c_s}{2\pi\nu} = \frac{c_s}{\omega} \tag{7.1.11}$$

gives a thermal noise of

$$\begin{aligned} x^2(\omega) &= \int_{\omega_1}^{\omega_D} \frac{4k_BT}{m\omega^3 Q} \times \frac{3V}{2\pi^2 c_s^3} w^2 \exp\left[-\frac{w^2_{o(beam)}\omega^2}{2c_s^2}\right] dw \\ &= \frac{6k_BTV}{\pi m c_s^3 Q} \int_{\omega_1}^{\omega_D} \frac{1}{\omega} \exp\left[-\frac{w^2_{o(beam)}\omega^2}{2c_s^2}\right] dw \\ &= \frac{6k_BTV}{\pi m c_s^3 Q} \times 7.8 \\ &= 2 \times 10^{-34} cm^2/Hz \end{aligned} \tag{7.1.12}$$

The noise in this case will be $x(f) = 2 \times 10^{-17} cm/Hz$. The noise background cannot then be explained by using a Debye distribution for the acoustic modes.

Another source of broadband noise could be the low frequency tail of a mode from some other part of the jewel that has a resonant frequency much greater than 100 kHz. For a viscous damping model, the thermally driven displacement noise is

$$\begin{aligned} x^2(\omega) &= \frac{4k_BT}{m\omega_0^3 Q} \\ &= \frac{4.2 \times 10^{-18}}{m f_0^3 Q} \, cm^2/Hz \end{aligned} \tag{7.1.13}$$

for $\omega << \omega_0$. Since the background noise is flat and has a magnitude of $2 \times 10^{-15} cm/\sqrt{Hz}$, the product of mass, resonant frequency and Q must be

$$m \times f_0^3 \times Q = 1.7 \times 10^{14} \, gHz^3 \tag{7.1.14}$$

The small, curved mirror that is optically contacted to the thick plate has a mass of 14 g and should have resonant frequencies in the hundreds of kHz range. This suggests that the Q of this resonance would have to be on the order of 10^{-2}. While the measured Q's of the thin plate, cylinder and thick plate were low ($10^3 - 10^5$ rather than 10^6) , a Q of 10^{-2} for the 1″ mirror seems too small to be an acceptable explanation for the noise that is measured. If one makes a model for the optical contact as a material that has a spring constant and a large loss, one could possibly find a resonant frequency of a simple mass with a spring attached to it that is much lower than the resonant frequency of an internal mode of the small mirror and that has a much lower Q than the internal mode. This is discussed in the optical contacting noise section.

7.2 Optical Contacting Noise

The source of the noise could be related to the fact that all of the Q's are at least an order of magnitude too low for what one would normally expect from fused quartz. There are two likely explanations for the low Q's: the multi-layer dielectric coating or the optical contacting.

One way to understand whether the coating degrades the Q is to compare the Q's of the uncoated thicker plate to that of the coated thin plate in the jewel. Since the frequency of a plate's normal mode is proportional to its thickness, the normal modes of the thick plate should have resonant frequencies with resonant frequencies about 4 times those of the thin plate. There are measured resonant frequencies that match this pattern, but their Q's are within the same range as those from the thin plate. The coating then is not responsible for the low Q's.

Since the jewel was disassembled, it is clear that the optical contact is not the equivalent of the whole assembly being fused together. The resonant frequencies changed by only a few per cent before and after the jewel was taken apart. The Q's remained the same. It is very likely that this "lossy" clamp is responsible for the degradation of the Q. The optical contacting force can then be viewed as a new driving term for the various normal modes of the entire jewel. For example, the two small spherical mirrors could have some displacement noise from their contact to the thick plate.

One way to model the optical contact is to give it the properties of a material with a certain spring constant and loss (see figure 7.2.1). By comparing the energy stored in the plate with that stored in this spring clamp, an estimate of the damping is obtained. The amount of energy stored in the plate is (see for example [18])

$$\begin{gathered} Energy = \frac{Eh^3}{24(1-\sigma^2)} \int_{area} \left(\frac{\partial^2 Z}{\partial x^2} + \frac{\partial^2 Z}{\partial y^2} \right)^2 + \\ 2(1-\sigma) \left[\left(\frac{\partial^2 Z}{\partial x \partial y} \right)^2 - \frac{\partial^2 Z}{\partial x^2} \frac{\partial^2 Z}{\partial y^2} \right] dA \end{gathered} \tag{7.2.1}$$

The energy stored in the spring clamp is

$$Energy = \frac{1}{2} Y \int_{area\ of\ contact} Z^2 dA \tag{7.2.2}$$

where Y is the spring constant per unit area. The shape of $n = 0$, $k = 1$ mode for a disk with a 6.0325 cm radius is

$$Z(r, \theta) = [J_1(0.764r) + 0.015 I_1(.0764r)] \cos\theta \tag{7.2.3}$$

Doing the integrals gives

$$\begin{aligned} E_{plate} &= 2.1 \times 10^{10} \times 2.621 \\ E_{clamp} &= .022 \times Y \end{aligned} \tag{7.2.4}$$

If the optical contact has a loss $\phi_{clamp}(\omega)$ and it is the dominant loss mechanism of this normal mode, it will be related to the loss of the plate $\phi_{plate}(\omega) = (9000)^{-1}$ by

$$\begin{aligned}\phi_{clamp} &= \phi_{plate}\frac{E_{plate}}{E_{clamp}} \\ &= \frac{1}{9000}\frac{5.5\times 10^{10}}{0.22Y} \\ &= \frac{2.8\times 10^{7}}{Y}\end{aligned} \tag{7.2.5}$$

Since the noise spectrum is flat, the damping mechanism is most likely a viscous one. The loss must then be scaled in frequency

$$\phi_{clamp} = \frac{2.8\times 10^{7}}{Y}\left(\frac{9.76kHz}{f_0}\right) \tag{7.2.6}$$

Figure 7.2.1 Model of optical contact force.

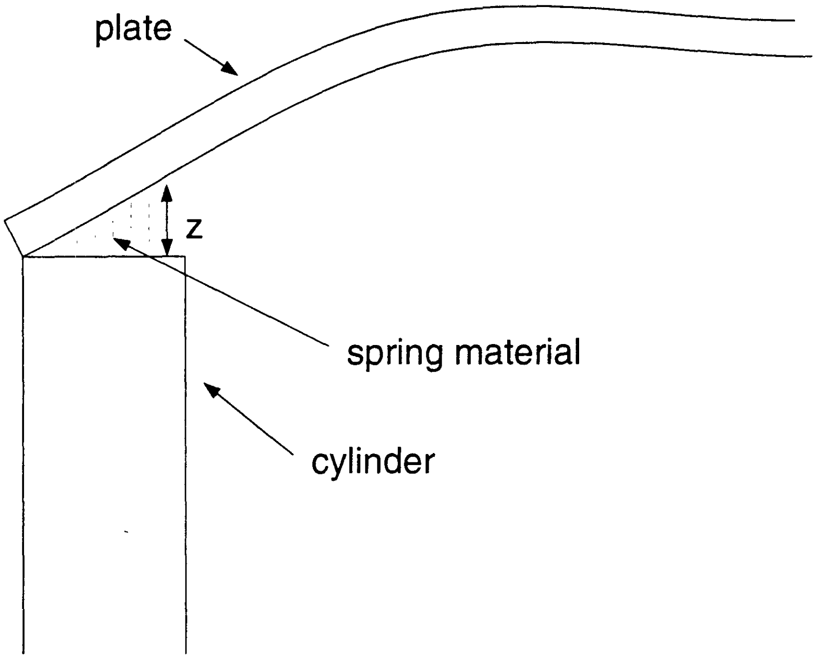

A first guess for the optical contact spring constant Y would be the Young's modulus of fused quartz divided by the separation between the two contacted pieces. The separation length is bounded by the surface figure error of the contacted pieces that is less than $\lambda = 6135\dot{A}/10$ and sets

$$Y > 1\times 10^{17}\frac{dynes/cm^2}{cm} \tag{7.2.7}$$

The area of the contact could be no greater than that from the difference between the outer and inner radius of the cylinder

$$\begin{aligned}area &= \pi(6.0325cm)^2 - \pi(5.08cm)^2 \\ &= 33.3\ cm^2\end{aligned} \tag{7.2.8}$$

The next step is to take this spring model and apply a mass to it that is equal to the plate mass (160g). This would show whether the measured noise spectrum was due to the optical contact loss thermally driving the plate. The resonant frequency of such a system is

$$\begin{aligned} f_0 &= \frac{1}{2\pi}\sqrt{\frac{Y \times area}{m}} \\ &= 23MHz \end{aligned} \tag{7.2.9}$$

Using viscous damping model with a loss as described by equation 7.2.6 gives an off-resonance noise spectrum for $f << f_0$

$$\begin{aligned} x^2(\omega) &= \frac{4k_BT\phi_{clamp}(\omega)}{m\omega_0^3} \\ &= \frac{4k_BT \times 2\pi \times m \times 2.8 \times 10^7 \times 9760}{Y^3 \times (contact\, area)^2} \\ x(\omega) &= 6 \times 10^{-27} cm/\sqrt{Hz} \end{aligned} \tag{7.2.10}$$

This is much smaller than the measured noise spectrum.

Alternatively, Y and the contact area can be equated to the measured spectrum

$$x^2(w) = 4 \times 10^{-30} cm^2/Hz = \frac{45}{area^2 \times Y^3} \tag{7.2.11}$$

Assuming $Y = 1 \times 10^{17} \frac{dynes/cm^2}{cm}$ produces a value for the contact area of $9 \times 10^{-11} cm^2$ which seems much too small given the upper limit for the contacted area of $33.3cm^2$. Assuming a contact area of $33.3cm^2$ gives a value for Y of $2.2 \times 10^9 \frac{dynes/cm^2}{cm}$. This implies a length scale for the optical contact separation of 330 cm. Again, this does not seem reasonable.

Another way to find consistency in this model is to equate the measured noise spectrum to optical contact spring driving the plate and assume this is the loss of the optical contact. Then, by using equation 7.2.5, the loss of the plate can be derived.

$$\begin{aligned} x^2(\omega) &= 4 \times 10^{-30} cm^2/\sqrt{Hz} \\ &= \frac{4k_BT}{m\omega_0^3}\phi_{plate}(\omega)\frac{E_{plate}}{E_{clamp}}\left(\frac{9.76kHz}{23MHz}\right) \\ &= \frac{4k_BT\sqrt{m}\,\phi_{plate} \times 2.8 \times 10^7 \times \left(4.2 \times 10^{-4}\right)}{Y^{\frac{5}{2}} \times (contact\, area)^{\frac{3}{2}}} \\ &= 4.1 \times 10^{-53}\phi_{plate} \\ Q_{plate} &= \left(\phi_{plate}\right)^{-1} = 1 \times 10^{-23} \end{aligned} \tag{7.2.12}$$

Once again, the answer is inconsistent and very unreasonable.

A better place to search for optical contacting noise is from the joint between the small mirrors and the thick plate. The thermally driven motions from the thin plate will primarily be a common mode displacement that is cancelled by the interferometry. On the other hand, the motion of one small mirror would be added incoherently with respect to the motion of the other. The mass of a small mirror is 14g and the contact area is $3.8cm^2$. Using the method in equation 7.2.10 to determine the off-resonance noise given the plate loss gives

$$\begin{aligned} f_0 &= \frac{1}{2\pi}\sqrt{\frac{Y \times area}{m}} \\ &= 26MHz \end{aligned} \tag{7.2.13}$$

$$\begin{aligned} x^2(\omega) &= \frac{4k_BT\phi_{clamp}(\omega)}{m\omega_0^3} \\ &= \frac{4k_BT \times 2\pi \times m \times 2.8 \times 10^7 \times 9760}{Y^3 \times (contact\ area)^2} \\ x(\omega) &= 1.7 \times 10^{-26} cm/\sqrt{Hz} \end{aligned} \tag{7.2.14}$$

This number is much too small. Doing the reverse process as in equation 7.2.12 gives

$$\begin{aligned} x^2(\omega) &= 4 \times 10^{-30} cm^2/\sqrt{Hz} \\ &= \frac{4k_BT}{m\omega_0^3}\phi_{plate}(\omega)\frac{E_{plate}}{E_{clamp}}\left(\frac{9.76kHz}{26MHz}\right) \\ &= 2.8 \times 10^{-52}\phi_{plate} \\ Q_{plate} &= \left(\phi_{plate}\right)^{-1} = 7 \times 10^{-23} \end{aligned} \tag{7.2.15}$$

The answer is completely inconsistent.

There is another clue in the data that suggests an explanation for the measure noise spectrum. A close examination of the broadband noise shows that is grows slightly by a factor of 1.4 between 1 kHz and 25 kHz. This is much easier to see on a linear plot of the data with an expanded scale (see figure 7.2.2). Scaling the data from the simple Mach-Zender interferometer (without cavities) and superposing it on the full interferometer (with cavities) data shows that the Mach-Zender response is flat while the full interferometer has this bump in it. This bump is then probably a real measurement rather than some irregularity in the signal extraction. Above 50 kHz, the amplitude of the noise rolls off due to various filters from the Fabry-Perot cavity bandwidth and the electronics bandwidth. This broad peak could be due to a very low Q mode (on the order of one) with a resonant frequency of about 30 kHz. If one fits this data to a viscous damping model, the parameters obtained are

$$\begin{aligned} m &= 7.0g \\ f_0 &= 28.1kHz \\ Q &= 1.27 \end{aligned} \tag{7.2.16}$$

Surprisingly, the mass is almost exactly half that of one of the small mirrors (14g).

This result is only speculation. The data does not fit the curve for a resonance above the resonant frequency. Moreover, the calculation done in equation 7.2.14 shows that such a result is not consistent with the optical contact model.

There is another possible explanation for this low Q resonance and the measured noise spectrum. It could be due to some environmental noise source other than internal thermal noise such as acoustic noise driving a mode of the cylindrical part of the jewel. This mode could be highly damped by the viton pieces upon which the jewel sits. These modes, however, are clearly seen in the data and their Q's are between $5 \times 10^3 - 10^5$. This hypothesis then is not correct.

Figure 7.2.2 Plot of the broadband noise with a linear scale. The fitted curve is the thermal noise for a viscous damped harmonic oscillator with the parameters given in equation 7.2.16.

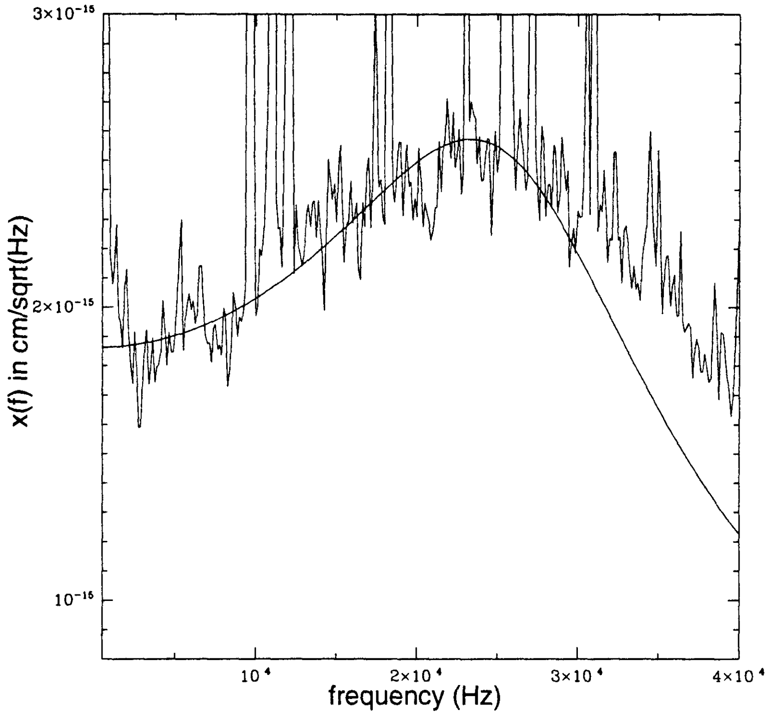

7.3 Experimental Conclusions

This experiment has set an upper limit of $x(f) < 2 \times 10^{-15} cm/\sqrt{Hz}$ for the off-resonance thermal noise spectrum from a piece of fused quartz in the shape of a thin disk. It has demonstrated the use of resonant Fabry-Perot cavities to increase the phase changes of light due to small motions of the cavity end mirrors. It has also shown an interferometric technique to reduce the transmission of common mode noise, especially the frequency noise of a laser, through a Mach-Zender interferometer.

This experiment has successfully measured a noise displacement spectrum on the order of $10^{-15} cm/\sqrt{Hz}$. As a relatively small, table top set up, it has achieved a sensitivity comparable to that of early gravity wave detector prototypes which are larger, more complicated and more expensive experiments. Since thermal noise will be an important noise source in advanced gravity wave detectors, new experiments must be undertaken to gain a better understanding of when the thermal noise limit will be reached.

The techniques developed in this thesis offer a way to measure thermal noise with the same sensitivity as a full scale gravity wave detector. A particularly interesting application of this type of measurement is the direct monitoring of thermal noise in a mirror substrate in order to remove it from a gravity wave detector output signal. This could possibly serve as means to avoid the thermal noise limit and is discussed in chapter 10.

Chapter 8 Future Experiments

8.1 Other Experiments Using the Current Design

While the experiment performed in this thesis did not seem limited by instrument noise, the desired experimental sensitivity of $10^{-17} cm/\sqrt{Hz}$ was not attained. This happened because the mirrors became contaminated over time which reduced the output intensity of the Fabry-Perot cavities and hence, the signal gain of the interferometer. One interesting goal for a further experiment would be to clean the mirrors and try to achieve a better experimental sensitivity. At this point, a few holes could be drilled into the side of the cylinder. This would allow easy access to the mirrors if any further cleaning were needed in the future.

While the jewel is disassembled, the mechanical Q's of its various components could be measured. This would determine whether the optical contacts are responsible for the relatively low Q's that were measured for the fused quartz in this experiment. The Q measurement could be performed on the separate pieces with an optical detection scheme such as an optical lever.

One way to study the Q would be to add extra damping to the jewel. Epoxy could be placed on the plate to compromise its Q. In fact, epoxy could be used to glue the jewel together. It would be interesting to measure the off-resonance thermal noise as a function of the Q. Since the thermal noise resonant peak is $x(\omega_0) \propto \sqrt{Q}$ and the off-resonance noise is $x(\omega << \omega_0) \propto 1/\sqrt{Q}$, the thermal noise peak will decrease while the off-resonance noise will increase as the Q becomes smaller. In figure 5.3.5, the thermal noise resonant peak has a value of $3 \times 10^{-13} cm/\sqrt{Hz}$ and a Q of 6500. If the Q is reduced to less than 10, then the off-resonance thermal noise might be greater than the background noise of $2 \times 10^{-15} cm/\sqrt{Hz}$. While ruining the Q of fused quartz does not offer any insight to the inherent loss mechanisms of fused quartz, it does give some understanding of how adding components to a piece of fused quartz affects its Q.

8.2 Experiments to Understand Thermal Noise

There are many other ways to design an experiment that uses interferometry to measure the off-resonance thermal noise displacement spectrum of a mechanical object. One of the goals of this experiment was to take advantage of the inherent common mode rejection of an interferometer. Unfortunately, the assembly that held the phase sensitive parts of the experiment together was a fairly complicated mechanical system with many resonances and with clamping conditions (from the optical contacts) that were not understood very well. A future experiment should reduce the complexity of the mechanical system to be measured. An important part of the new design would include a clamp that does not reduce the Q of the material and that does not couple more environmental noise into the system.

There are essentially two ways to build such an experiment. Both techniques involve hanging the mirrors that form the resonant cavities. The difference between the two techniques involves whether the cavity is external to the mirror substrate or internal to the mirror substrate.

If the cavity is external to the mirror substrate, the experiment is almost the same as the one performed in this thesis except that all the mirrors are hung rather than optically contacted to a bigger assembly (see figure 8.2.1). The servo schemes will also be somewhat different. Since the length of each cavity can be controlled separately, there is no longer a need for the thermal length control. There is a new complexity to the entire servo control system since there will be a substantial motion of the mirrors at low frequencies from the ground motion.

The advantage of this system is that there no longer are any optical contacts. One disadvantage is an added set of mechanical resonances from the suspension wires. Another potential problem is the type of actuator used to control the cavity lengths. While the frequency of the laser is locked to one cavity, the other one needs an actuator to control its length. This could be done with an electrostatic plate that would act upon the thick mirror.

Figure 8.2.1 Top view of a hanging experiment design with external cavities. All the mirrors are suspended as pendula.

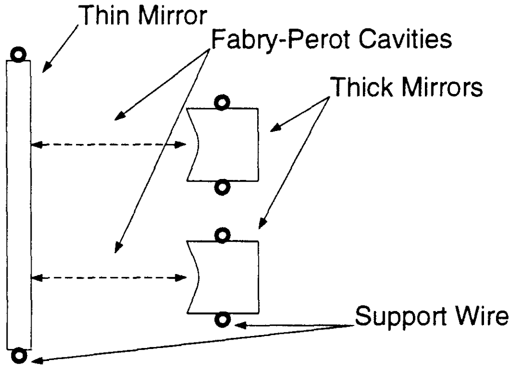

Another way to do this experiment is to put the Fabry-Perot cavities inside the mirror substrates themselves (see figure 8.2.2). This technique can achieve high sensitivities (see chapter 10). The servo system is similar to the one used in the experiment performed in this thesis. The frequency of the laser can be tuned to the length of one cavity while the other cavity is thermally tuned so that it is also resonant with the laser frequency. If both mirrors are the same size with the same mechanical Q, then the thermal noise from each cavity should add in quadrature. Again, there is no added complexity of an optical contact or an added mechanical system.

Unfortunately, as discussed in section 3.2, it is difficult to design a monolithic mass that has a resonant frequency between 1 and 10 kHz and that has a large off-resonance thermal noise spectrum. Also, since the centre of the mirror is being sampled, many normal modes will contribute to the displacement that is measured. If the experiment does achieve a very high sensitivity through the use of very low loss substrates and coatings, a measurement of the actual thermal noise spectrum from a LIGO type mirror might be possible.

The problem with this design is that it assumes that the thermal noise in both mirrors is the same. Since the noise in each mirror is not correlated, the measured noise should be the quadrature sum of the noise in each mirror. There is no way to independently measure the noise of each mirror.

Figure 8.2.2 Top view of a hanging experiment design with internal cavities.

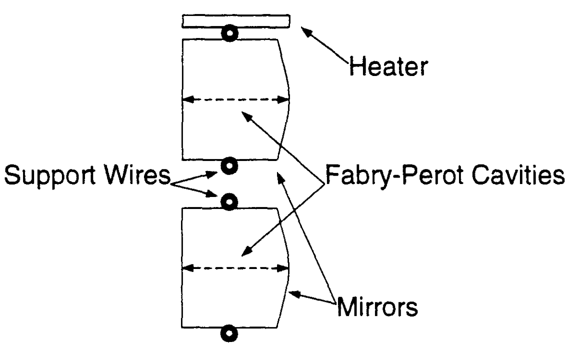

8.3 Experiments to Understand Optical Contacting Noise

Optical contacting is a convenient way to assemble fused quartz pieces. It is important to rule out optical contacting noise as the source of the measured noise in this experiment if optical contacting is to be used as an assembly technique in high sensitivity measurements like gravity wave detection.

The first task would involve measuring the mechanical Q's of the various components of the jewel before and after contacting as described in section 8.1.

The next part of the investigation would be somewhat more difficult. An experiment similar to that described in figure 8.2.1 would be set up except that another thick mirror would be made (see figure 8.3.1). It would consist of two pieces of fused quartz that are optically contacted together. One of the pieces would be a coated mirror. The other would have a hole in its centre. The assembled piece would have the same dimensions and mass as the regular thick mirror. This compound mirror should have the same thermal noise as the regular mirror. If the measured thermal noise spectrum was excessive when the compound mirror replaces the regular mirror, the optical contact would be a very likely source for that excess noise.

Figure 8.3.1 Sketch of an experiment to measure optical contacting noise.

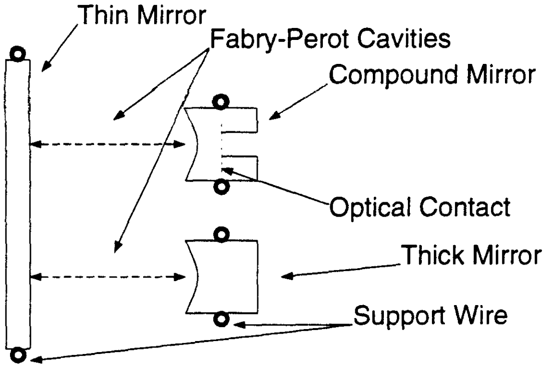

Chapter 9 Microscopic Model for Understanding Thermal Noise in a Bulk Piece of Fused Quartz

9.1 Theory

The most basic aspect of this model is the assumption that the loss mechanism in fused quartz comes from a point like defect in the material. This defect can be an impurity or any other kind of non-uniformity in the material (see for example Braginsky [28]). These defects are driven by thermal energy to produce impulses that kick the various normal modes of the fused quartz. The two main assumptions are that these defects are randomly distributed about the material and that the time distribution of the impulses follow Poisson statistics.

9.2 Concept for Data Analysis

A simple implementation of this model in a thin disk of fused quartz looks at the effect of an impulse in two different normal modes. The first consideration is the response of a simple harmonic oscillator to an impulsive force of the form:

$$\begin{aligned} F(t) &= a_n,\ t_n - \frac{\tau}{2} < t < t_n + \frac{\tau}{2} \\ &= 0,\ otherwise \\ &\lim \tau \to 0,\ a_n\tau \to const. \end{aligned} \tag{9.2.1}$$

The oscillator will respond as follows:

$$\begin{aligned} \ddot{x} + \omega_0^2(1 + i\phi)x &= \frac{F(t)}{m} \\ x(t) &= \sum_n \frac{a_n}{m\omega_0} e^{-\frac{\phi}{2}\omega_0(t-t_n)} \sin\omega_0(t - t_n) \end{aligned} \tag{9.2.2}$$

The next step involves determining how to weight each pulse relative to each normal mode. The two lowest order normal modes have the form (see chapter 3)

$$\begin{aligned} J_0(k_0 r) + b_0 I_0(k_0 r),\ \omega = \omega_0 \\ [J_1(k_1 r) + b_1 I_1(k_1 r)]\cos\theta,\ \omega = \omega_1 \end{aligned} \tag{9.2.3}$$

The effective amplitude of the pulse is weighted according to its position in each normal mode. For example, if a pulse occurs at r=θ=0, then the pulse has a maximum amplitude for the first mode and zero amplitude for the second mode.

A simulation of this model was implemented by considering the first two normal modes of the plate at 5.26 kHz and 9.57 kHz. In each time interval Δt , there are four random variables that specify all the pulse parameters. The amplitude of each pulse is the same.

variable 1	decide if pulse occurs
variable 2	decide sign of pulse
variable 3	decide where on radius pulse occurs
variable 4	decide where on θ pulse occurs

Figures 9.2.1 and 9.2.2 show the simulation result for both the amplitude and phase of the 5.26 kHz mode as a function of time. Figure 9.2.3 shows the phase for the other mode. It is clear that the changes in phase are correlated in time.

Figure 9.2.1 Plot of the amplitude for the first mode vs. time. In this case, ω_0=5.26 kHz,ϕ=$(10000)^{-1}$, $\Delta t=2\times10^{-5}$ sec, and the probability threshold for a pulse to occur in each time interval is 0.01.

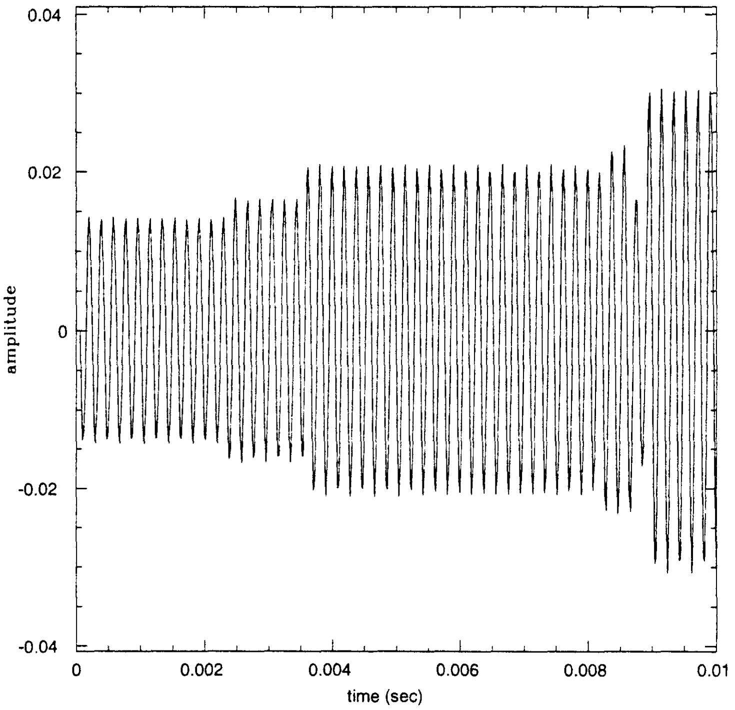

Figure 9.2.2 Plot of the phase for the first mode vs. time. In this case, ω_0=5.26 kHz, $\phi=(10000)^{-1}$, $\Delta t=2\times 10^{-5}$ sec, and the probability threshold for a pulse to occur in each time interval is 0.01.

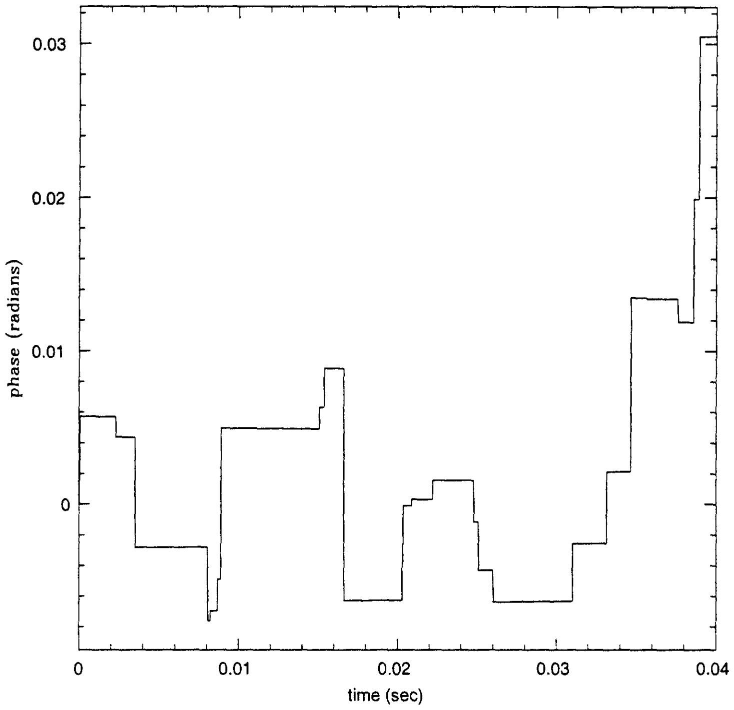

Figure 9.2.3 Plot of the phase for the second mode vs. time. In this case, ω_1=9.57kHz,,$\phi=(10000)^{-1}$, $\Delta t=2\times 10^{-5}$ sec, and the probability threshold for a pulse to occur in each time interval is 0.01.

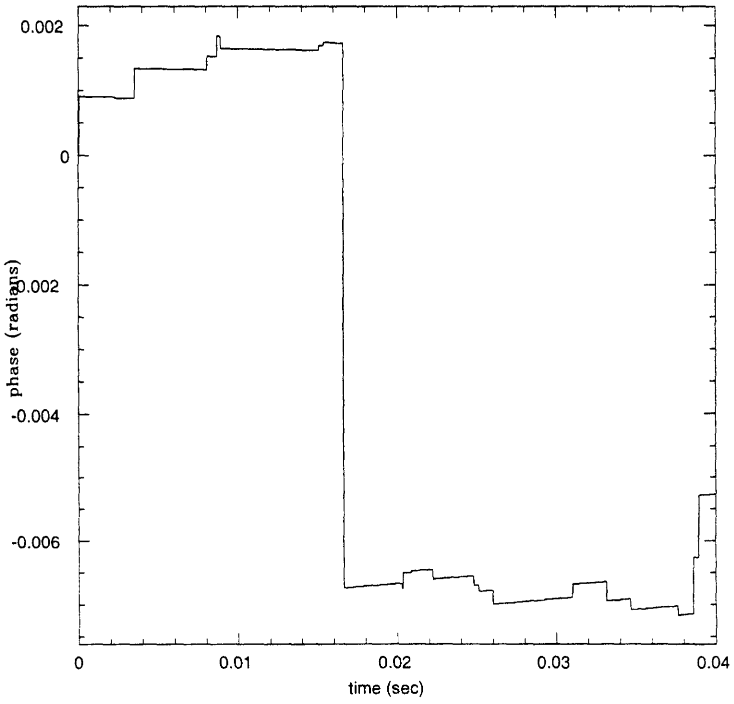

One must now find a method that can determine a change in phase. Once a suitable indicator for a phase change is available, then the cross correlation between the phase change for two different modes should have a maximum at time t=0. By taking the derivative of the phase from one mode, one obtains pulses that can be correlated with those obtained by taking the derivative of the phase from another mode.

Figure 9.2.4 This shows the derivative of the phase from figure 9.2.2

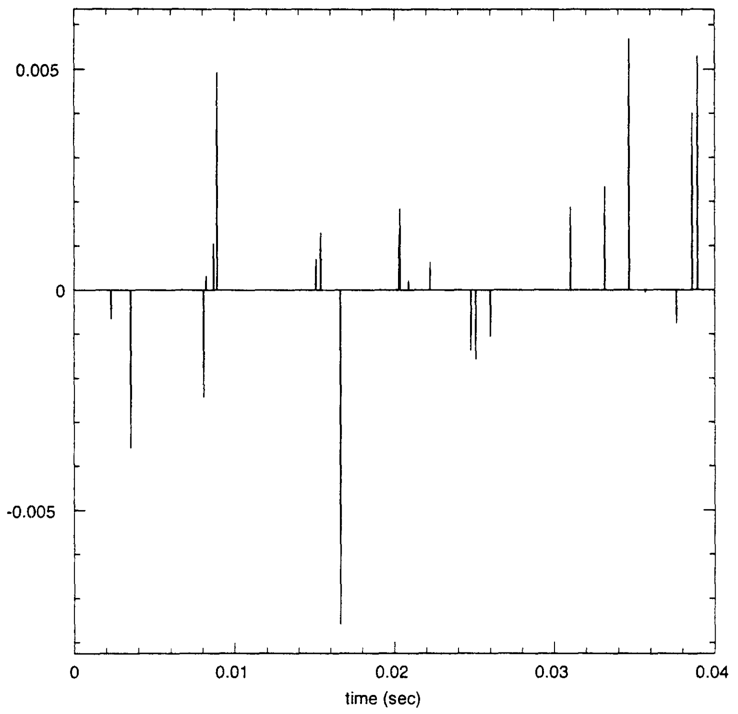

If one then takes the cross correlation of the absolute value of the derivative of the phase of one mode with the absolute value of the derivative of the phase of another mode, one sees that there is a maximum at time t=0 and that the data is correlated.

Figure 9.2.5 This figure is the cross correlation of the absolute value of the derivative of the phase from figure 9.2.2 with the absolute value of the derivative of the phase from figure 9.2.3.

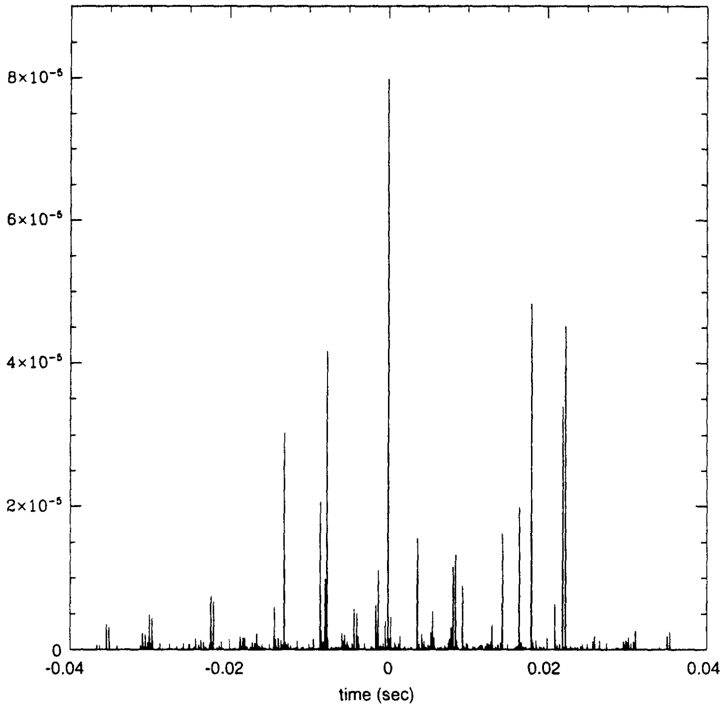

The method to extract the phase data from the amplitude signal that monitors the excitation of the normal mode is to mix this signal with a stable oscillator at the same frequency of the normal mode.

9.3 Experiment

When working with real data, there will be noise that corrupts the signal. The effect of the noise will depend upon the signal to noise ratio and the bandwidth of the filtering. In the current thermal noise experiment, there are resonant peaks that are a factor of 20 to 40 dB above a white noise background.

If one integrates the signal under one peak (in this case the 10.975 kHz mode), the RMS is 3.6×10^{-13}cm. If one takes the background noise to have a magnitude of $2 \times 10^{-15}\ cm/\sqrt{Hz}$, then a bandpass filter with a bandwidth of 300 Hz is necessary for a signal to noise ratio of ten. A signal to noise ratio of 100 requires a bandwidth of 3 Hz. The resonant frequencies of interest are at about 10 kHz and the Q's are between 5000 and 7000. The inherent bandwidth of the resonance then is 2 Hz. This presents a problem because the broadband noise exciting the electronic filter will be confused with the thermal noise exciting the mechanical filter of the normal mode.

Ideally, a high bandwidth time series of the interferometer output should contain all the data necessary to see the correlations in the phase jumps of different modes. The sampling frequency must meet the Nyquist criteria for the highest frequency mode considered. The data is then analyzed digitally as shown in figure 9.3.1. This analysis is done for two different resonant frequencies and is cross correlated.

Figure 9.3.1 Data analysis scheme used to search for changes in the phase of an oscillator.

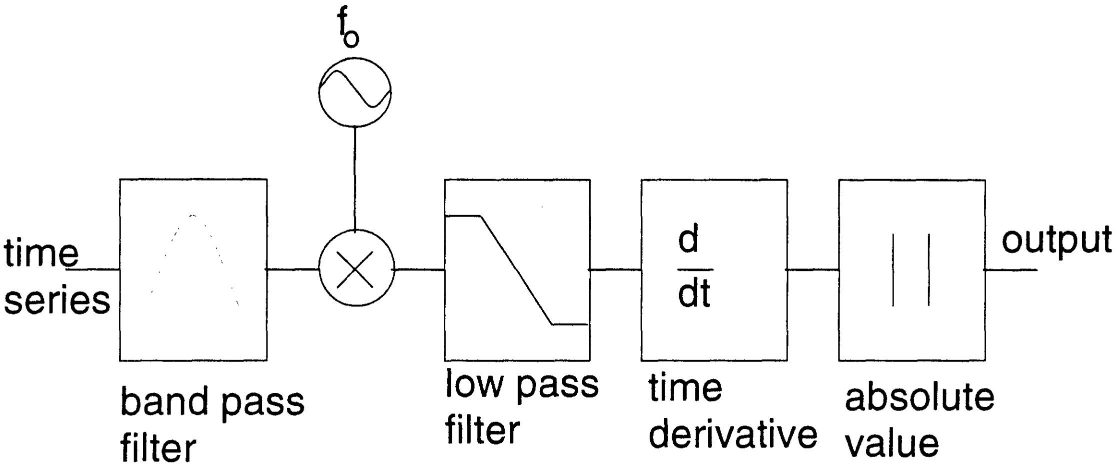

A time series of the interferometer output was taken with a sampling rate of 100 kHz. The data was low pass filtered at 25 kHz and high pass filtered at 7 kHz in order to include plate resonances at 9.6 kHz, 10.9 kHz, 17.8 kHz, 18.2 kHz and 19.9 kHz and to reduce aliasing from signals above the Nyquist frequency. Unfortunately, when doing the data analysis, the background noise exciting the bandpass filter dominated the input signal to the mixer. This means that any phase changes that occur are due response of the bandpass filter to the noise. When the data analyzed about a resonant frequency is cross correlated by that about another resonant frequency, it shows the same result as cross correlating the data about a resonant frequency with data about a frequency where there is no resonance. Since the background noise is the major component of the excitation, it sets an upper limit on the product of the rate and amplitude of the point like impulses that excite the normal modes.

Figure 9.3.2 Plot of power vs. bandwidth for the data that was taken. The power goes linearly with the bandwidth and the noise can be assumed to be Gaussian.

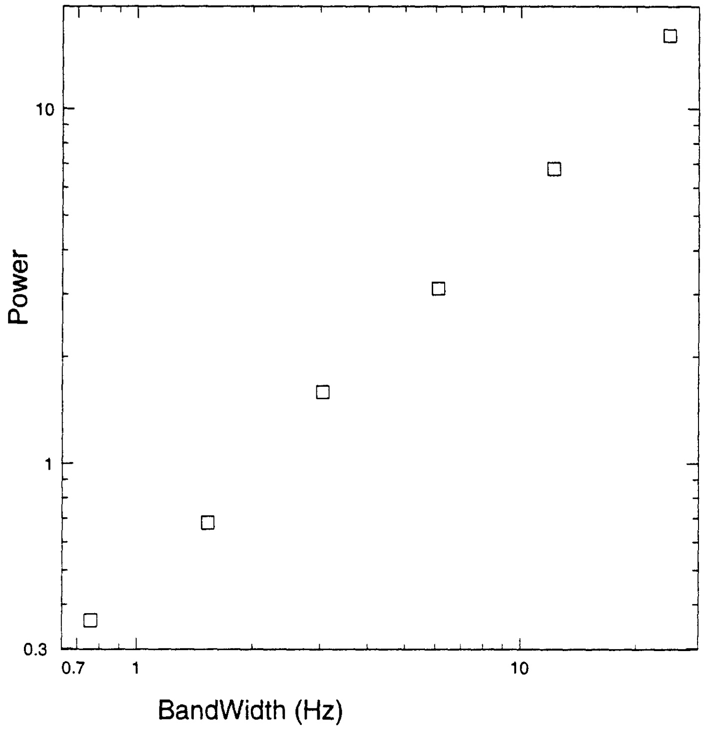

If the point like impulses have a Poisson distribution with an average occurrence rate R, exponential tail with time constant τ and a displacement Δx, the power spectral density of the displacement noise is (see for example [29])

$$x^2(\omega) = (\Delta x)^2 \left(\frac{1}{\omega^2 + 1/\tau^2}\right)\left(\frac{\omega^2}{\omega^2 + 4R^2}\right) \tag{9.3.1}$$

Assume $\tau^{-1} << \omega$ since the impulse acts like some displacement that happens suddenly and then takes a long time to settle. Using a noise of $2 \times 10^{-15}\, cm/\sqrt{Hz}$ at 500 Hz gives

$$\begin{gathered} x^2(\omega) \approx \frac{(\Delta x)^2 R}{\omega^2} \\ \sqrt{R}\Delta x < 6.3 \times 10^{-12} cm/\sqrt{Hz} \end{gathered} \tag{9.3.2}$$

Another limit that can be set is that $\Delta x < 3.6 \times 10^{-13} cm$ since the excitation could not be seen and thus, could not be bigger than the RMS under the peak. Figure 9.3.3 shows a plot of where the rate of impulses and their magnitude could be given these limit.

Figure 9.3.3 Plot of the range of values where the rate of pules and the magnitude of the pulses might lie.

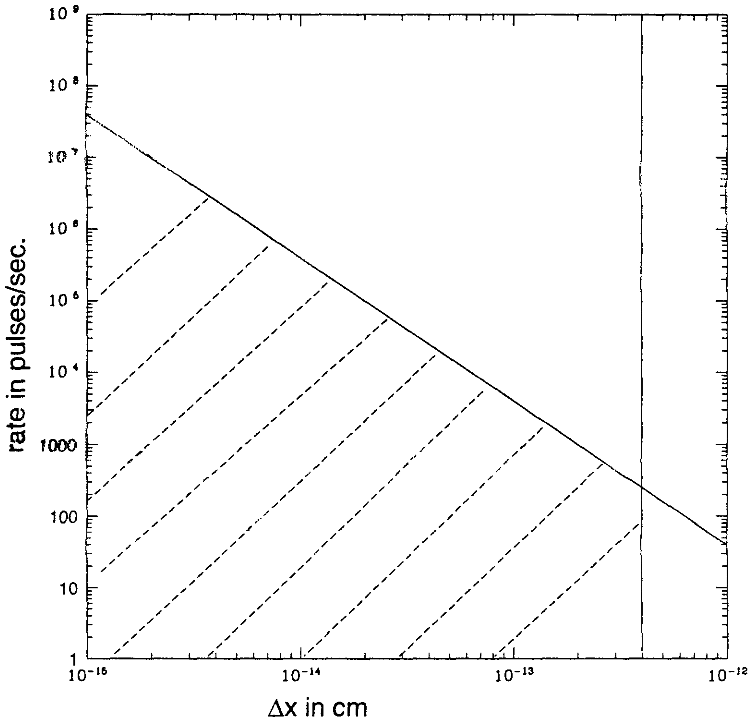

Chapter 10 Ideas for an Interferometer to Measure the Thermal Noise of a Test Mass

10.1 Thermal Noise Limit

In later generation gravity wave detectors, thermal noise from the internal modes of the test masses will become a limiting noise source. If LIGO is to meet the most conservative estimates for the detection of gravity waves from astrophysical sources such as coalescing binaries, then sensitivity of future detectors must approach a strain of $10^{-23} Hz^{-\frac{1}{2}}$ near 100 Hz [30]. Figure 1.2.2 shows that for a structure damped loss mechanism, this goal is not attainable.

There are very few ways to avoid this problem except to make the arm lengths longer or somehow to alter the test masses. The arm lengths are fixed by the initial design while the design of the test masses should be optimized to keep thermal noise at a minimum. The thermal noise can be reduced by significantly improving the Q of the mirror substrate material. Since the off-resonance thermal noise is inversely proportional to the square root of the Q, new materials with $Q > 10^7$ must be found.

Another possible way to avoid this noise limit is to measure the thermal noise from the mirrors. In the interferometer, the gravity wave strain signal is directly related to the motion of the test mass. The thermal noise in the test mass, on the other hand, is a motion about its centre of mass and not an actual motion of the centre of mass. This suggests that the test mass thermal noise can be removed from the gravity wave signal.

10.2 Intra-Test Mass Interferometer Noise

If one wants to remove this noise from the gravity wave signal, the sensor must have a noise that is lower than $3 \times 10^{-18} cm/\sqrt{Hz}$ and hopefully less than $4 \times 10^{-19} cm/\sqrt{Hz}$. Figure 10.2.1 shows the shot noise limit of an interferometer with an effective optical input power of 4 mW. If the input power is increased to 1 W, then the noise would go down by a factor of 15. If the loss does not exceed 10 ppm, then a sensitivity of less than $4 \times 10^{-19} cm/\sqrt{Hz}$ is possible.

The next thing to consider is whether an interferometer inside a test mass can achieve the same sensitivity. A great deal of research has been performed to understand and minimize the losses in fused quartz for the manufacturing of optical fibres. Current specifications set a limit on the losses for 1.06 μm light at 2 dB/km or 1.6 ppm/cm. At longer wavelengths, the losses are even smaller. If a test mass has a length of 10cm, then the loss due to absorption in the material will be 16 ppm. Losses in coating can now be made less than 1 ppm. Unfortunately, the test masses are coated for light with a different wavelength and for different transmissions. If dichroic coatings can be made with losses less than 1 ppm and the appropriate transmission to maximize the sensitivity, then this should not be a problem.

The calculation of the intra-test mass interferometer sensitivity is essentially the same as that done in chapter 4, except the losses in the medium must be taken into account. Assuming an input power of 1 Watt to each pair of cavities, perfect contrast and a modulation depth that approaches 0 (Γ<<1), the shot noise of the interferometer will be

$$noise = 3.9 \times 10^{-15} \frac{[(1-\mu)+\mu(L+T)]^2}{\mu^2 T(1-L-T)}\ cm/\sqrt{Hz} \tag{10.2.1}$$

where $\mu = \alpha^2 = 1 - (material\ loss)$.

Figure 10.2.1 The sensitivity of an intra-test mass interferometer as a function of loss in the cavity medium. The loss in the mirrors was set at 1 ppm.

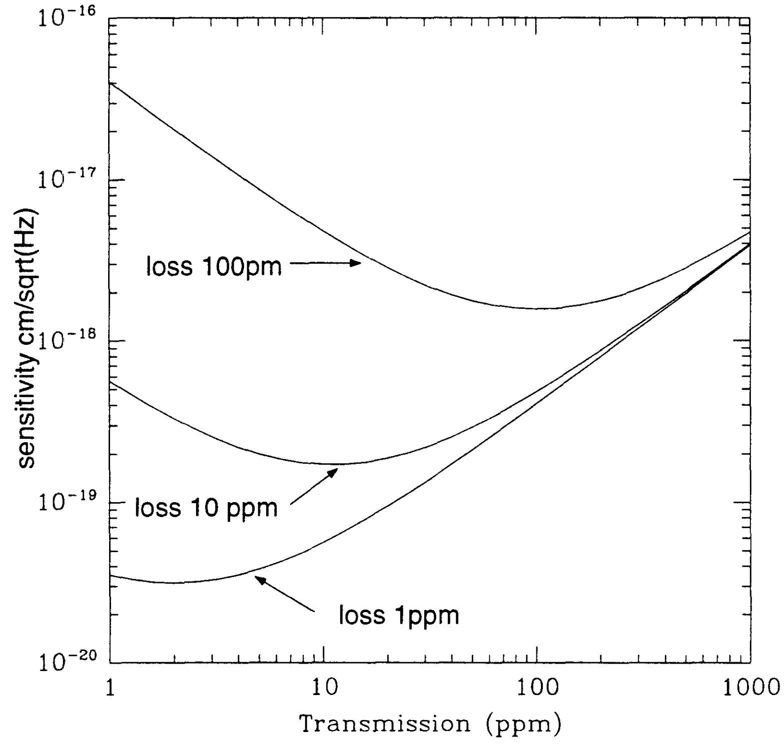

The bandwidth of an intra-test mass interferometer is greater than 1 kHz for even the most optimistic losses for the cavity medium. Since the optimum detection frequency for LIGO is at 100 Hz, the signal from an intra-test mass interferometer has an adequate frequency response for the gravity wave detection band.

Figure 10.2.2 The bandwidth of an intra-test mass interferometer as a function of loss in the cavity medium. The loss in the mirrors was set at 1 ppm

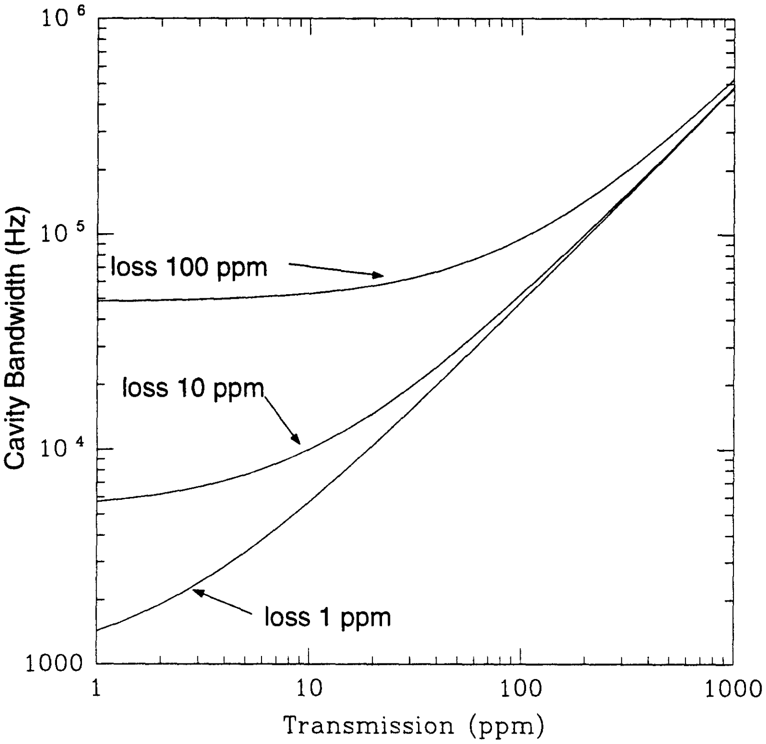

10.3 Conceptual Model for Implementation

If such an interferometer does achieve the necessary sensitivity, then it must be implemented in such a way that it measures the motion of the mirror where the laser beam spot for the gravity wave signal is located. There is an assumption that the motions of both sides of the mirror are correlated with each other. This is the same assumption that the motions of the test mass can be decomposed into normal modes. The normal mode is a rigid body and its motion is determined by the shape of that mode.

Since the optical path is inside the cavity, the index of refraction of the material becomes important. If the mirror changes shape, its density will change slightly and so will its index of refraction. The Lorentz-Lorenz formula for the index of refraction of a material is (see for example Marion [31])

$$\frac{n^2-1}{n^2+2} \times \frac{1}{\rho} = const. \tag{10.3.1}$$

If a block has dimensions $a \times a \times a$ and one of the sides decreases by a small amount δ, then the density of the material increases to

$$\rho' = \rho\left(1 + \frac{\delta}{a}\right) \tag{10.3.2}$$

The index of refraction increases by an amount

$$n' = n\left(1 + \Delta\frac{\delta}{a}\right)$$
$$\Delta = \frac{n^4 + n^2 - 2}{6n} \tag{10.3.3}$$

For fused quartz at $\lambda = 1.064\mu m$, $n = 1.44963$ and $\Delta = 0.52$. Since the optical path travelled by the light is proportional to the index of refraction, the actual displacement measured by an internal interferometer is

$$\begin{aligned} \Delta x_{optical} &= n'a' - na \\ &= n\left(1 + \frac{\delta}{a}\Delta\right)(a + \delta) - na \\ &\approx n\delta(1 + \Delta) \end{aligned} \tag{10.3.4}$$

The effective change in path length from the change in the refractive index then must be taken into account.

The actual implementation of the interferometer in the test mass can be done differently depending on whether the mirror must transmit light (as the mirror closest to the beam splitter must) or whether the mirror can be opaque (as the end mirrors can be). In fact, the end mirrors might be made of a material with a high Q that is completely opaque to the laser light such as single crystal Silicon. This could serve as a means to take care of the internal thermal noise from the end mirrors.

For the far mirrors, the interferometer beam spot can simply sample the area of the mirror that the main laser beam does (see figure 10.3.1). The only problem in building such a cavity and using it as a displacement transducer is that the frequency noise of the laser must be smaller than the displacement noise of the cavity. The frequency of the laser is stabilized by setting its frequency to the length of some reference cavity. The reference cavity must be quieter than the mirror itself. If the mirror is designed properly, it should have the smallest amount of thermal noise for a piece of fused quartz that is possible. It is not clear then that a single cavity measuring device would work.

Figure 10.3.1 Model of an intra-test mass interferometer for an end mirror.

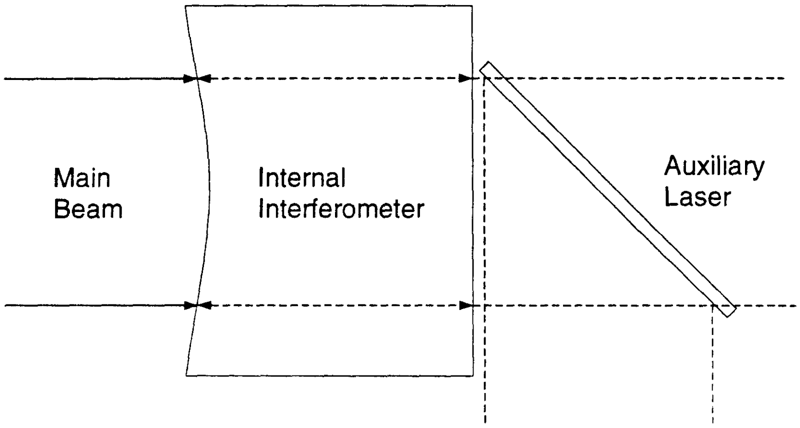

One way to avoid the problem of frequency noise is to use the technique developed in this thesis to remove common mode noise sources. At least two cavities would be set up inside the mirror (see figure 10.3.2). They would sample two or more parts of the mirror. The difficulty in this approach is how to reconstruct the motion of the mirror where the main gravity wave detector beam samples it from the displacement of a few discrete points on the mirror. The model described in chapter 9 assumes that all the normal modes of the mirror are excited at the same time by the microscopic processes of the loss mechanism. If enough points on the mirror are sampled, the measured motion can be decomposed into some of the mirror normal modes. The amplitude of these normal modes can then be extrapolated to obtain the amplitude of the other normal modes. The motion of the entire surface of the mirror can then be reconstructed.

Figure 10.3.2 Model of an intra-test mass interferometer for the mirror nearest the beam splitter.

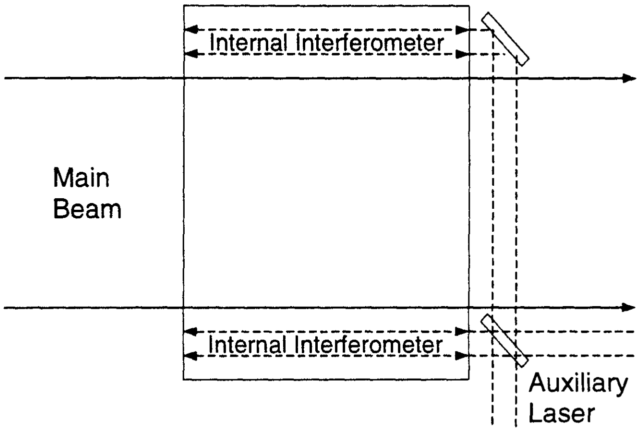

Another way to remove the motion of the mirror about its centre of mass is to coat both sides of the mirror and have the light reflect from both sides (see figure 10.3.3). If the phase change of the light due to motion of the far side is equal and opposite to the phase change produced from motion of the near side, then the total phase change of light reflected from the mirror will be insensitive to thermally excited normal modes of the mirror. If the cavity formed inside the mirror is resonant for a length l, then the phase for the reflected electric field (see appendix A) will be

$$\begin{aligned} \varphi_1 &= 0 \\ \varphi_2 &= Arg\left[e^{i\frac{\omega\Delta l}{c}} \times \frac{r_1 - \alpha^2 r_2 (r_1^2 + t_1^2) e^{-ix}}{1 - \alpha^2 r_1 r_2 e^{-ix}}\right] \\ x &= \frac{4\omega n \Delta l (1 + \Delta)}{c} \end{aligned} \tag{10.3.5}$$

where Δ is defined in equation 10.3.3. For small changes in length $\left(\frac{\Delta l\omega}{c} << 1\right)$, the phase for ε_2 will be

$$\frac{\omega\Delta l}{c}\left[1 + 4n(1+\Delta)\alpha^2 r_2 \left(\frac{r_1^2 + t_1^2}{r_1 - \alpha^2 r_2 (r_1^2 + t_1^2)} - \frac{r_1}{1 - \alpha^2 r_1 r_2}\right)\right] \tag{10.3.6}$$

By setting equation 10.3.6 equal to 0, the appropriate reflectivity and transmission (r_2, t_2) can be found to satisfy the condition that the reflected light is insensitive to a symmetric mirror motion about its centre of mass. Putting in typical values for r_1, t_1 shows that this technique is very dependent on having all the reflectivities and transmissions very precisely determined. In general, this is not a good way to design an experiment so that this technique does not look very promising.

Figure 10.3.3 Sketch of the mirror and the light path for a motion of the mirror about its centre of mass. Each side of the mirror moves an amount Δl.

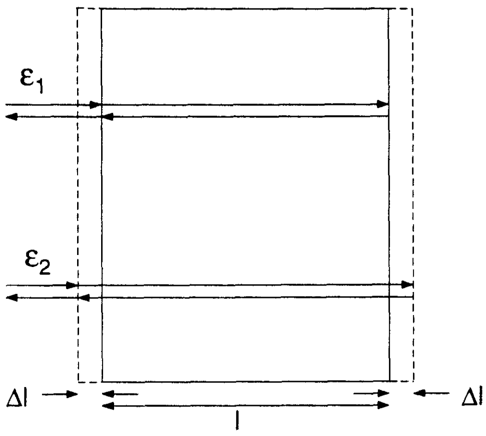

Chapter 11 Conclusions

The detection of gravitational waves from astrophysical sources will be a great triumph for Einstein's Theory of General Relativity and will open a new window to the universe outside of the electromagnetic spectrum. The inherent weakness of a gravitational wave makes this experiment a challenging task and requires a very detailed understanding of all possible noise sources in the detection apparatus.

This thesis discusses thermal noise which could ultimately be the limiting noise source for an interferometric gravitational wave detector. Thermal noise arises when a system is disturbed from its equilibrium state by the statistical fluctuations inherent in a heat bath. In mechanical systems, there are processes which cause the system to dissipate energy over time. This introduces heat into the thermal reservoir and raises its temperature. These same processes are driven by statistical thermal fluctuations and in turn, excite the mechanical system.

In the particular case of a gravity wave detector, there are two mechanical systems where the thermal noise can be a significant problem: the suspensions that hold the interferometer mirrors and the internal normal modes of the mirrors. In both cases, the distribution of the thermal noise in the frequency domain is important. The principal methods to reduce the thermal noise is to put the mechanical resonant frequency of the system out of the detection band and to use a high Q design. This ensures that most of the thermal noise is not in the frequency regime of interest. An actual prediction of the thermal noise floor of a gravity wave detector is a detailed calculation that involves a good understanding of the mechanical systems and their loss mechanisms.

The thermal noise of a pendulum was calculated by considering the losses in the flexure of the thin fibres that support the pendulum mass. The thermal noise from the suspension depends upon the loss mechanism in the thin fibres. One such mechanism is thermoelastic damping. An experimental investigation of thermoelastic damping was performed by measuring the Q's of thin fibres made of tungsten, sapphire, silicon and fused quartz. Tungsten had the highest losses with Q's on the order of 10^3 that were relatively frequency independent. Fused quartz had the lowest losses with Q's between $10^5 - 10^6$ that again were relatively frequency independent. The results indicated that thermoelastic damping is at best only an upper limit for the Q of a wire. A calculation of the thermal noise for a pendulum using thermoelastic damping as a lower limit for the loss shows that both fused quartz and tungsten produce about the same amount of thermal noise. While tungsten has a higher loss than fused quartz, it also has a higher yield strength. These two effects tends to cancel each other.

In the interferometer mirrors, there is thermal noise due to the inherent mechanical losses in the substrate material. The two models that are commonly used in describing the loss mechanisms in bulk solids have different frequency dependences and are called structure damping and viscous damping. The ratio of the thermal noise from structure damping over the thermal noise from viscous damping for frequencies less than the resonant frequency is proportional to $\sqrt{f_0/f}$. Since the lowest resonant frequency for a

LIGO mirror is on the order of 10 kHz, the noise from the two different loss mechanisms is a factor of 10 different at 100 Hz which is the optimum detection frequency band for LIGO. An experiment was built to measure the off-resonance thermal noise in a test piece of fused quartz and thus, determine the frequency dependence of the loss mechanisms.

Some interesting techniques using interferometry to perform high sensitivity measurements were developed. Since mirrors with very low losses on the order of a few ppm. can now be manufactured, it is possible to make a Fabry-Perot cavity with a very high finesse $\left(> 10^5\right)$. The phase of the light inside such a cavity is very sensitive to small displacements of the cavity mirrors. By building two Fabry-Perot cavities each with a common mirror, a very sensitive measurement of an anti-symmetric motion of the common mirror is possible ($< 10^{-17} cm/\sqrt{Hz}$ for a 40 mW laser operating at $\lambda = 1.06 \mu m$). The output of each cavity can be combined in a Mach-Zender interferometer where symmetric noise sources cancel. The interferometer in this thesis clearly demonstrated that the frequency noise of a laser can be precisely cancelled by carefully controlling the lengths of the Fabry-Perot cavity arms.

The actual measurement of the thermal noise was inconclusive. The typical Q's measured for the piece of fused quartz in this experiment was between $10^4 - 10^5$ for resonant frequencies between 5 and 75 kHz. The thermal noise at the mechanical resonance was accurately measured ($4 \times 10^{-13} cm$ RMS for an 11 kHz resonance). The off-resonance thermal noise was $2 \times 10^{-15} cm/\sqrt{Hz}$ which was too high to be the low frequency tail of the thermal noise from any of the mechanical resonances. A careful study of the various possible experimental noise sources including electronic noise, frequency noise, amplitude noise and others could not find one that was responsible for the measured noise. An investigation of other possible displacement noise sources included the off-resonance thermal noise from higher frequency normal modes and a model for optical contacting noise. Again, these two possibilities could not explain the noise adequately. A series of experiments to gain a better understanding of the measured noise is proposed in chapter 8.

A model to understand the interaction between the loss mechanisms in the form of Poisson distributed impulses and their excitation of normal modes was presented. The model attempts to understand the correlation of thermal noise in different normal modes of the mirror. An experiment to test this hypothesis could only set an upper limit to the strength and rate of these impulses.

Finally, some conceptual designs to measure the thermal noise directly in a gravity wave detector test mass were discussed. If this becomes possible, the thermal noise could be subtracted from the gravity wave signal and would no longer be a limit for the sensitivity of a gravity wave detector. The optical experiment performed in this thesis is a prototype for such a technique.

Appendix A The Fabry-Perot Cavity

A light beam incident upon a Fabry-Perot cavity is partially reflected and partially transmitted through an incident mirror, partially reflected and partially transmitted through an end mirror whereupon the process repeats itself until all the light either escapes from the cavity or is attenuated by losses in the mirror. The interesting properties of this cavity occur when the light is resonant inside.

Figure A.1 Fabry-Perot cavity. α is the electric field transmission of the cavity medium or $\sqrt{1 - material\ loss}$. In general, it is set to 1.

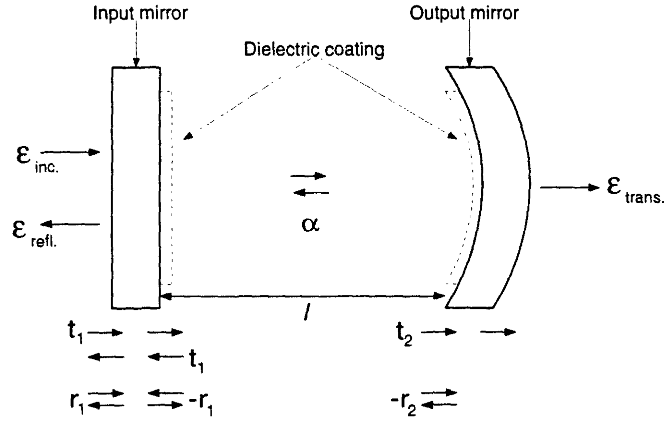

The equation for the reflected electric field is:

$$\begin{aligned}
\frac{\varepsilon_{refl}(t)}{\varepsilon_{inc}(t)} &= r_1 e^{i\omega t} - \alpha^2 r_2 t_1^2 e^{iw(t-\frac{2l}{c})} - \alpha^4 r_1 r_2^2 t_1^2 e^{i\omega(t-\frac{4l}{c})} - \dots \\
&= e^{i\omega t}\left(\frac{r_1 - \alpha^2 r_2 (r_1^2 + t_1^2) e^{-ix}}{1 - \alpha^2 r_1 r_2 e^{-ix}}\right) \qquad x = \frac{2\omega l}{c} \\
&= e^{i\omega t} \times A_{refl}(x) \times e^{i\varphi_{refl}(x)}
\end{aligned} \tag{A.1}$$

Similarly, the equation for the transmitted field is:

$$\begin{aligned}
\frac{\varepsilon_{trans}}{\varepsilon_{inc}} &= e^{i\omega t}\left(\frac{\alpha t_1 t_2}{1 - \alpha^2 r_1 r_2 e^{-ix}}\right) \\
&= e^{i\omega t} \times A_{trans}(x) \times e^{i\varphi_{trans}(x)}
\end{aligned} \tag{A.2}$$

If the reflectivity of the mirror is R, transmission T and loss L, then $r = \sqrt{R}$, $t = \sqrt{T}$ and $R + T + L = 1$. Also, α is set to 1. In this experiment, both mirrors have the same coatings with T=22ppm and a L< 5ppm. Figures A.2—A.5 show the intensity

($I(x) = \varepsilon(x)\varepsilon^*(x)$) and phase ($\varphi(x) = \arg[\varepsilon(x)]$) of the reflected and transmitted light for the loss and transmission given above.

Figure A.2 Reflected intensity of a Fabry-Perot cavity (T=22 ppm, L=5 ppm).

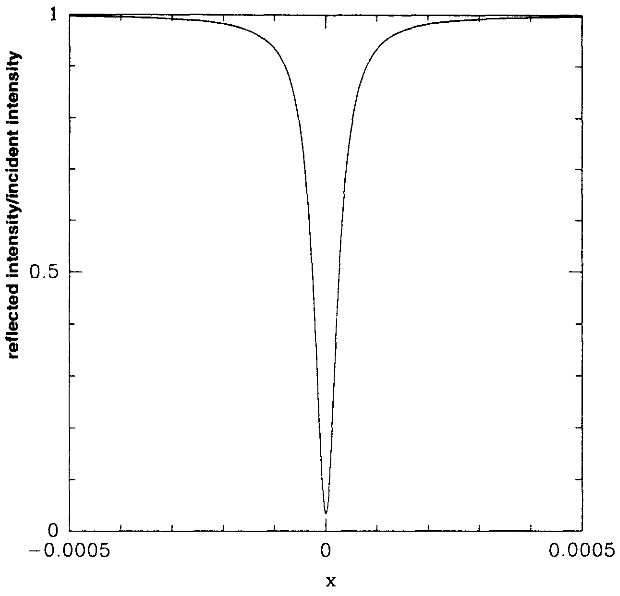

Figure A.3 Reflected phase of a Fabry-Perot Cavity (T=22 ppm, L=5 ppm).

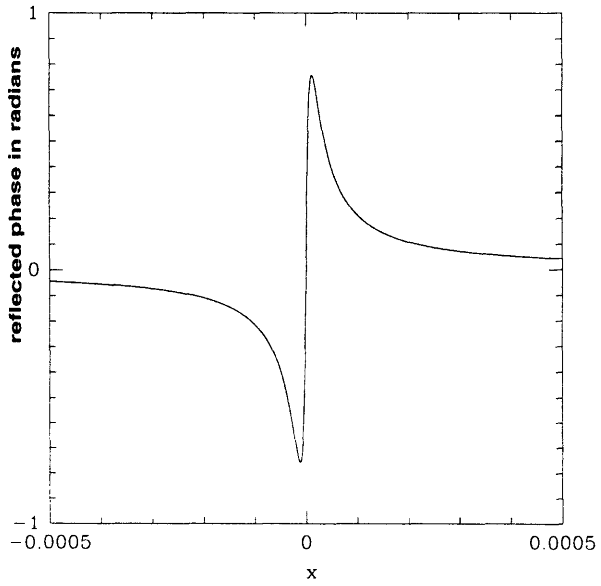

Figure A.4 Transmitted intensity of a Fabry-Perot cavity (T=22 ppm, L=5 ppm).

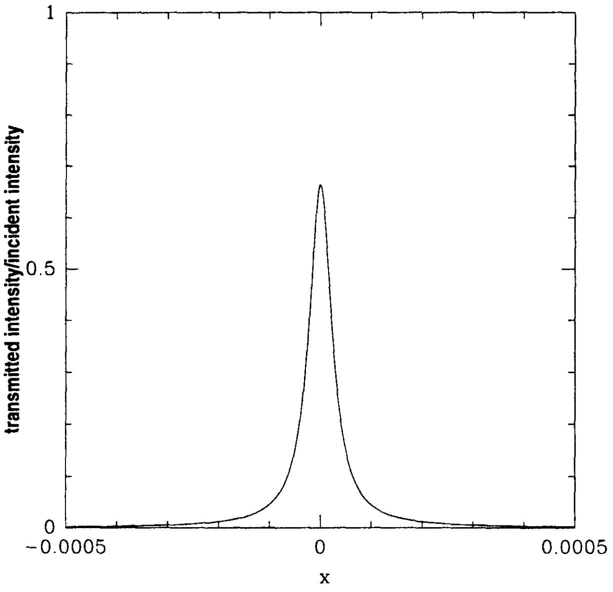

Figure A.5 Transmitted phase of a Fabry-Perot cavity (T=22 ppm, L=5 ppm).

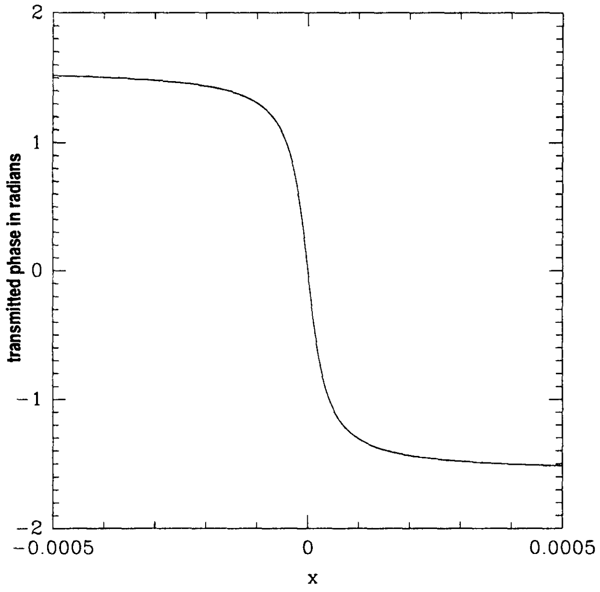

Some of the properties of a symmetric cavity for $T, L << 1$ are:

$\frac{I_{trans}}{I_{inc}}$ peak	$\left(\frac{T}{T+L}\right)^2$
φ_{trans}, $x << 1$	$\frac{-(1-L-T)}{T+L}x$
Bandwidth (FWHM)	$\frac{(T+L)}{\pi}\left(\frac{c}{2l}\right)$
$\frac{I_{refl}}{I_{inc}}$ minimum	$\left(\frac{(1-L-T)L}{L+T}\right)^2$
φ_{refl}, $x << 1$	$\frac{T}{L(T+L)}x$

Figure A.6 shows the dependence of the transmitted light intensity through the cavity as a function of mirror loss for the cavity at resonance. For mirrors with low transmissions, it is important to keep the losses low in order to insure that the transmitted light does not become too small.

Figure A.6 The intensity of light transmitted through the Fabry-Perot cavity as a function of mirror loss for the cavity at resonance and a fixed mirror transmission of 22 ppm

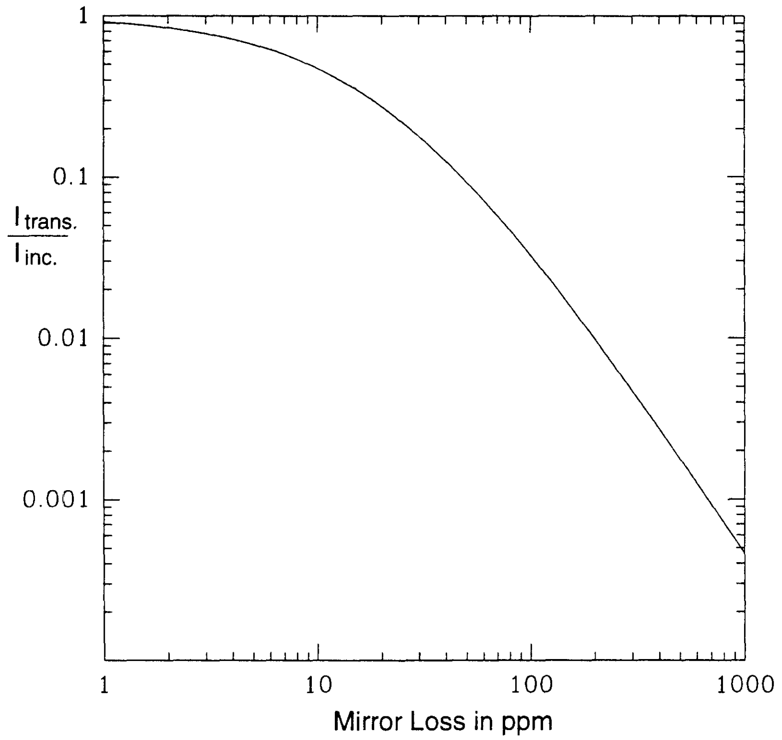

Figure A.7 shows the dependence of the reflected light intensity from the cavity as a function of mirror loss for the cavity at resonance. For mirrors with low transmissions, it is important to keep the losses low in order to insure that the reflected light does not become too large.

Figure A.7 The intensity of light reflected from a Fabry-Perot cavity as a function of mirror loss for the cavity at resonance and a fixed mirror transmission of 22 ppm

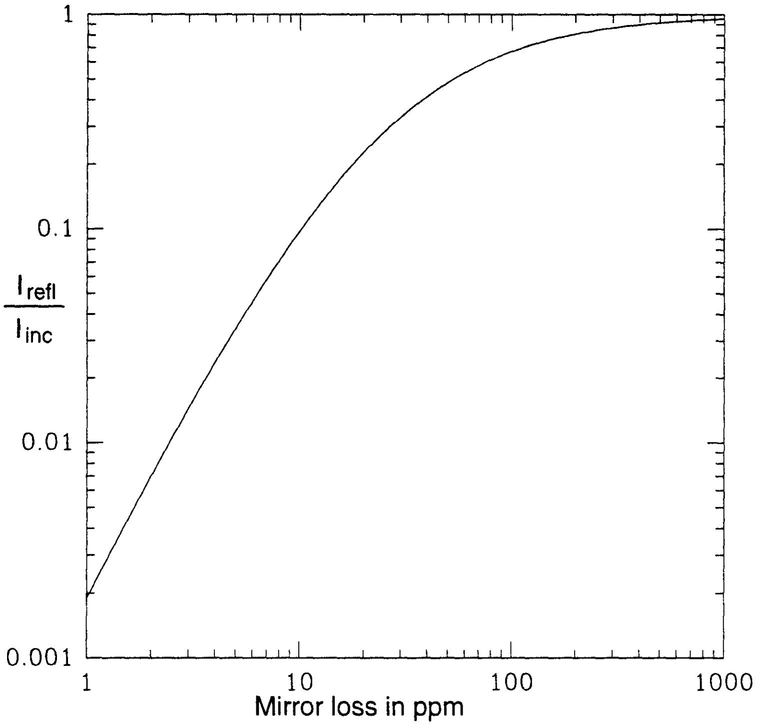

Figure A.8 shows the cavity bandwidth as a function mirror loss and transmission. The cavity bandwidth should not be narrower than that of the signal to be measured.

Figure A.8 Cavity bandwidth as a function of mirror loss and transmission.

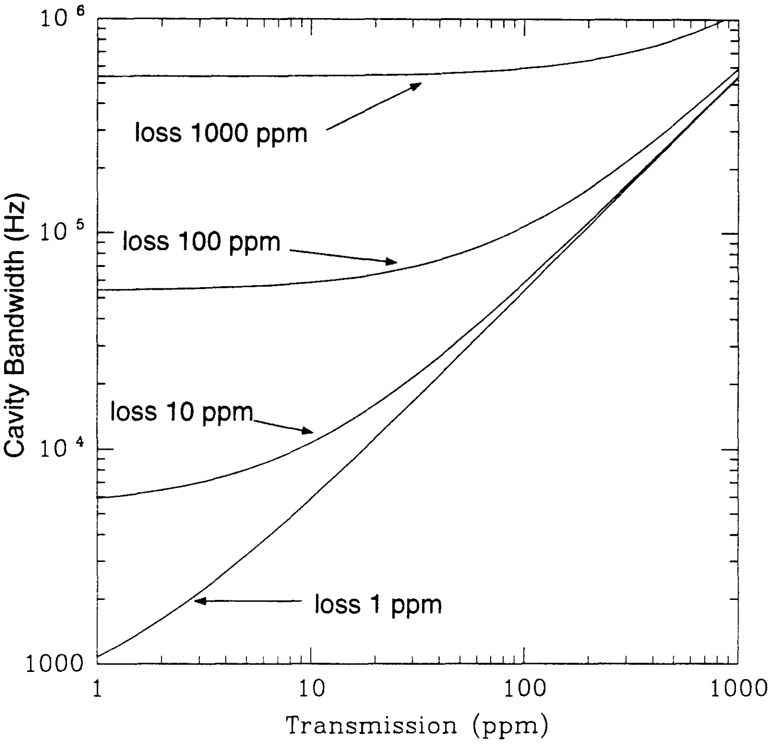

Appendix B Phase Modulation

The laser light was phase modulated by passing it through a rectangular LiTaO3 crystal Pockels cell 7mm×7mm wide by 30mm long. Unfortunately, the faces were cut square which meant relatively high reflection losses (14% for each face) since n=2.2 for LiTaO3. The electro-optic axis z' was perpendicular to the optic axis z and parallel to the polarization of the linearly polarized light beam (see figure B.9).

Figure B.9 $LiTaO_3$ Pockels cell

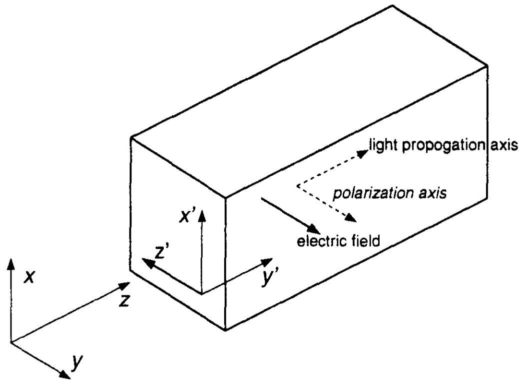

An RF voltage was applied through a tuned transformer circuit to the crystal (see figure B.10).

Figure B.10 Tuned transformer circuit for Pockels cell

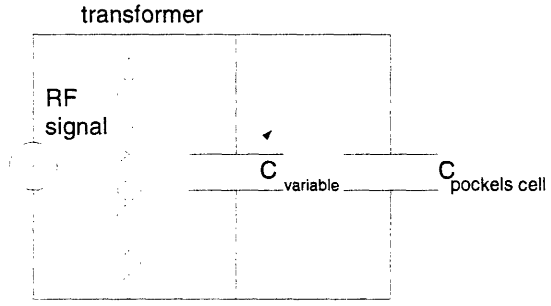

The electro-optic tensor[32] for LiTaO3 is that of a 3m symmetry group crystal and has the form:

$$\begin{pmatrix} 0 & r_{12} & r_{13} \\ 0 & -r_{12} & r_{13} \\ 0 & 0 & r_{33} \\ 0 & r_{42} & 0 \\ r_{42} & 0 & 0 \\ r_{12} & 0 & 0 \end{pmatrix} \tag{B.3}$$

By applying an electric field $E_{z'}$ along the z' axis, one creates an index ellipsoid:

$$\left(\frac{1}{n_{x'}^2} + E_{z'}r_{13}\right)x'^2 + \left(\frac{1}{n_{y'}^2} + E_{z'}r_{13}\right)y'^2 + \left(\frac{1}{n_{z'}^2} + E_{z'}r_{33}\right)z'^2 = 1 \tag{B.4}$$

Since the light is linearly polarized along the z' axis, only the index of refraction along this axis is important.

$$n'_{z'} = n_{z'} - \frac{1}{2}E_{z'}r_{33}n^3_{z'} \tag{B.5}$$

The electric field of the light becomes:

$$\begin{aligned} \varepsilon_{z'} &= \varepsilon_0 e^{i\left(\omega t - \frac{\omega}{c}n'_{z'}l\right)} \\ &= \varepsilon_0 e^{i\left(\omega t - \frac{\omega}{c}\left(n_{z'} - \frac{1}{2}E_{z'}r_{33}n^3_{z'}\right)l\right)} \end{aligned} \tag{B.6}$$

where l is the length of the crystal.

If $E_{z'}$ has the form

$$E_{z'} = -\frac{V_0}{d}\sin(\omega_m t) \tag{B.7}$$

where d is the width of the crystal, then

$$\begin{aligned} \varepsilon_{z'} &= \varepsilon_0 e^{i\left(\omega t - \frac{\omega}{c}\left(n_{z'} + \frac{V_0}{2d}\sin(\omega_m t) r_{33}n^3_{z'}\right)l\right)} \\ &= \varepsilon_0 e^{i(\omega t - \Gamma \sin(\omega_m t) + \phi)} \end{aligned} \tag{B.8}$$

where

$$\begin{aligned} \Gamma &= \frac{\omega V_0 r_{33} n^3_{z'} l}{2cd}, \; r_{33} = 30 \times 10^{-12}\frac{m}{V} \\ &= 4 \times 10^{-3} V_0 \frac{rad}{V} \end{aligned} \tag{B.9}$$

and is called the modulation index. Using the relations

$$\begin{aligned} \cos(\Gamma \sin(\theta)) &= J_0(\Gamma) + 2\sum_{k=1}^{\infty} J_{2k}(\Gamma)\cos(2k\theta) \\ \sin(\Gamma \sin(\theta)) &= 2\sum_{k=0}^{\infty} J_{2k+1}(\Gamma)\cos((2k+1)\theta) \end{aligned} \tag{B.10}$$

where J_k are Bessel's function of the first kind and the limit where $\Gamma < 1$, then

$$\begin{aligned} e^{-i\Gamma \sin(\omega_m t)} &= \cos(\Gamma \sin(\omega_m t)) - i \sin(\Gamma \sin(\omega_m t)) \\ &= J_0(\Gamma) - i2J_1(\Gamma)\sin(\omega_m t) + ... \\ &= J_0(\Gamma) - J_1(\Gamma)\left(e^{i\omega_m t} - e^{-i\omega_m t}\right) \end{aligned} \tag{B.11}$$

and the light electric field (neglecting constant phase terms) will be

$$\begin{aligned} \varepsilon_{z'} &= \varepsilon_0 e^{i\omega t}\left[J_0(\Gamma) - J_1(\Gamma)\left(e^{i\omega_m t} - e^{-i\omega_m t}\right)\right] \\ &= \varepsilon_0 J_0(\Gamma)e^{i\omega t} - \varepsilon_0 J_1(\Gamma)e^{i(\omega+\omega_m)t} + \varepsilon_0 J_1(\Gamma)e^{i(\omega-\omega_m)t} \end{aligned} \tag{B.12}$$

This produces two sidebands at frequencies $\omega \pm \omega_m$ around the carrier at frequency ω.

Figure B.11 Carrier and sidebands for phase modulated light

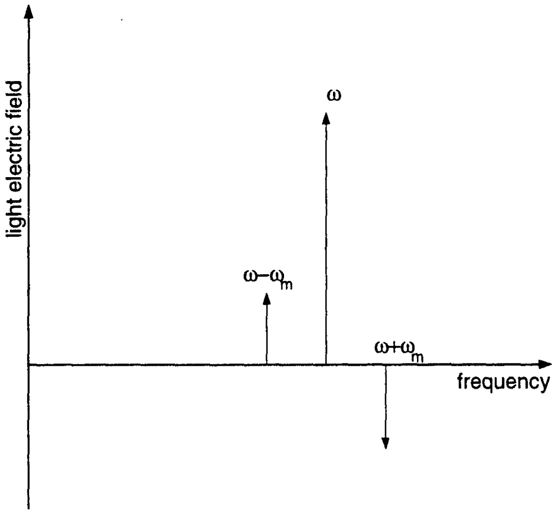

Bibliography

[1] K. S. Thorne, *300 years of Gravitation.* Cambridge University Press, Cambridge, 330, 1987.

[2] L. L. Smarr, ed., *Sources of Gravitational Radiation*, Cambridge University Press, 1979.

[3] P. F. Michelson, J. Price, and R. C. Taber *Science*, vol. 237, p. 150, 1987.

[4] R. Weiss and B. Block *J. Geophys. Res.*, vol. 70, p. 5615, 1965.

[5] R. E. Vogt, R. W. Drever, F. J. Raab, K. S. Thorne, and R. Weiss, "Laser interferometer gravitational wave observatory, proposal to national science foundation," December, 1989.

[6] N. Wax, ed., *Selected Paperson Noise and Stochastic processes.* Dover Publications, 1954.

[7] F. Reif, *Fundamentals of Statistical and Thermal Physics.* McGraw-Hill Book Co., 1965.

[8] H. Callen and T. Welton *Phys. Rev.*, vol. 83, no. 1, p. 34, 1951.

[9] H. Callen and R. Grene *Phys. Rev.*, vol. 86, no. 5, p. 702, 1952.

[10] A. S. Nowick and B. S. Berry, *Anelastic Relaxation in Crystalline Solids.* Academic, 1972.

[11] P. R. Saulson *Phys. Rev. D*, vol. 42, p. 2437, 1990.

[12] F. K. du Pre *Phys. Rev.*, vol. 78, p. 615, 1950.

[13] P. G. Roll, R. Krotkov, and R. H. Dicke *Ann. Phys.*, vol. 26, p. 442, 1961.

[14] B. Block and R. D. Moore *J. Geophys. Res.*, vol. 71, p. 4361, 1966.

[15] D. Shoemaker, R. Schilling, L. Schnupp, W. Winkler, K. Maischberger, and A. Rudiger *Phys. Rev D*, vol. 38, no. 2, p. 423, 1988.

[16] J. C. Livas, *Upper Limits for Gravitational Radiation from Some Astrophysical Sources.* PhD thesis, Massachusetts Institute of Technology, 1987.

[17] A. Gillespie and F. Raab *Physics Ltters A*, vol. 178, p. 357, 1993.

[18] L. Landau and E. M. Lifshitz, *Theory of Elasticity.* Pergamon Press Ltd., 1970.

[19] C. Zener *Phs. Rev.*, vol. 52, p. 230, 1937.

[20] C. Zener *Phs. Rev.*, vol. 53, p. 90, 1938.

[21] L. D. Landau, E. M. Lifshitz, and L. P. Ptavskii, *Statistical Physics.* Pergamon Press., 1980.

[22] J. Kovalik and P. R. Saulson *Rev. Sci. Instrum.*, vol. 64, no. 10, p. 2942, 1993.

[23] P. M. Morse, *Vibration and Sound.* McGraw-Hill Book Co., 1948.

[24] R. D. Blevins, *Formulas for Frequency and Mode Shape.* Robert E. Krieger Publishing Co., 1986.

[25] A. W. Leissa, "Vibration of shells," tech. rep., Washington, Scientific and Technical Information Office, NASA, 1973.

[26] R. W. P. Drever, J. Hall, F. Kowalski, J. Hough, G. Ford, A. Munley, and H. Ward *Appl. Phys. B*, vol. 31, p. 97, 1983.

[27] A. Rudiger, R. Schilling, L. Schnupp, W. Winkler, H. Billing, and K. maischberger *Optica acta*, vol. 28, no. 5, p. 641, 1981.

[28] V. N. Braginsky, V. Mitrofanov, and V. Panov, *Systems with Small Dissipation*. The University of Chicago Press, 1985.

[29] Y. W. Lee, *Statistical Theory of Communication*. John Wiley & Sons, Inc., 1963.

[30] A. Abramovici, W. Althouse, R. Drever, Y. Gursel, S. Kawamura, F. Raab, D. Shoemaker, L. Sievers, R. Spero, K. Thorne, R. Vogt, R. Weiss, S. Whitcomb, and M. Zucker *Science*, vol. 256, p. 325, 1992.

[31] J. Marion and M. heald, *Classical Electromagnetic Radiation*. Academic Press, 1980.

[32] A. Yariv, *Optical Electronics*. Holt, Rhinehart and Winston, Inc., 3rd ed., 1985.

2175-72